# MSc. Thesis

## Microstructural characterisation of recycled carbon fibre reinforced polymer composites

Application and evaluation of the method of ellipses

Auteur
Jesper Oranje

TU Delft

Image by ELG Carbon Fibre

*I had a microscopy pun,*
*But it's out of focus*

# Microstructural characterisation of recycled carbon fibre reinforced polymer composites

-

*Application and evaluation of the method of ellipses*

*Master of science thesis*

*By*

*Jesper Oranje*

*For obtaining the degree Master of Science at the Delft University of Technology*

*November 3rd, 2021*

*Committee:*

| | |
|---|---|
| *Prof. Clemens A. Dransfeld* | *TU Delft, chair, supervisor* |
| *Asst. Prof. Miguel A. Bessa* | *TU Delft, co-supervisor* |
| *Asst. Prof. Daniël M. J. Peeters* | *TU Delft, examiner* |

*Faculty of Aerospace Engineering*
*&*
*Faculty of Mechanical, Maritime and Materials Engineering (3ME)*

Materials Science and Engineering

*A digital version of this report can be found at*
*https://repository.tudelft.nl/*

# Preface

This thesis would not have been possible without the enormous support I've received from my girlfriend, family, in-laws, friends and colleges at the Rotterdam University of Applied Sciences, which have given me the chance to combine work and research.
I would like to especially thank my supervisors Clemens Dransfeld and Miguel Bessa for their guidance and open-door policy regarding any questions I had.
I sincerely hope this thesis is of help to anyone interested in the advancement and application of recycled carbon fibre reinforced polymers.

- Jesper

# Abstract

Carbon fibre reinforced polymer (CFRP) composites are well-known for their specific strength and stiffness properties. For the past two decades, various industries have increasingly used these materials to improve performance and reduce emissions. This increased use has caused a problematic growth in both production and end-of-life CFRP waste. Recent developments in recycling processes allow recycled carbon fibres (rCF) to have undamaged and clean surfaces with intact sizing, retaining the mechanical properties of non-recycled virgin carbon fibres (vCF) at a considerable cost reduction.

Unfortunately, CF recyclate from these recycling procedures is highly diffuse making them useless for structural application. For making rCF material viable to be used in structural applications, further processing of the recyclate is necessary. To manufacture high-performance rCF materials which feature homogenously distributed, orientated and aligned fibres, considerable effort has to be spent in controlling the microstructure during processing.

The presented thesis has focused on introducing an initial characterisation method that allows for quantitative analysis and comparison between rCF microstructures. Characterisation is performed by analysing elliptical CF footprints in perpendicular cross-section micrographs. Fibres in the micrograph are identified and segmented through a semi-supervised machine learning tool. The elliptical fibre shape is measured by the method of ellipses (MoE) in FIJI ImageJ. This MoE extracts the position and elliptical shape of every fibre footprint in the micrograph. Analysis of the microstructure is done in python to quantify the microstructural morphology by fibre diameter, fibre orientation distribution (FOD), global-local fibre volumes (Vf), fibre density distribution (FDD) and Fibre-to-Fibre (FtF) spacing.

It was found that the method is accurate and reliable in identifying and measuring fibres present in the cross-section micrograph. Similarly, calculated values for Vf, FDD and FtF spacing can be used for characterising the quality of studied materials.
Unfortunately, despite being frequently used in literature to characterise highly aligned and orientated CF materials, all fibre orientation measurements were flawed by the inherent susceptibility of the MoE to calculate fibre orientation with large biases. This orientation bias was caused by the error sensitivity of the arccosines function used for calculating the out-of-plane (OoP) angle. Minute elliptical shape differences in near perpendicular fibres with almost circular footprints resulted in large non-linear errors.

Recommended is to study FODs in samples that are sectioned at a 45 or 60° angle, resulting in large elliptical fibre footprints which are less error sensitive when analysing with the MoE. The induced section angle can easily be transformed back to yield an unbiased FOD measurement.

# Table of content

# Nomenclature

| | |
|---|---|
| 2D | Two Dimensional |
| 3D | Three Dimensional |
| | |
| CF(s) | Carbon Fibre(s) |
| CFRP | Carbon Fibre Reinforced Polymer |
| (μ)CT | (microscale) Computed Tomography |
| | |
| FDD | Fibre Density Distribution |
| FOD(s) | Fibre Orientation Distribution(s) |
| FRP | Fibre Reinforced Polymer |
| FTF | Fibre-to-Fibre |
| | |
| LTP | Low Temperature and Pressure |
| | |
| MoE | Method of Ellipses |
| | |
| OM | Optical Microscopy |
| OoP | Out-of-plane |
| | |
| rCF | recycled Carbon Fibre |
| | |
| SCFs | Super Critical Fluids |
| SCW | Super Critical Water |
| SEM | Scanning Electron Microscope |
| | |
| UD | Unidirectional |
| | |
| vCF | virgin Carbon Fibre |
| $V_f$ | Fibre Volume fraction |
| | |
| $\phi$ (phi) | in-plane angle |
| $\theta$ (theta) | out-of-plane angle |

# 1. Introduction

This chapter introduces the thesis research project. Paragraph 1.1 elaborates on the project background. Paragraph 1.2 explains the research goals, introduces the parties involved and stats the research questions. Paragraph 1.3 outlines the scope of the thesis project. Paragraph 1.4 explains the thesis report structure.

## 1.1 Project background

The aerospace industry has led the field for the past decades in the use of Carbon Fibre Reinforced Polymer (CFRP) to decrease structural weight and increase vehicle performance. But during the last decade, a steady decrease in price [1] combined with emission regulations has caused the aerospace industry to be caught up and even surpassed by the automotive and wind power industry in annual global demand for CFRP. In 2018 the automotive and wind power industry market share accounted for 10 and 24 %, totalling 14 and 34 kilotons in bulk weight respectively, compared to 23% and 32 kilotons for the aerospace industry. The aerospace sector may not be the biggest consumer of CFRP by bulk weight anymore but still accounts for roughly 70 % of global revenue (18 billion dollars) compared to 6 % (1,5 Billion dollars) and 4 % (1 billion dollars) for the automotive and wind power industry respectively. [2], [3] This difference in revenue per bulk weight of CFRP is primarily caused by using lower performance and less stringently certified carbon fibre (CF) and matrix systems by the latter two.

Increasing application for CFRP is eventually followed by an increase in both production and end-of-life (EoL) CFRP waste, giving rise to problems but also opportunities [4]. Currently, there is no industrial CFRP waste management and recycling system which can handle large quantities of waste and produce high-quality recycled carbon fibres (rCF). [2], [5]

The majority of CFRP waste is disposed of as landfill or incinerated for thermal energy, and only a small margin is recycled for new composite products. [6], [7] Here lies an opportunity. In the past decade, increasing awareness of environmental consequences, legislative penalties and economic opportunities in rCF products have spurred the development of recycling- and manufacturing processes. These methods already yield rCF materials with relatively high mechanical properties at a significant cost and emissions reduction. However, these rCF materials still need further improvements to achieve mechanical properties to be deemed sufficient as vital structural components. [2], [8]–[10]

To achieve this higher mechanical performance, rCF materials would need to feature; fibre volume fractions ($V_f$) comparable to virgin CF (vCF) composites, highly aligned and orientated fibres, non-damaged fibre surfaces or sizing and no resin residue or char. To reliably produce these high-performance rCF materials, significant effort has

to be spent in achieving optimal re-manufacturing parameters which manage and control the intrinsic chaotic discontinuous microstructure of raw rCF material. [8] By measuring and quantitively characterising the microstructure, discreet improvements can be made to the production process to manufacture high-performance rCF materials. Unfortunately, such a quantitative characterising framework does not yet readily exist, holding back the development of rCF.

## 1.2 Research goals

The goal of this thesis is to introduce an initial quantitative characterisation method that can assess the microstructural quality of rCF materials. With the prospect of further development to achieve a full quantitative characterisation method of rCF by the Aerospace Manufacturing Technologies (AMT) research group at TUDelft.

To achieve this goal, this current thesis research project was done in collaboration with a CF recycling company and research institute which supplied the rCF material.

To successfully develop the characterisation method, several research questions have been formulated and will be answered in this thesis report. The research questions are:

1. *How can the fibres and morphology in rCF materials be measured?*
2. *Which microstructure is preferred in rCF materials?*
3. *Which parameters quantitatively describe the fibre morphology?*
4. *How well does the method identify fibres and characterise the microstructure?*

## 1.3 Outline and scope

A scope has been defined to establish research boundaries; these are:
Thesis project will incorporate:

- Sample preparation of discontinuous fibre materials.
- Optical microscopy of sample material.
- Method development for fibre identification and tracking.
- Fibre morphology characterisation
- Microstructural comparison between samples with different processing parameters.

Thesis project will exclude:

- Production of the discontinuous fibre material.
- Mechanical testing of the discontinuous fibre material.
- Simulations predicting the mechanical properties.

# 2. Literature review

In this chapter a brief overview of relevant information is giving on topics which are relevant to the thesis content. Paragraph 2.1 describes fundamental mechanisms which dictate the mechanical properties of CFRP. Paragraph 2.2 introduces multiple recycling processes and their influence on CFRP microstructure. Paragraph 2.3 presents manufacturing methods which process rCF material into aligned material, and their effect on microstructure. Paragraph 2.4 reviews the most relevant literature on the characterisation of rCF. Paragraph 2.5 identifies the relevant knowledge gaps.

## 2.1 Mechanical properties of CFRP

Carbon fibre reinforced polymers (CFRP) composites are well known for their superior specific strength and stiffness properties when compared to other engineering alternatives. These respectively high specific mechanical properties originate from the combination of carbon fibre reinforcement and polymer matrix to form what is called a composite, as can be seen in Figure 1.

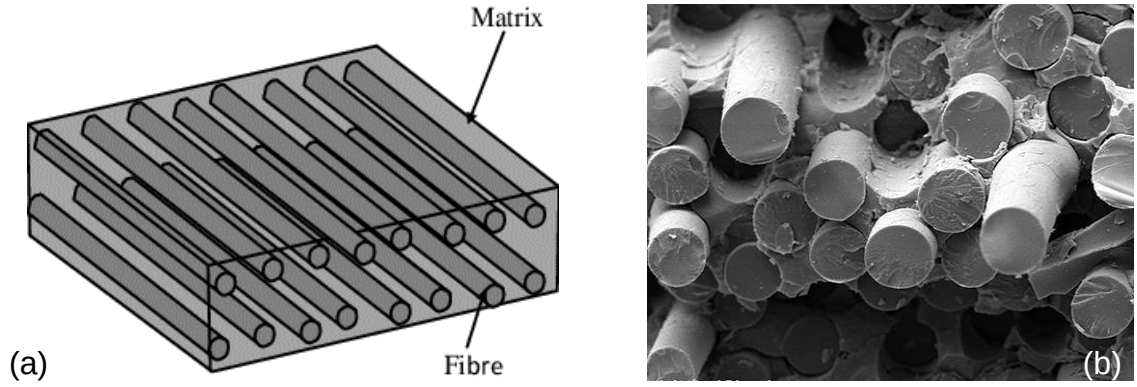


*Figure 1 (a) Simplified representation of straight fibres within matrix to form a composite. [element6composite] (b) Scanning electron microscopy image of a fractured composite surface showing fibres embedded in matrix. [MATECH]*

These carbon fibres, depending on being manufactured as high tensile or high modulus fibres, can have tensile strengths and stiffnesses ranging between 3000 - 6000 MPa and 200 - 600 GPa respectively. The polymeric matrix which can have tensile strengths up to 100 MPa and moduli ranging between 3 - 5 GPa adds relatively no tensile strength and stiffness properties to the composite when compared to CF's. However, the matrix is vital in a composite as it adheres the CF's together, allowing distribution of shear stresses. This interface shear strength (IFSS) is an essential part of the composite overall mechanical performance and is greatly dependent on the CF surface treatment. This surface treatment is mostly done by etching and coating, or so-called sizing the fibres with a minute layer of polymeric resin or reactive agent, promoting physicochemical bonding of functional oxygen and/or nitrogen groups on the CF surface with matrix. [11]

Besides the effectiveness of adhesion between fibres and matrix, another crucial determining factor to the mechanical properties of a CFRP composite is the orientation of CF reinforcement within the composite. Being that CFs best resist tensile strain, a composite has optimum strength and stiffness properties when the alignment of fibres is parallel to that of the applied tensile load. When loaded at an angle out of parallel to the fibre direction, the composite performance decreases sharply and continues to decrease rapidly to roughly the matrix strength and stiffness when loaded perpendicular to the fibre orientation [12], [13] as illustrated in Figure 2.

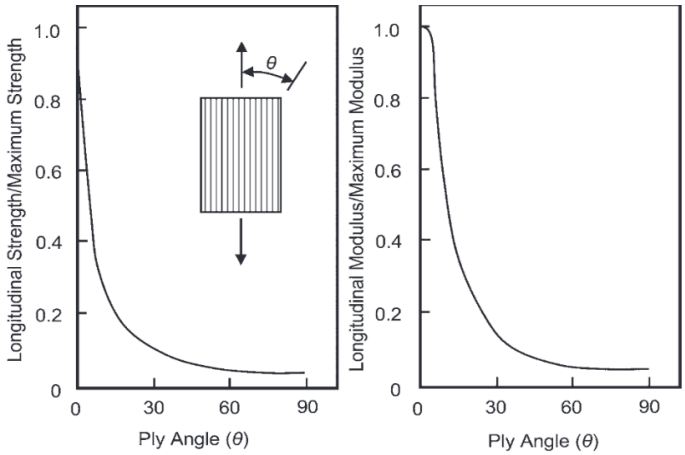


*Figure 2 Change of composite strength and stiffness as a function of fibre orientation [Structural Composite Materials - F. C. Campbell 2010]*

To cope with this intrinsic behaviour during the operation where the angles and magnitude of loads vary, a specific amount of fibre layers (plies) in exact orientations can be stacked on top of each other in a so-called tailored layup. The combination of these layers forms the composite laminate.

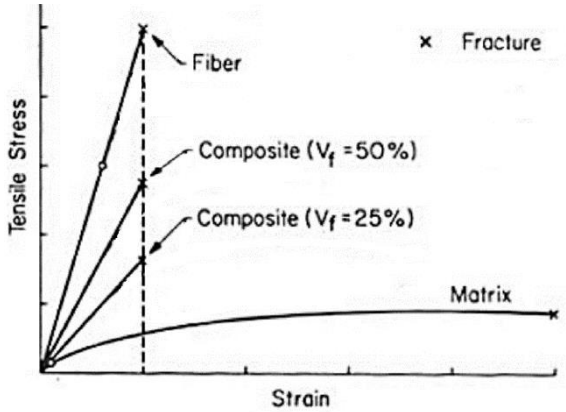


*Figure 3 Maximum tensile stress of a composite with changing fibre volume fraction [International Journal of Lightweight Materials and Manufacture May 2020]*

Another indicator for composite quality is the distribution of fibres and fibre volume fraction ($V_f$). The more evenly distributed CF reinforcement a CFRP composite contains, the stronger it gets as represented in Figure 3. This statement holds true until the point where the Vf is too high (>65~70 %) causing the efficiency of matrix wetting to decrease causing local dry spots. [12], [14]

When the composite features discontinuous fibre, an additional factor that strongly affects the mechanical properties is the length of CF reinforcements. When a matrix volume containing a discontinuous fibre is deformed by tension, the fibre and matrix will experience a difference in strain caused by their greatly different moduli, as illustrated in Figure 4a. This difference in strain causes shear stresses across the fibre-matrix interface which loads the fibre with tensile stress according to the shear lag model, as illustrated in Figure 4b.

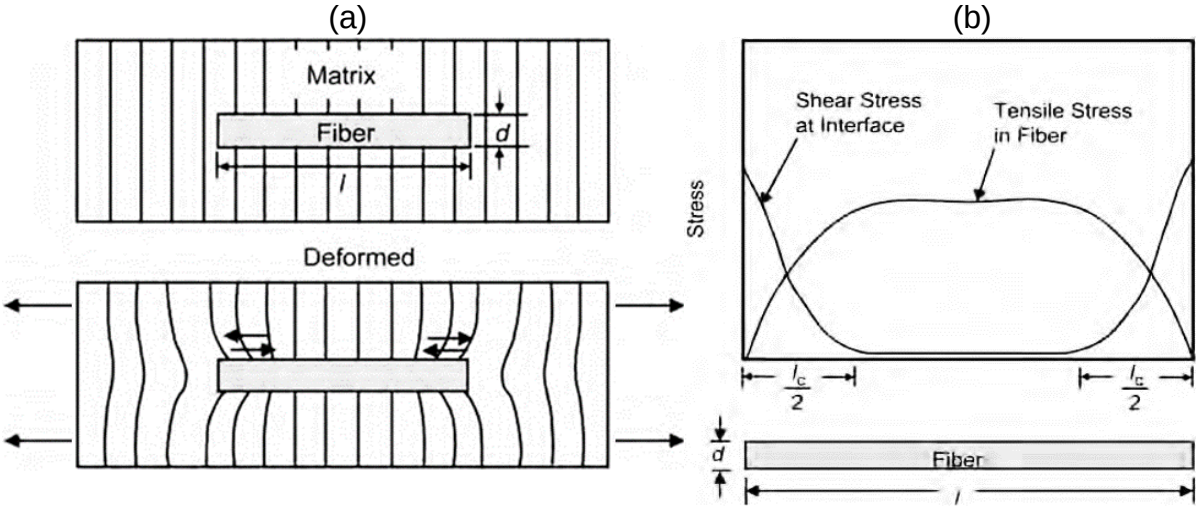


*Figure 4 (a) Visualisation of the effect of deformation in a matrix on strain around a fibre. (b) Shear and tensile stresses in discontinuous fibre [Structural Composite Materials - F. C. Campbell 2010]*

If the fibre length ($l_\mathrm{f}$) is longer than a certain critical length ($l_\mathrm{c}$) the shear stress converges to zero at a distance of $l_\mathrm{c}/2$ from the ends. In contrast, the tensile stress is zero at the free fibre end and reaches a maximum when the shear stress reaches a minimum, assuming a perfect bond between fibre and matrix. When $l_\mathrm{f} > l_\mathrm{c}$ a plateau forms where the tensile stress in the fibre is maximum as can be seen in Figure 4b. This plateau means that along this length the tensile stress is fully carried by the fibre and not the matrix. This makes the effective load-carrying capacities of the fibre larger, increasing the tensile strength of the composite. This $l_\mathrm{c}$ is thus important and can be calculated by,

$$l_c = \frac{\sigma_{tu}}{2\tau_i} d_f \tag{1}$$

Where the ultimate fibre strength is $\sigma_\mathrm{tu}$, the shear strength of the fibre-matrix interface is $\tau_\mathrm{i}$ and $d_\mathrm{f}$ is the fibre diameter. Note that the assumptions behind Figure 4 do not consider the interaction between other neighbouring fibres.

Whenever multiple fibres are closely packed and positioned alongside each other with a discontinuity in an adjacent fibre, a stress concentration arises around that fibre end, as can be seen in Figure 5a. When multiple discontinuities from neighbouring fibres are present, a single fibre can experience multiple stress peaks over its length as illustrated in Figure 5b. [15]–[18]

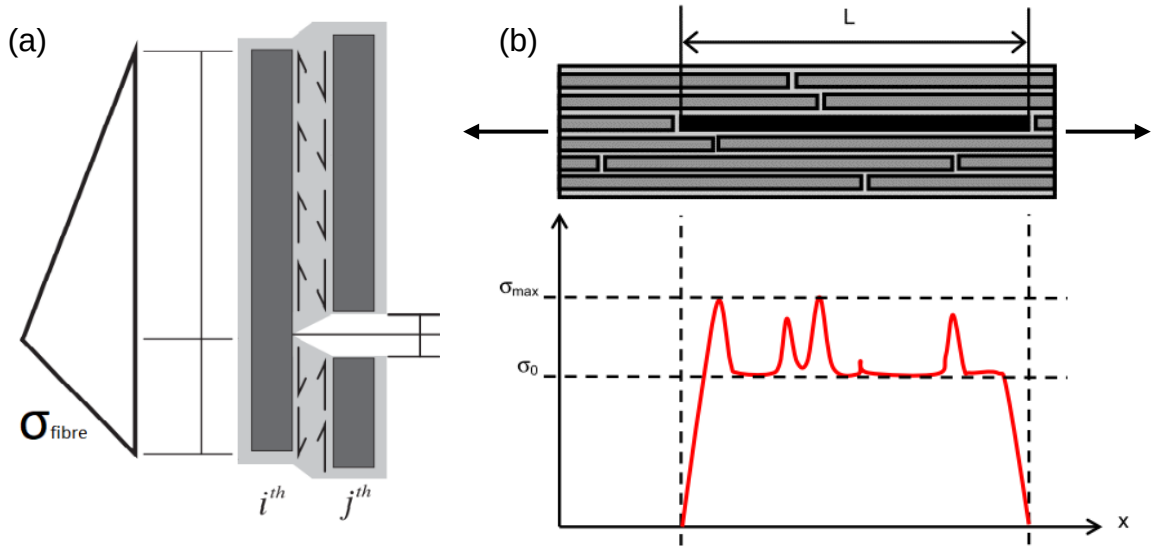


*Figure 5 (a) Representation of peak stress in the i-th fibre by shear stress transfer from the neighbouring j-th discontinuous fibre, as inspired by [J. Henry, S. Pimenta 2017], (b) Stress distribution in a staple fibre composite material. [Gillet et al. 2015]*

This conglomeration of stress concentration causes the peak stress in the fibre and matrix to exceed their maximum strength, initiating fracture and crack formation. [18] By further increasing the fibre length, the total amount of fibre ends in the composite is reduced, decreasing the number of stress concentrations while also statistically reducing the likelihood that stress concentrations are near each other. [17]
In theory, when $l_f > 5\, l_c$ roughly 90 % of the tensile strength and 95 % of the tensile modulus can be achieved when compared to continuous fibre composites. [12], [19], [20] In reality, discontinuous composites with fibre lengths $> 5\, l_c$ scarcely achieve strength and stiffness properties comparable to those of continuous composites. The discontinuous microstructure is challenging to control because the fibres are difficult to perfectly orientate and align. Thus, the mechanical performance of discontinuous composites is among others also heavily dependent on the microstructural control and parameters of the manufacturing process.

The microstructure of discontinuous composites varies greatly from that of continuous fibre composites. The discontinuous microstructure is particularly hard to control and still highly heterogeneous after an effort is spent to align the fibres, as can be seen in Figure 6b. These realigned discontinuous unidirectional materials can have average orientations within ±5° deviation of Unidirectional (UD) [21] but will be highly aligned in some areas and more disperse in others causing heterogeneity. Notably, the material often features both in and out-of-plane (OoP) fibre misalignment, where fibres weave over and underneath each other causing disrupted microstructures, as again be seen in Figure 6c. Furthermore, single fibres which have large misalignments in an otherwise highly orientated and densely packed microstructure can lead to a disruption in fibre packing. This disruption in packing affects the maximum transferable shear stresses and Vf on a local level by causing a resin-rich layer in between fibres, as can be seen in Figure 7.

To summarise, the mechanical property of a composite is heavily determined by the following features.

- Individual mechanical properties of both fibre and matrix.
- Fibre-matrix interface shear strength (IFSS).
- Fibre orientation & alignment.
- Fibre volume fraction ($V_f$)
- Fibre distribution.
- Fibre length.

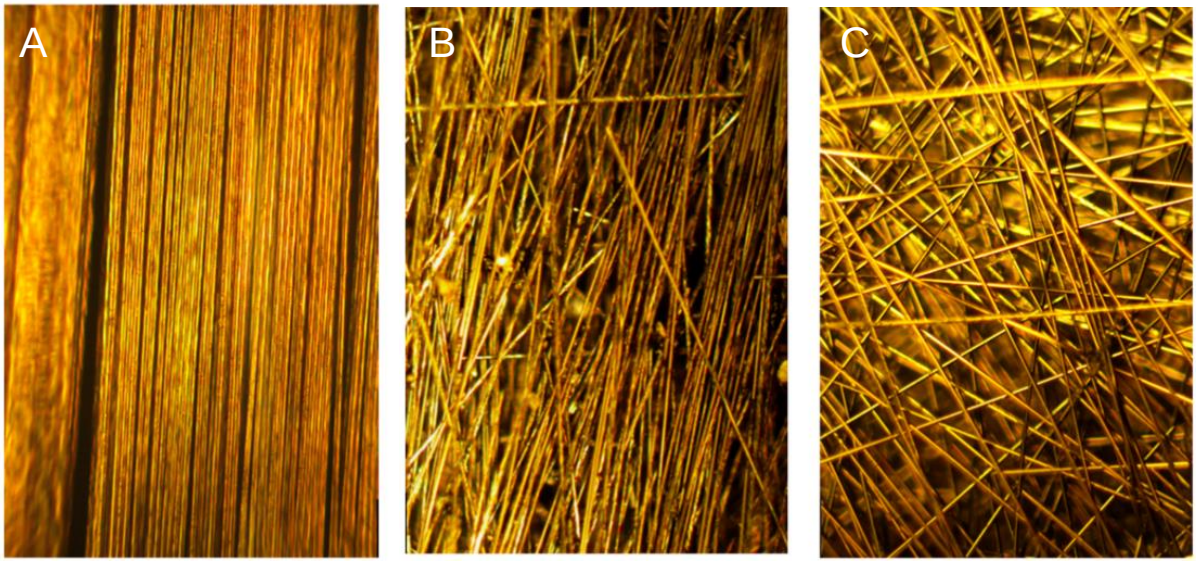


*Figure 6 (A) UD aligned vCF, (B) re-aligned rCF and (C) non-aligned rCF [Werken et al. 2019]*

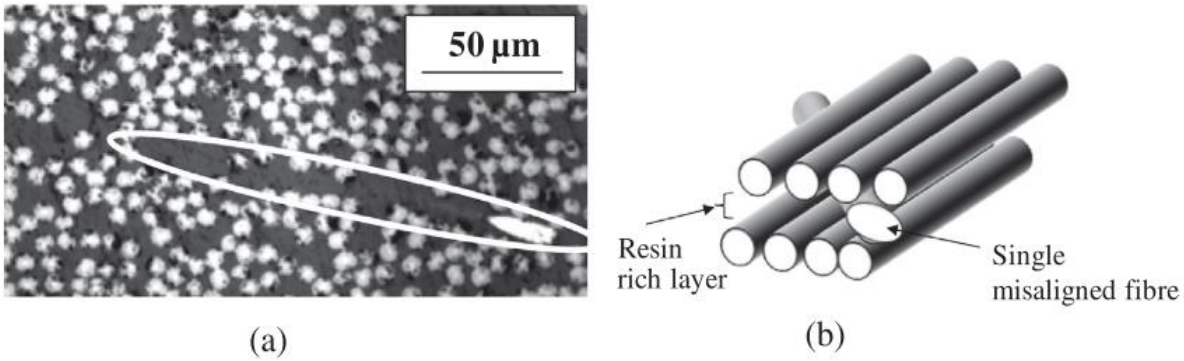


*Figure 7 (a) single misaligned fibre in the microscopy specimen causing resin rich area. (b) schematic representation of single misaligned fibre in the specimen in a 3D structure [Yu et al. 2014]*

## 2.2 Recycling of CFRP

CFRP waste originates from two distinct sources,

1. Manufacturing processes
2. End of life (EoL) components or vehicles.

A further specific distinction can be made about the physical state of the various types of waste. This distinction is of importance because different types of waste require different types of recycling processes. The different types of CFRP waste are:

1. Dry fibres,
2. Uncured fibres,
3. Cured materials.

The first two types of waste can only be contributed to manufacturing sources, whereas the last one can occur with both manufacturing and EoL. All three types of waste are likely to be contaminated with unwanted materials which must be separated from the valuable CFs before or during the recycling process, after which the fibres can be reclaimed to be used for rCF.

Dry fibre waste materials are typically offcuts or leftover materials which have not been wetted by resin or other chemicals. Therefore, when compared to the other two types of waste, dry fibre is normally less severely polluted and can be more easily separated into useable aggregate. Dry fibre waste contaminants frequently come in the form of cardboard rolls or bobbins where the fabrics and tows are stored on, pieces of adhesive tape, packing material and miscellaneous single-use production items such as gloves as can be seen in Figure 8.

Uncured waste shares the same manufacturing contaminants as dry fibre waste but should be handled differently compared to dry and cured waste. As it is classified as chemical waste since the fibres are wetted with resin or other chemicals and are still uncured, thus chemically active. The common industry practice is to cure the waste product with either heat or chemicals to dispose of it as normal waste. The uncured waste can originate from failed curing or resin mixing procedures, out-of-spec and out-of-life rolls of prepreg, but the majority consists out of prepreg offcuts which include release films as can be seen in Figure 9.[22]

Cured waste can be scrapped out-of-spec parts or CFRP moulds but is generally EoL. This waste is significantly different from the cured manufacturing waste because it is assembled and bonded with dissimilar materials such as adhesives, dissimilar fibres, foams, metals and paints. This requires the EoL waste components and vehicles to be disassembled and crushed into smaller dimensions after which dissimilar materials can be filtered out, as can be seen in Figure 10.

*Figure 8 Dry fibre production waste contaminated with various items as received by RecyCarb [Hofmann et al. 2019.]*

*Figure 9 Uncured waste consisting out of prepreg offcut and release film originating from the cutting manufacturing step. Left image [Nilakantan et al. 2015] - Right image [ELG Carbon Fibre Ltd.]*

*Figure 10 EoL waste scrap CFRP A320 tail section [Aero circular NV]*

In a real industrial CFRP recycling process, CFs are reclaimed from various sources which contain different types of CFs and resins. They are processed together in the recycling stages, essentially becoming a mix of rCFs. Consequently, the mechanical properties of industrial rCF can become inconsistent after the recycling processes when a small selection of fibres is tested. This is because mechanical properties now depend on the composition and mixing of waste feedstock, besides the recycling treatment conditions. Thus, making it hard to quantitatively compare properties of industrial rCF with those of vCF, making a compromise necessary to accept a distribution of properties. [5], [7]

As a clarification for the various CFRP waste origins, types and recycling processes a flowchart depicting the routes is given in Figure 11. In the following four paragraphs, the mechanical, chemical and thermal recycling processes are further described, after which the reprocessing of the recycled CFs is discussed.

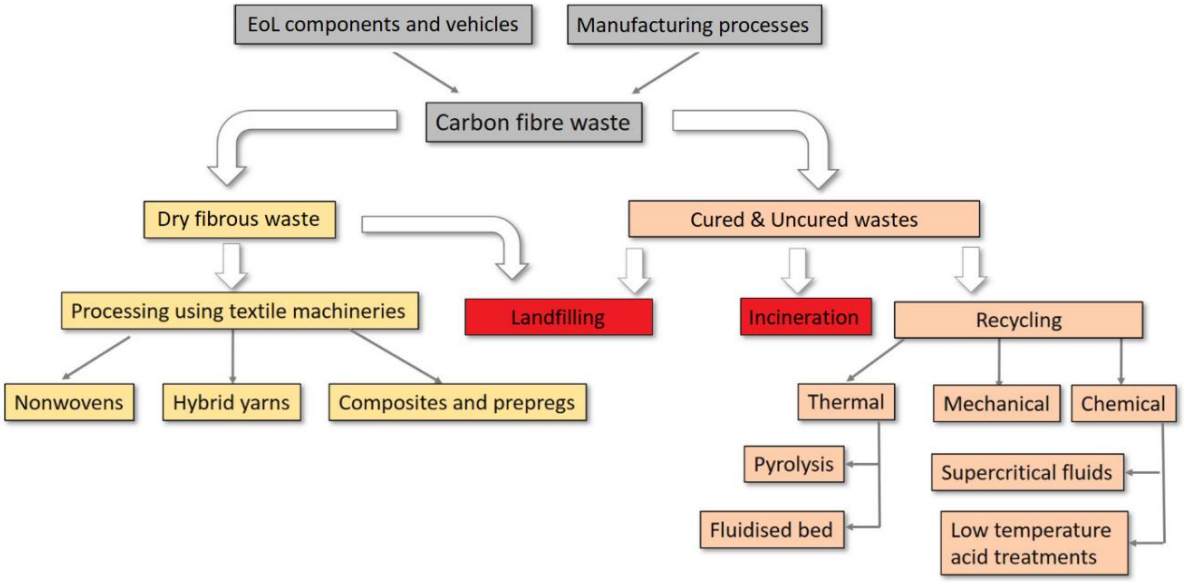


*Figure 11 various recycling routes depending on waste origin and waste type [modified from E. Pakdel et al 2021]*

### 2.2.1 Mechanical recycling

The mechanical recycling process is generally the first step for all CFRP recycling activities. After which, it is further processed by either chemical or thermal recycling methods.[5] The reason that chemical and thermal recycling methods usually cannot handle larger sized waste products. The waste can be reduced in size by either crushing, grinding, milling, and shredding. The specific size reduction can be altered and is depended on the capacity of the following recycling process and intended use of the recyclate.[2], [5] Generally, the size and related fibre length of the recyclate is tried to be kept as large as possible. Alternatively, the recyclate can be additionally mechanically processed by being grounded and milled into fine powder filler material for injection moulding, which is generally considered as downcycling.[23], [24]

Cured and EoL waste is most commonly crushed and shredded into flakes, as can be seen in Figure 12, which then can be further processed by either chemical or thermal methods. Dry fibre waste which has not been wetted by resin or other chemicals during the manufacturing of CFRP composite parts is most ideal for recycling. It has minimum impurities or likewise has easily removable contaminations and has identical mechanical and handling characteristics as vCF.
After the removal of possible foreign bodies, it can be processed using traditional textile processing methods for instance separating carding and spinning the fibres into veils, slivers, and yarns. These products can be used for reinforcements in (non-)woven fabrics and staple tapes, sheet- and bulk moulding compounds (SMC & BMC respectively). [2], [5], [10], [24], [25]

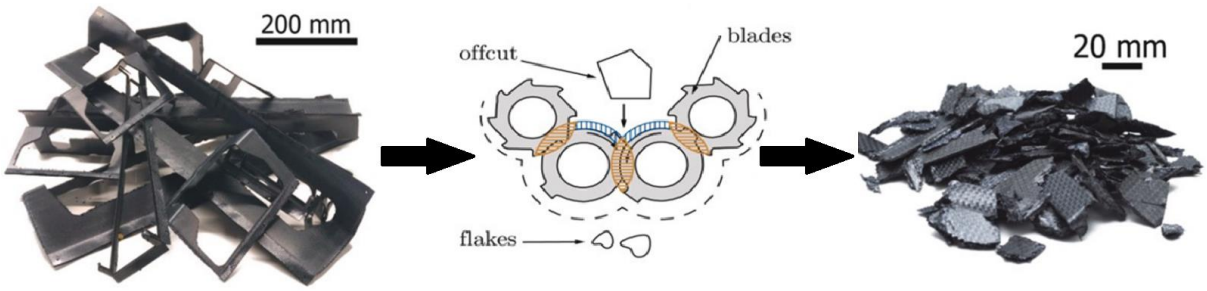


*Figure 12 Mechanical shredding of cured offcut waste, resulting in flakes [source TPRC]*

The biggest advantage to the mechanical recycling process is that it is a fast and cheap way of handling large amounts of waste, of which the various end product can be used in numerous industries. The biggest disadvantage is first and foremost the discontinuous fibres having lesser mechanical properties when compared to continuous vCF composites.

### 2.2.2 Chemical recycling

Chemical recycling methods mostly use solvolysis to decompose the matrix to recover the CFs from the composite. A wide range of solvents and different processing parameters are possible to decay the original polymeric matrix into low molecular weight polymers or monomers, leaving clean and undamaged CFs, as seen in Figure 13d. [2], [9], [26] The processing parameters can vary depending on the resin and solvents used, the recycling process can be done at room temperature or well above 300°C, at ambient or elevated pressures reaching over 200 bar which can lead to near- or supercritical conditions. [5] The solvolysis recycling process is usually classified into supercritical (SC), near critical and subcritical (subC) conditions, and on the basis of the reactive medium.[10]

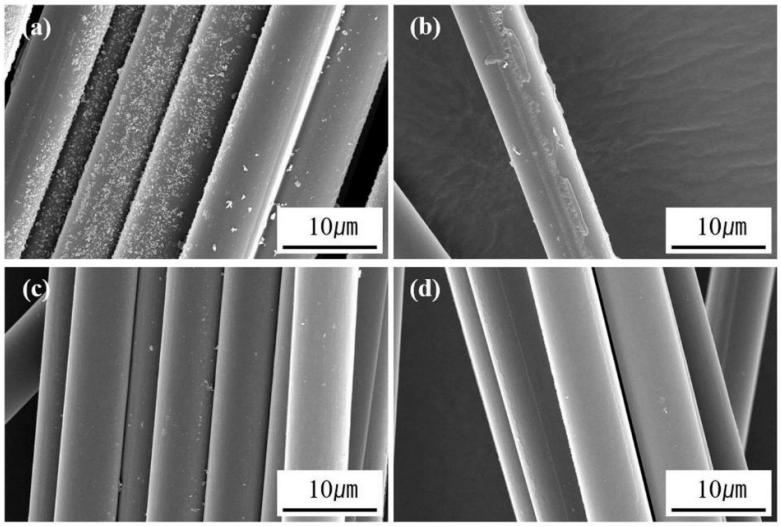


*Figure 13 SEM images of rCF after supercritical water (SCW) treatment at 405 °C and 280 bar (a) 10 min, (b) 30 min, (c) 60 min, and (d) 120 min treatment, respectively [Y. Kim* et al. 2019 ].

The near and supercritical fluids (SCFs) have characteristics such as gaseous viscosity, high diffusivity and can dissolve large amounts of resin components. The SCFs ability to dissolve the polymeric components allows them to additionally reclaim the polymeric matrix component. The temperature and pressure parameters allow an added capability of controlling solvent properties and reaction rates for achieving optimal processing conditions.

Depending on solvents and processing parameters, the various SCF recycling methods can achieve a matrix removal efficiency between 90 % and 100 %, retention in tensile strength of 60 to 100 %, and interface shear strength of 80 to 100 %. [2], [5], [6], [9], [27]

The general solvolysis processing steps are: First, diffusion of the solvent into the composite. Second, the SCF interacts with the polymeric matrix breaking covalent bonds. Third, dissolution of matrix compounds into SCF. [2], [5], [9]

Supercritical water (SCW) has been intensely researched for use in solvolysis, mainly due to its nontoxicity, recyclability and ease of controlling properties by processing parameters. In supercritical conditions (T>374°C and P>221 bar) water acts as a solvent that can easily dissolve organic compounds. Alternative solvents like alcohols and ketones with lower critical conditions (200–300°C and 20–60 bar) have been used separately or in combination with pure water with success. [9] The reaction rate, efficiency and processing control of resin decomposition by SCW mixtures can be accelerated and improved by the addition of acidic, alkaline and catalysts mixtures, as well as adding oxygen into the systems. [9], [26] The downside to these various additives is that the resultant solvent waste product is now more hazardous and toxic compared to the one resulting from pure SCW, thus their environmental effects should be considered. [2], [5], [26]

Both the composite resin system and the size of the recyclate dictates the solvolysis processing parameters and efficiency. For smaller sized aggregate, the performance

of the recycling process is not limited by diffusion of the solvent through the part. However, for larger parts that are treated in industrial-scale reaction vats, diffusion of the solvent over a larger distance through the part becomes limiting. The efficiency of the recycling process is also affected by the amount of dissolved matrix in the solvent. If greater amounts of composite waste are recycled in the batch reaction vat, or the solvent is used multiple times, the solvent becomes saturated, and the decomposition rate is slowed down. Another negative effect of having a saturated solvent is that reactor vat and recovered fibres are coated with organic residue that requires additional rinsing besides the usual after treatment. Semi-continuous reaction processes have been under development to improve the diffusivity and reaction rates of the recycling process, which in turn reduce the duration of the solvolysis process. The reduction in contact time between CFs and saturated solvent reduces the chance of the formation of residue on the fibres. [2], [5], [6], [26]

Using SCFs requires specific equipment which can handle and control the high pressures and temperatures, making it an expensive and energy-intensive process. Therefore, recycling studies have focused on developing less demanding conditions for the chemical degradation of the matrix, operating at temperatures below 200°C and at or near ambient pressures. These low temperature and pressure (LTP) recycling methods use pre-treatments, acids, catalysts or other types of reactive solvents [9]. The pre-treatment is usually done to swell the polymer matrix and accelerate the interactions with the catalysts or acids. The catalysts and acids diffuse into the crosslinked polymer network, breaking the covalent bonds degrading the matrix. To accelerate the process further, the mixture can be agitated by stirring, microwave radiation or ultrasonic vibrations. The effects of LTP solvolysis on fibre properties are comparable to those of SCFs. [5], [6], [9] The biggest downside of LTP recycling methods is that the use of more reactive acids, catalysis and solvents results in more dangerous waste products which are difficult to dispose of or to recycle without damaging to health and the environment.

The biggest advantage of solvolysis compared to other recycling processes, is that both SCF and LTP methods can achieve clean, matrix-free and undamaged CFs with similar mechanical properties compared to vCFs. The chemical recycling process by SCF solvolysis is more easily controlled by processing parameters when compared to LTP, its diffusivity and reaction rate can be monitored and adjusted while the process is ongoing. The LTP process is harder to control while the solvolysis process is in progress since this method functions on the reactivity of the solvents used in the process and less so on temperature and pressure. However, SCF reactors are expensive since they must withstand high temperatures and pressures, along with being corrosion resistant if the SCFs are modified with reactive additives. The LTP methods are cheaper to use since they require lower temperatures and pressures compared to SCF, but still require specific types of reactors and facilities capable of handling highly corrosive environments and waste products.

### 2.2.3 Thermal recycling

In the thermal recycling methods, fibres are reclaimed from their composite by thermally decomposing the polymeric matrix. These techniques additionally allow the recovery of inorganic fillers, inserts and in some cases the polymer resin components as oil and tar. The two thermal recycling methods that are most common, are pyrolysis and fluidised bed recycling.

Throughout the industry, pyrolysis has been the most widely implemented method of composite recycling by which fibres are reclaimed for rCF composites, as it can be run continuously and handle larger CFRP waste parts which could still contain dissimilar materials, such as adhesives, metals, dissimilar fibres, foams, and paints as can be seen in Figure 14

*Figure 14 (Left) End of life component before pyrolysis, (Right) End of life component after pyrolysis [CFK Valley Stade Recycling GmbH]*

During the pyrolysis process, CFRP waste is heated to 400 – 700°C in either a reactive, inert or super-heated steam environment to volatilize or decompose the polymer matrix into gas, oil or char.[27] After this initial pyrolysis process, the CF surface is covered with residue from the decomposed polymer matrix, as can be seen in Figure 15b.

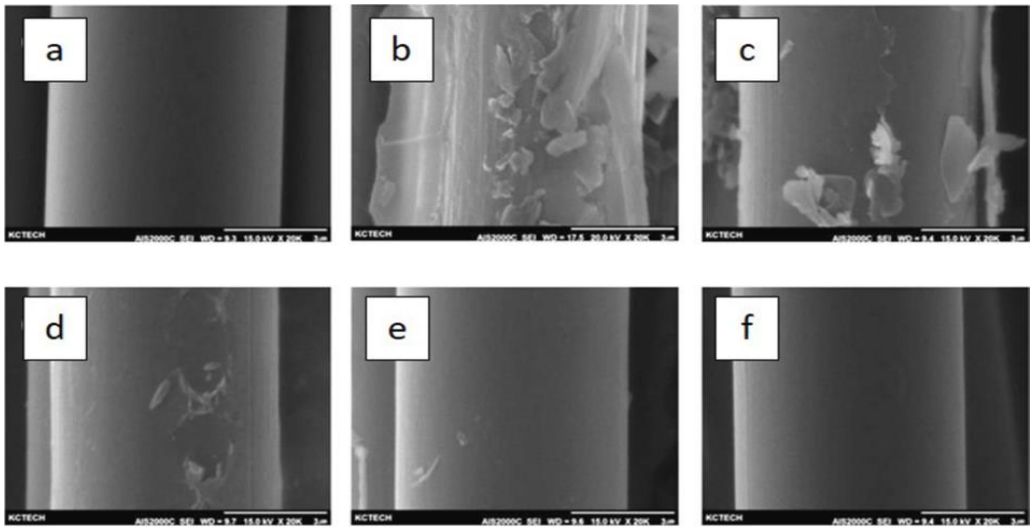


*Figure 15 SEM images of a) clean vCF, b) CF after steam pyrolysis at 550°C. rCF after steam/air process treated for c) 30 min, d) 45 min, e) 60 min, and f) 75 min [K. W. Kim et al. 2017]*

To remove the matrix residue, the CFs are post-processed in heated synthetic air ($N_2$+ $O_2$) or pure oxygen at 300-500°C to carbonize the matrix residue. This post-pyrolysis oxidation treatment is the most critical step in retaining the mechanical properties of the fibre, as it can easily damage the fibre surface because the fibre is no longer protected by the matrix, damage can be seen in Figure 16. [2], [5], [6], [9], [10], [28]

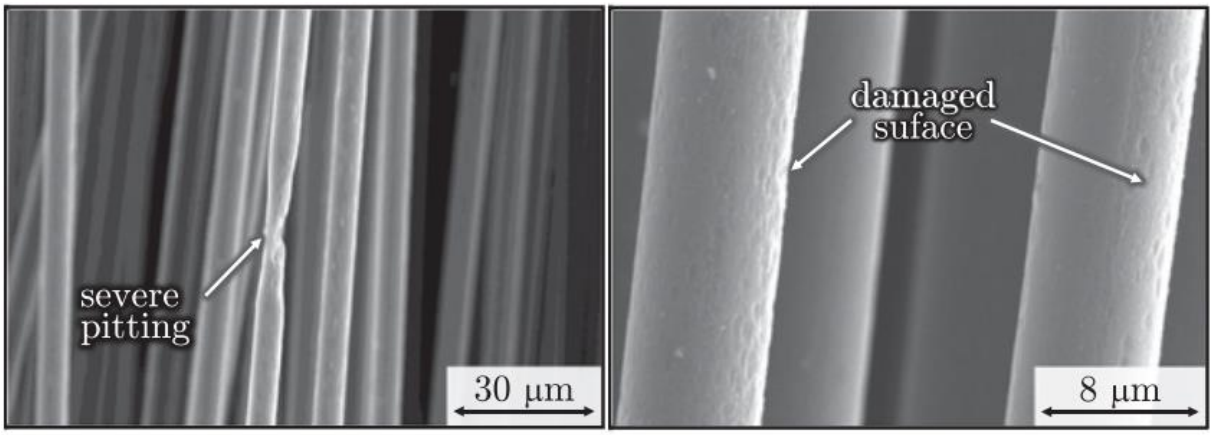


*Figure 16 SEM images of rCF showing pitting and surface damage after aggressive pyrolysis cycles [Gopalraj et al. 2020*

By increasing the oxidation temperature, the efficiency and required time to remove the char layer from fibre surfaces is shortened, however, the higher post-processing temperatures in either oxygen or synthetic air have a higher potential of damaging the CFs, as can be seen in Figure 17. It also appears that various types of CFs from separate manufactures experience different levels of degradation at different temperatures.

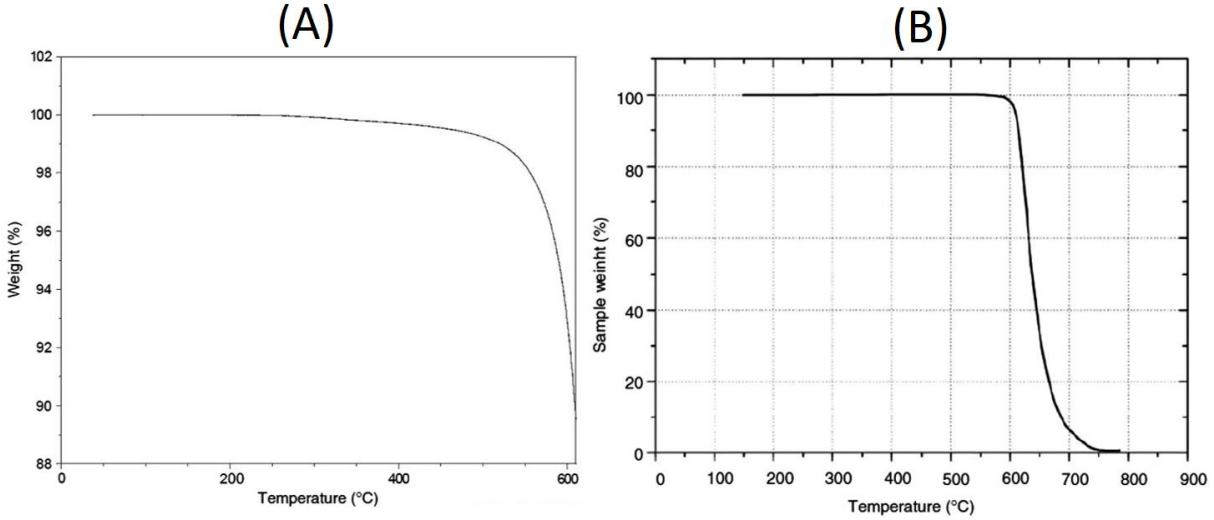


*Figure 17 Effect of post-processing parameters on weight reduction of CF by Thermal Gravimetric Analysis (TGA) (A) Hexcel AS4 carbon fibres in oxygen, (B) TGA of Toho-Tenax HTA carbon fibres in synthetic air. [Oliveux et al. 2015]*

There is also a possible formation of functional oxygen groups on the fibre surface by post-processing oxidation to be considered. These oxidised functional groups can increase the surface energy and create formation sites on the fibre surface which

promote covalent bonding with new resin, increasing the interfacial shear strength (IFSS). For some cases, this can result in rCF composites demonstrating similar mechanical performances in terms of strength and modulus as vCF composites.[27] Depending on processing conditions, tensile strength and modulus of the fibre can be reduced by 85 % or be almost equal to the vCF. Where the industry average is around 80-90 % retention of mechanical properties of the fibres, after mixing of fibre feedstock to get less variation in final properties.[2], [5], [6], [9], [10]
The optimisation of processing conditions, such as time, temperatures and atmosphere for the initial pyrolysis and secondary oxidation thus play a great role in the retention of mechanical properties.

An alternative to conventional pyrolysis is the fluidised bed recycling process, which uses a bed of silica sand fluidised by heated air between 450 – 550 °C. The fibres are recovered by degrading and vaporising the polymeric matrix with heat and attrition caused by the silica particles. The process only accepts smaller CFRP waste (6–25 mm). [24], [29] The recovered fibres are released from the fluidised bed and moved by the hot air to a collection chamber. After which the fibres need a post-oxidation process to remove residue [4], [29], the process flow can be seen in Figure 18. In terms of mechanical properties, the recycled fibres experience typically a 20 % reduction in their tensile strength due to the attrition caused by the silica particles and lower process control over the effects of the oxidizing atmosphere on the fibres. [6], [24]
The benefit of this process is that mixed and contaminated materials can be processed, therefore particularly suitable for end-of-life waste. The shorter length recovered fibres (typically between 5 -10 mm) which are an effect of the smaller feedstock and broken fibres during recycling are highly suitable for bulk- and sheet moulding compounding (BMC & SMC), and injection moulding methods. [5], [24]

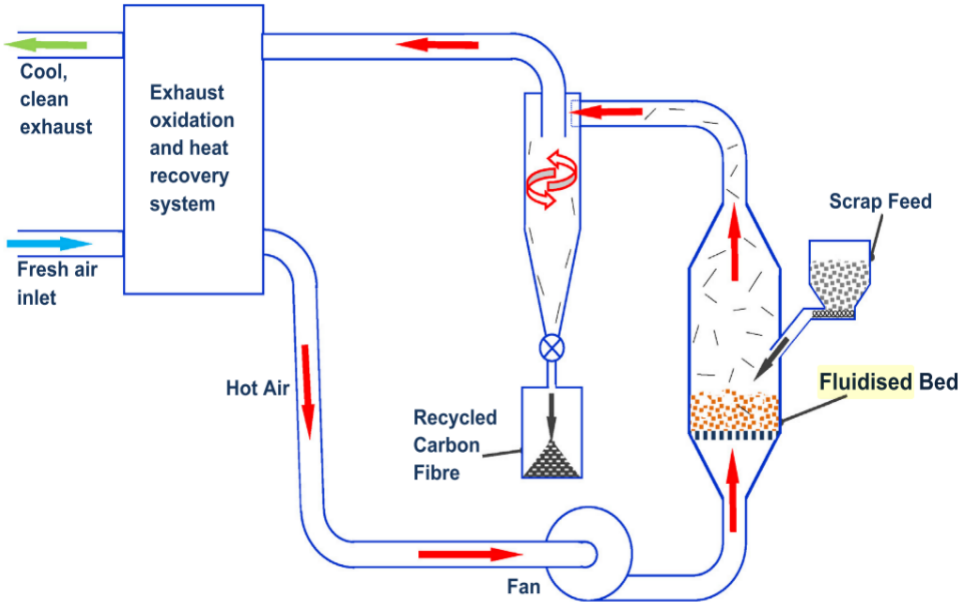


*Figure 18 Fluidised bed components and process flow [Meng 2017]*

## 2.3 Processing and aligning recycled CF

The rCFs are in a discontinuous and disordered fluffy state after the recycling process, as can be seen in Figure 19. Preventing them from being directly reprocessed into fabric and tape materials like their continuous vCF relatives. This recycled fluffy material thus must be reprocessed into a product that can be used to manufacture rCF composites. The fibrous recyclate can be either left disorientated and processed in sheet and bulk modulus compound (SMC or BMC) for compression moulding or realigned by various techniques to yield materials with higher mechanical performance. It has been shown that when these realigned discontinuous fibre composites have 85 % of their fibres aligned within ±5º from perfect alignment possess comparable properties to continuous fibre composites [21]

*Figure 19 Randomly orientated discontinuous rCF fluff [Pickering et al 2016]*

Examples of developed techniques for realigning rCF are based on the Explosives Research and Development Establishment (EDRE) process sprays a slurry of short CFs in water suspension onto a rotating drum, as can be seen in Figure 20, to realignment the rCF into non-woven staple materials with roughly 90 % of fibres aligned within ±15°.[4], [30]

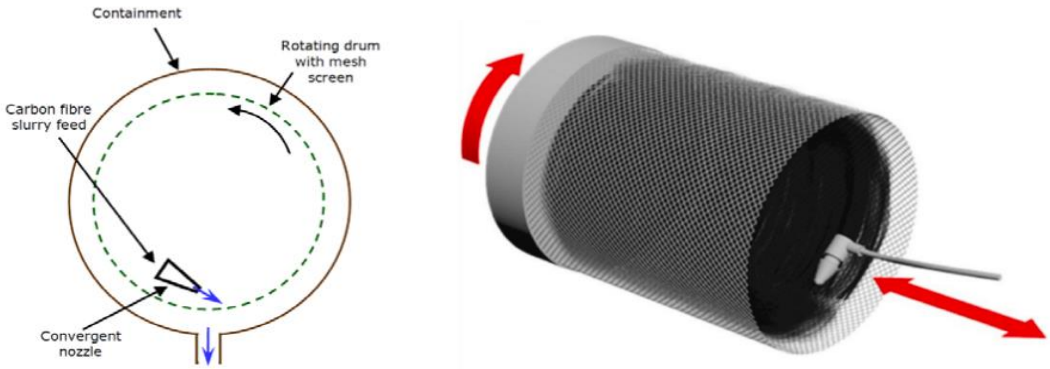


*Figure 20 centrifugal spinning drum with deposits short fibres by water flow in the rotational direction source left Wong K et al. 2010 and right [Werken et al. 2019]*

Another novel realignment technique that uses water as transport media to realign short fibres is the High-Performance Discontinuous Fibre (HiPerDiF) method under-developed since 2014 at the University of Bristol.[21] This technique realigns the fibres by spraying a water-fibre mixture against a vertical plate causing them to align with the plate surface and being deposited on a conveyor belt underneath the plate, as can be seen in Figure 21. $V_f$ up to 55 % with 67 % of fibres being in the range of ±3° to the alignment direction were reported in compression moulding.[31]

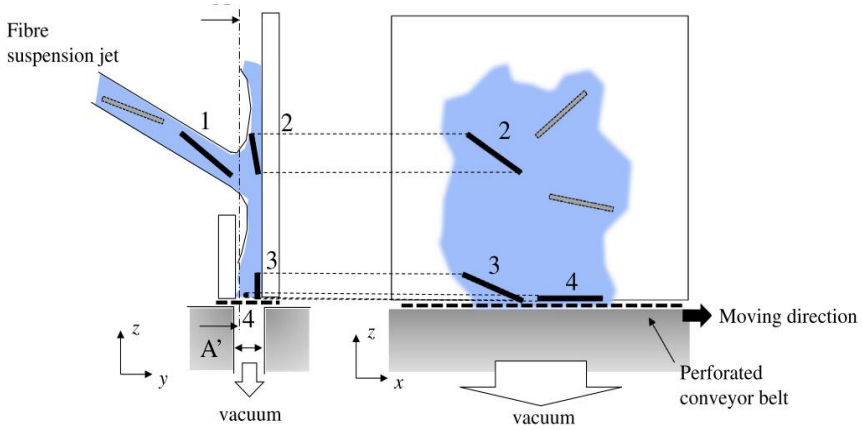


*Figure 21 Schematic drawings of HiPerDiF method. [Yu, H. et al 2014]*

When long fibres (>30mm) have to be realigned, the two previously mentioned wet alignment techniques are not viable. Longer fibres get entangled causing them to clog the flow system or warp when being deposited, causing a lower degree of alignment and stochastic microstructure decreasing the Vf significantly. [21] Because of this, dry realigning methods for the processing of long fibres are more effective. Recent studies have repurposed tried and proven traditional wool and textile processing methods like carding and yarn spinning for dry processing successfully.


*Figure 22 A. CF and PA6 Feedstock. B First & second Opening C mixed feedstock [ J. Wellekötter et al. 2020]*

The process generally starts with opening the feedstock to get less entangled CF bundles while simultaneously mixing in a thermoplastic processing fibre, as can be seen in Figure 22, which binds the fibres after applying heat in a later processing stage. These thermoplastic processing fibres typically consist out of polyamide (PA) or polypropylene (PP), the mixing ratio compared with CF varies between 10 – 70 %. [9], [32], [33] The first step in realigning the rCF involves the carding process, as can be seen in Figure 23. The carding process uses multiple rollers and drums which have various length metal pins that comb the fibres, ideally dispersing, eliminating

entanglements, and orientating them into a web. During this carding step, the fibres stand the biggest chance of being damaged and being reduced in length by the pins, for these reasons the processing must be as gentle as possible. In the second stage, the carded fibres are stripped from the main cylinder by the doffer drum to form a sheet or web preform.

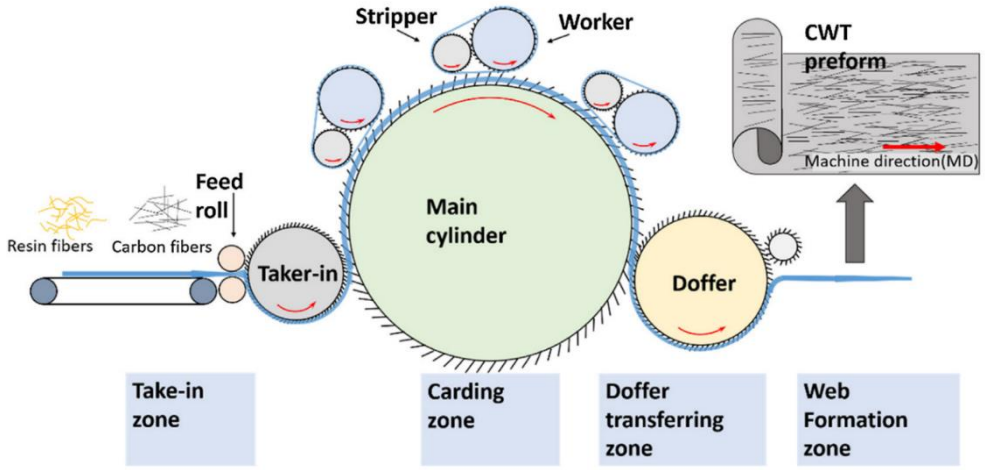


*Figure 23 schematic representation of the carding process [ B. Xiao, et al. 2019]*

The sheet or web preform which is produced by the carding process can already be used in moulding processes. [33] But to further improve the fibre alignment and thus improve mechanical properties a subsequently stretching or drafting process can be applied. This process stretches or drafts the web by feeding the material into a pair of rollers that have different rotation speeds further increasing the fibre orientation in the drafting direction, as can be seen in Figure 24. This process can be repeated multiple times, further increasing the fibre orientation and length of the web which alternatively can be folded and spun into a sliver for yarns and tapes capable of achieving over 80 % of their fibre orientation distribution (FOD) within ±10° of unidirectional. [9], [33], [34] At this drafting processing step the stretched material is normally heated to melt the thermoplastic processing fibre to bind the fibres together fixing the orientation in place so the material can be handled.

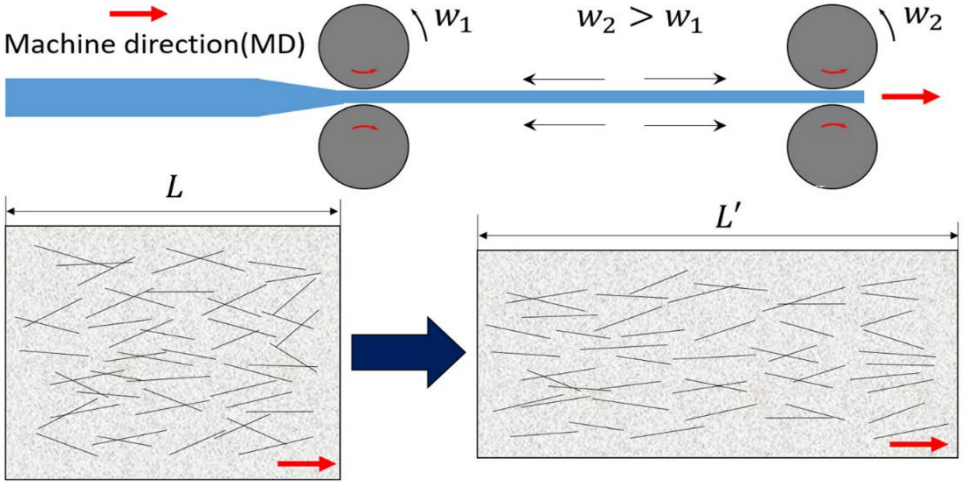


*Figure 24 schematic of the stretching / drafting process [B. Xiao, et al. 2019]*

## 2.4 Microstructural characterisation of discontinuous CF

The majority of the studies which report on the microstructural characterisation of discontinuous CFRP composites do so on injection moulded composites. These feature comparability low Vf, more diffuse fibre orientation and alignment distributions when compared to realigned discontinuous CF. Almost all apply the method of ellipses (MoE) to analyse the fibre orientation and report their results by comparing the change of orientation tensor components (see paragraph 3.2) through-thickness or at different distance intervals.

Examples of these studies are; Vélez-García et al. [35] which applied a modified version of the MoE to characterize orientations in a short fibre injection moulded disk. The method studied elliptical and non-elliptical footprints on small cross-sections. The study reported on fibre orientation by tensor matrix components acquired from plasma etching measuring the unambiguous fibre angle to derive the 3D fibre orientation. Hofmann et al. [36] reports on the results from a MoE analyse applied to injected moulding composites disk which features semi-flexible long fibre paths. Régnier et al. [37] introduced a fibre orientation characterisation method by scanning electron microscope (SEM) image analysis for low $V_f$ injection moulded fibre reinforced polymers. This study tries to overcome the tedious and time-consuming practice of having to determine 3D fibre orientations with successive grinding and polishing by analysing a single SEM image taken under a 45° oblique plane and applying the shadow method analysis (see paragraph 3.1). The 3D fibre orientations are reported in the form of orientation- tensors components by probability distribution functions. Sharma et al. [38] measures the fibre orientation in long carbon fibre injection moulded reinforced composites and reports on them by analysing the change of orientation tensor components through-thickness of the sample. They also discuss the biases which can be introduced during sample preparation and image processing including ellipse fitting with the MoE methodology.

Studies on microstructural characterisation of high-performance realigned CF tapes and fabrics are harder to come by when compared to injection moulded composites. Research projects which process and re-align short and long discontinuous fibres into high-performance rCF materials, mostly report on mechanical properties as an indication of microstructural quality. Most of these research projects are industrially orientated explaining this emphasis. When they report on microstructural characteristics, they refer to $V_f$, voids and average fibre orientation of a limited number of fibres studied.

Examples of these research projects are; The HiPerDiF project Yu et al. [39] which reports on fibre orientations determined by measuring embedded and polished specimens by microscopy. The fibre orientation was manually determined from in-plane samples by drawing lines in CAD on a total of 400 fibres across five microscopy images. The resulting line angles were analysed by probability distribution function to conclude that both 65 % of the fibres for the 41 % $V_f$ sample and 67 % of the fibres for the 55 % $V_f$ sample were in a range of ±3°. It was subsequently noted that the fibre orientation in the processed and cured samples was “slightly” worse than the dry

preforms. A fibre length of 3mm is used by the HiPerDiF method, being that the estimated critical fibre length was 0.45mm by assuming an interfacial shear strength (IFSS) of 34MPa. The material with 55 % $V_f$ achieved a tensile modulus of 115 GPa and tensile strength of 1509 MPa.

The TUFF project [20], [40], [41] papers characterize their microstructure in terms of areal weight, $V_f$ , distributions of fibre length, fibre to fibre spacing and fibre alignment by using microscopy and µCT analysis. The project claims to have achieved full property translation of stiffness and strength when compared to continuous prepreg. They characterised their material to have a 60 % $V_f$, 95 % of all their fibres aligned within 5° and a minimum fibre aspect ratio of 600 (≈3 mm fibre length with ±5 µm fibre diameter). Two sets of cross-sectional micrograph samples were studied. One set was cut perpendicular (90°) to fibre direction and analysed with edge detection and Hough transformation algorithm to locate fibre centres and measure fibre diameter. These samples were used to calculate areal weight, Vf and fibre spacing. Fibre spacing analysis yielded that 80 % of the first four neighbours were located within 0.3, 0.5, 1.5, 3µm and 0.6, 0.9, 1.5, 3 µm for the two different sample materials. The second set was cut at 15° from the fibre direction and was used to measure fibre alignment with ellipse fitting and then applying the MoE. The microscopic approach evaluated only 400 fibres per sample. An interesting result was that the smaller fibre lengths tended to increase alignment quality. Similar characterisation was done by Werken et al. [42] and Xiao et al. [33] which analysed the FOD and fibre spacing by in-plane microscopy and µCT of re-aligned material. An overview of different re-alignment projects and their associated mechanical properties are shown in Figure 25.

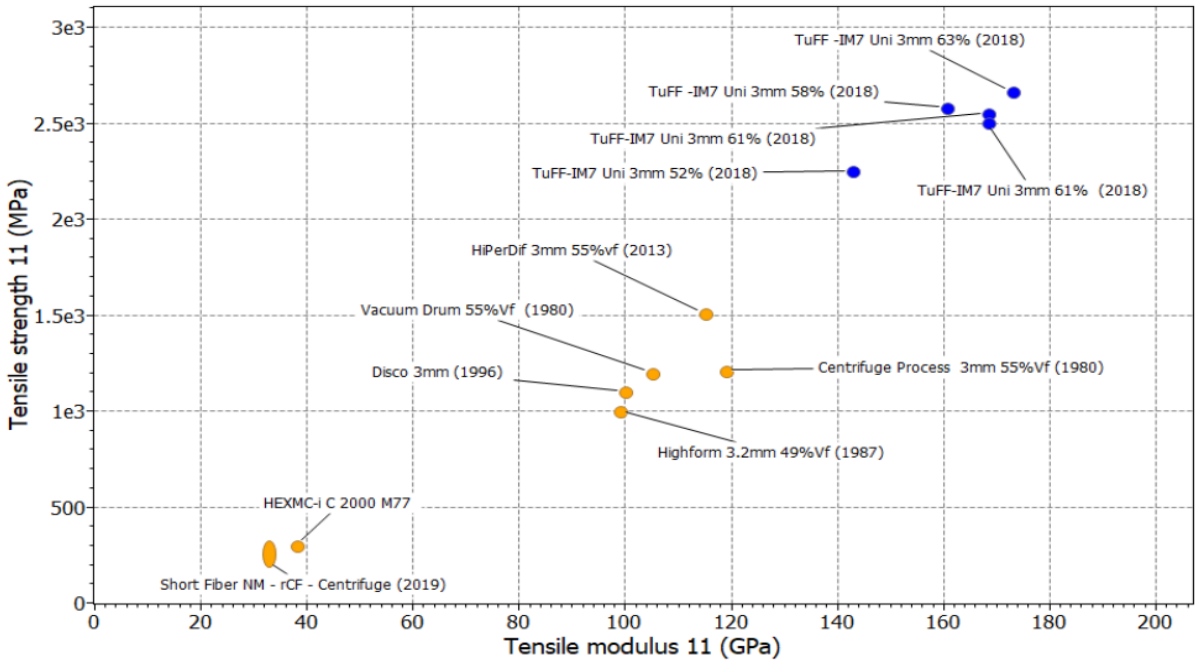


*Figure 25 Comparison of mechanical performance of realigned discontinuous CF composites [Yarlagadda et al. 2019]*

## 2.5 Knowledge gaps

Studies that report on discontinuous CF composites by optical microscopy and µCT are abundant. These studies span a wide field of interest, varying from fibre and void content, ply stacking, fracture mechanics and global fibre orientations. Studies that report on the individual 3D discontinuous fibre morphologies are respectively rarer. This can be explained by the fact that characterising 3D fibre morphology by optical microscopy is labour intensive and time-consuming. Studies that apply the µCT method for 3D fibre morphology characterisation are becoming more common. In the past laboratory-scale µCT devices were hindered by cost, insufficient resolution, and contrast, but in more recent years the laboratory scale µCT devices have become more capable and research on the 3D fibre morphology in one scan has therefore begone to be more feasible.

Research that reports on microstructure and the individual fibre morphology of recycled discontinuous CF composites can be split into two groups. The first characterises low $V_f$ and more diffusely FOD injection moulded CFRP composites. The second investigates more high performance re-aligned materials that feature high levels $V_f$ and a narrow band of FOD. This last group of studies is of particular interest for this thesis. Literature from this second group has shown that identifying fibres and analysing the microstructure on multiple parameters by either optical microscopy or µCT is not novel but remains a challenging matter. The relevant articles apply their characterisation method on a small selection of fibres in cross-sections or in-plane images and extrapolate their findings to quantify the quality of their produced material. These articles all have an industrial or commercial interest behind their publications and are thus incentivised to only show their best results and do not show the variation in microstructure across different processing parameters.

This is an evident knowledge gap that ought to be filled to help the advancement of rCF to achieve mechanical properties of vCF. As explained in paragraph 1.2 the research goal for this thesis project is to introduce an initial quantitative characterisation method that can be applied to rCF. Subsequently being further developed and functioning as a framework for improving the material quality by comparing the resulting microstructure with changing manufacturing parameters.

# 3. Method of microstructural characterisation

The purpose of this chapter is to explain the theoretical methodology of microstructural characterisation of discontinuous CFRP. First, the methodology behind determining the fibre orientation by the Method of Ellipses (MoE) is explained in paragraph 3.1, after which the methodology behind morphology characterisation is given in paragraph 3.2. The sequencing of these paragraphs is done since the latter uses the parameters which result from the MoE as explained in paragraph 3.1. Material parameters which determine the mechanical properties of discontinuous CFRP have been introduced in Paragraph 2.1 and will not be further explained in this chapter. Relevant literature which reports on the characterisation of discontinuous CFRP is reported in paragraph 2.4.

## 3.1 Method of Ellipses

Over a short distance, CFs can be assumed to be cylindrical, rigid, straight rods. Therefore, its spatial orientation within the composite can be described using spherical coordinates with the azimuthal, or in-plane ($\phi$), and the zenith, or out-of-plane ($\theta$) angles as is shown in Figure 26.

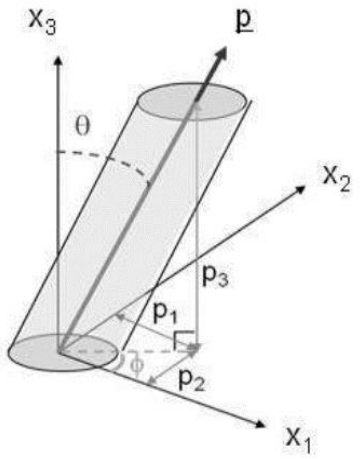


*Figure 26 Orientation components for a single fibre description [Vélez-Garcia et al. 2010]*

The CFs leave elliptical footprints on the surface plane after being ground and polished for the reflective light OM, as can be seen in Figure 27A. The resulting ellipse yields five geometrical parameters which can be used to characterize the fibre orientation by constructing an orientation vector. This method is known as the Method of Ellipses (MoE) [43].

The five parameters as visualised in Figure 27b are the x and y location of the fibre mass centre ($x_c$, $y_c$), the minor ($m$) and major ($M$) axes, and the in-plane fibre angle ($\phi_f$) defined with respect to the $x_1$-axis of the observational plane and major-axis.

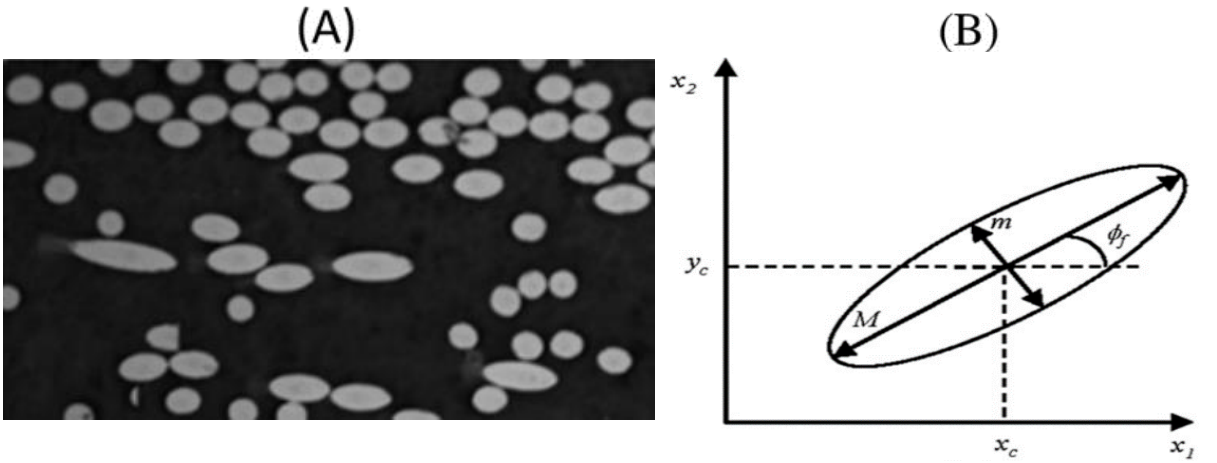


*Figure 27 (A) Optical microscope image showing elliptical footprints of fibre cross-sections in a composite [Vélez-García et al. 2012] (B) Definition of five geometrical xc, yc, m, M, and ϕf parameters measured in each ellipse to extract these [Vélez-García et al. 2010]*

To translate the elliptical cross-section to a shape measurement, a best fitting ellipse must be constructed. In this thesis, the principle of "ellipse of concentration", or otherwise called the "method of moments" is used. [44] Other methods available include least square regression and least sum of squares fitting procedures. [45]
The method of moments calculates the first and second-order central moment of fibre pixel data points. The first order central moment represents the mean value of all coordinate data, thus the x-y mass centre. The second characterises the variance or shape distribution of pixel data points with the minor and major axes. These descriptors can be used to construct an ellipse in standard form:

$$\frac{x^2}{a^2} + \frac{y^2}{b^2} = 1 \tag{1}$$

Where x - y are the centre coordinates, and a - b are the minor - major radii. This approach ultimately relates the shape of all fibre pixels to the area and fitment of the ellipse to the original fibre cross-section. Obtaining the fibre pixels is further explained in paragraph 4.3.1. The best-fitting ellipse is defined by the highest effective percentage covering the fibre pixels. This fitment factor f is defined by:

$$f = \frac{\pi ab - n}{n} \tag{2}$$

Where πab is the area of the fitted ellipse and n is the measured pixel area.

After the best fitting ellipse is defined for every fibre, the OoP angle can be calculated by:

$$\theta = cos^{-1}\left(\frac{m}{M}\right) \tag{3}$$

Unfortunately, a fundamental weakness of this MoE is its inability to give a complete and definite verdict about the orientation of the fibre from one single 2D micrograph

image. The problem is that any measured ellipse can represent two possible OoP fibre orientations, as depicted in Figure 28. Both tilted fibres have the same in-plane angle $\phi$, but the OoP $\theta$ angle is ambiguous. Because the 2D ellipse cannot define if the real fibre angle $\theta$ is positive ($\theta + \pi$) or negative ($\theta - \pi$) relative to the out of plane axis $x_3$ from Figure 26 on page 23.

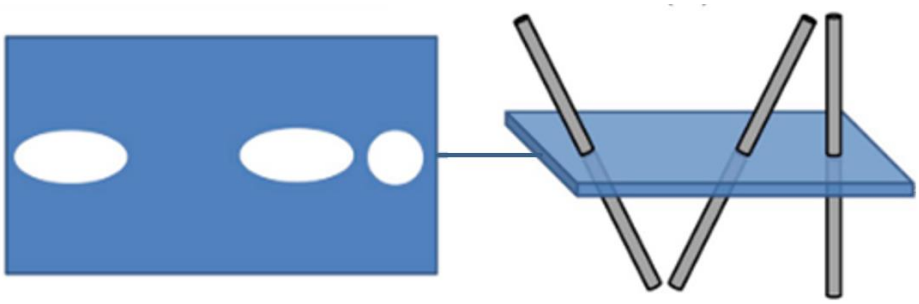

*Figure 28 Ambiguity in fibre orientation, the two fibres under an angle of θ and -θ have identical elliptical footprints on the surface plane. [ Hanhan et al. 2019]*

To determine the sign of $\theta$, a second measurement is needed to verify the OoP angle for characterising the fibre morphology. One of these methods is done by grinding and polishing down a small known distance h. After which, another OM image is taken and compared with the original image to measure in which direction the ellipse has moved, specifying its true 3D orientation, as can be seen in Figure 29.

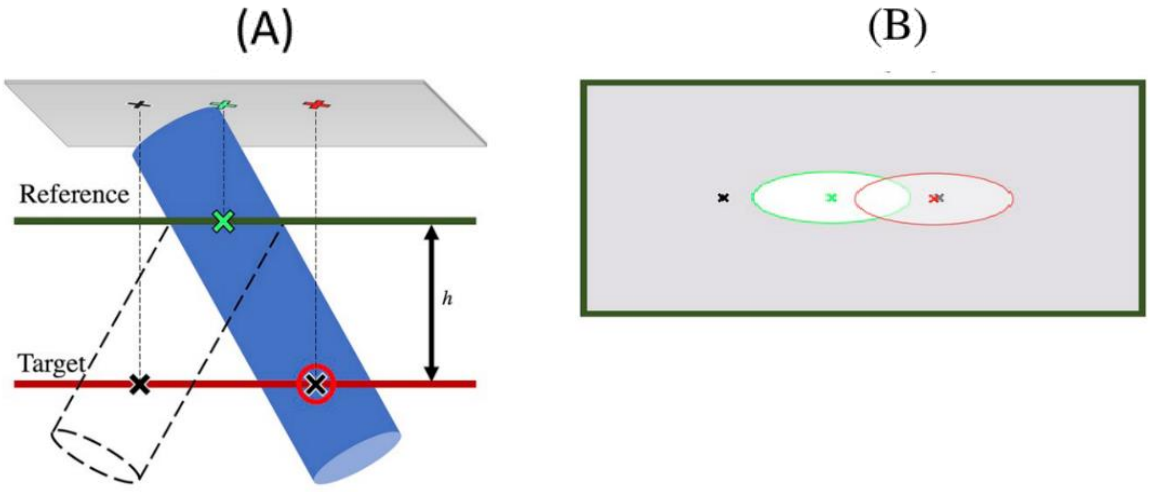


*Figure 29 Verification OoP orientation (A) Geometrical representation of ambiguous fibre direction and its two possible positions before second measurement. (B) Change of ellipse position as effect of second measurement, verifying sign OoP angle [ Hanhan et al. 2019]*

Alternatives to this successive parallel grinding and polishing method is to grind two orthogonal plane sections or two inclined cross-sections. [46] Another way of verifying the sign of $\theta$ and thus true 3D fibre orientation in the MoE is to measure the so-called shadows left by the fibre. This shadow indicates the underlying fibre which can be measured after a consecutive etching procedure [35], [47] or by using a scanning electron microscope (SEM) [35], [37], [48] when acquiring the original images. The

SEM can detect features just underneath the surface because of high energy backscattering electrons used for imaging. Results for both etchant and SEM shadow methods can be seen in Figure 30. The downside to this technique is that the microscopy sample is destroyed after only two measurements, excluding consecutive measurements to characterise fibre mobility through sample height.

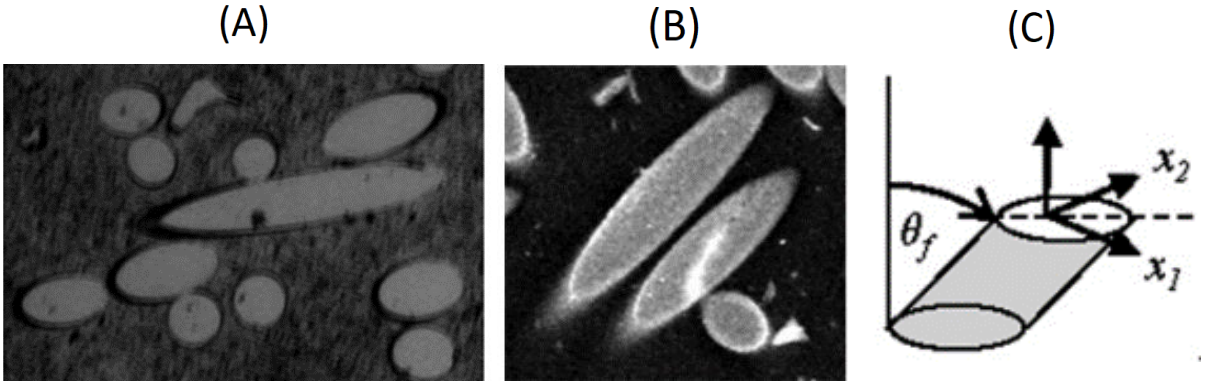


*Figure 30 (A) OM image showing shadows after etching [Vélez-García et al. 2012] (B) SEM image showing fibre shadow as effect of the penetration energy of the high energy electrons used for imaging [Régnier et al. 2008] (C) geometrical representation of the shadows [bay et al. 1992]*

After identifying the correct sign of θ, an unambiguous orientation tensor A can be constructed to characterise the complete 3D fibre direction by the second-order tensor form A, which is structured as follows:

$$A = \begin{bmatrix} A_{11} & A_{12} & A_{13} \\ A_{21} & A_{22} & A_{23} \\ A_{31} & A_{32} & A_{33} \end{bmatrix}$$

With the suffixes for the tensor terms being associated with:

1. The primary fibre/tape direction
2. Transverse to the primary fibre/tape direction (width of the material).
3. The thickness direction.

The components for this tensor A can be determined by the $\vec{p}$ unit vector as given by:

$$p_1 = \sin(\theta)\cos(\phi) \quad (4)$$
$$p_2 = \sin(\theta)\sin(\phi) \quad (5)$$
$$p_3 = \cos(\theta) \quad (6)$$

and A can then be defined as:

$$A_{ij} = p_i p_j = \begin{bmatrix} sin^2(\theta)\,cos^2(\phi) & sin^2(\theta)\,cos(\phi)\,sin(\phi) & sin(\theta)\,cos(\theta)\,cos(\phi) \\ sin^2(\theta)\,cos(\phi)\,sin(\phi) & sin^2(\theta)\,sin^2(\phi) & sin(\theta)\,cos(\theta)\,sin(\phi) \\ sin(\theta)\,cos(\theta)\,cos(\phi) & sin(\theta)\,cos(\theta)\,sin(\phi) & cos^2(\theta) \end{bmatrix}$$

Where the OoP angle is specified as -90° ≤ θ ≥ 90° and the in-plane angle -90° ≤ ϕ ≥ 90°. The original nine components reduce to five independent ones, due to tensor symmetry $A_{ij}=A_{ji}$ and normalization condition $A_{11} + A_{22} + A_{33} = 1$.

The 2D ellipses from the MoE define $A_{11}$, $A_{22}$, $A_{33}$, and $A_{12}$, but since sin(θ) ≠ sin(-θ) the components $A_{13}$ and $A_{23}$ are undetermined without the secondary measurement since each contains a single sin(θ) term.

For the fibre angle microstructure characterisation, the three most useful descriptive orientation components are:

- $A_{11}$ Orientation in the main fibre direction, varying from 0 to 1.0.
- $A_{22}$ Orientation in-plane transverse to the main fibre direction, varying from 0 to 1.0.
- $A_{13}$ Orientation tilt of main direction fibres in out of thickness plane, varying from -0.5 to 0.5.

Where values closer to zero for the three entries; $A_{11}$, $A_{22}$, $A_{13}$ mean a higher degree of unidirectional fibre angle.

Comparing the global and local average values for these three entries and the OoP orientation θ in a FOD or histogram describes the microstructural quality of the sample material.

It must be noted that the probability of detecting a fibre in the microscopy plane decreases when the misalignment of the fibre increases. The probability of detection is further decreased when fibre length is reduced, as is the case for discontinuous fibres, leading to undercounting of fibres. To correct for this undercounting bias, a weighting function is often applied to every measured fibre k, and is as follows:

$$F(\theta_k) = \frac{1}{\mathrm{L}\cos\theta_k + \mathrm{d}\sin|\theta_k|} \tag{7}$$

The function depends on the fibre length L, and fibre diameter d, or in alternative notations fibre aspect ratio q. For highly aligned long discontinuous fibres the weighted factor is often ignored when analysing the complete cross-section. By measuring the complete cross-section the probability of miscounting a high angular fibre is significantly reduced as a function of the total probability. [35], [37], [38], [48]

## 3.2 Fibre morphology

The ideal discontinuous microstructure can be described as unidirectional straight parallel fibres with close uniform spacing, as depicted in Figure 31. Any deviation from this ideal microstructure will decrease the mechanical properties of the material. To grade and compare the microstructural quality of rCF materials with the ideal microstructure, a quantitative characterisation method must be applied. The MoE as explained in paragraph 3.1 yields a total of six parameters unique to every fibre. Besides the in- and OoP angles, the x-y coordinates and minor-major axes can additionally be used to further evaluate the microstructure.

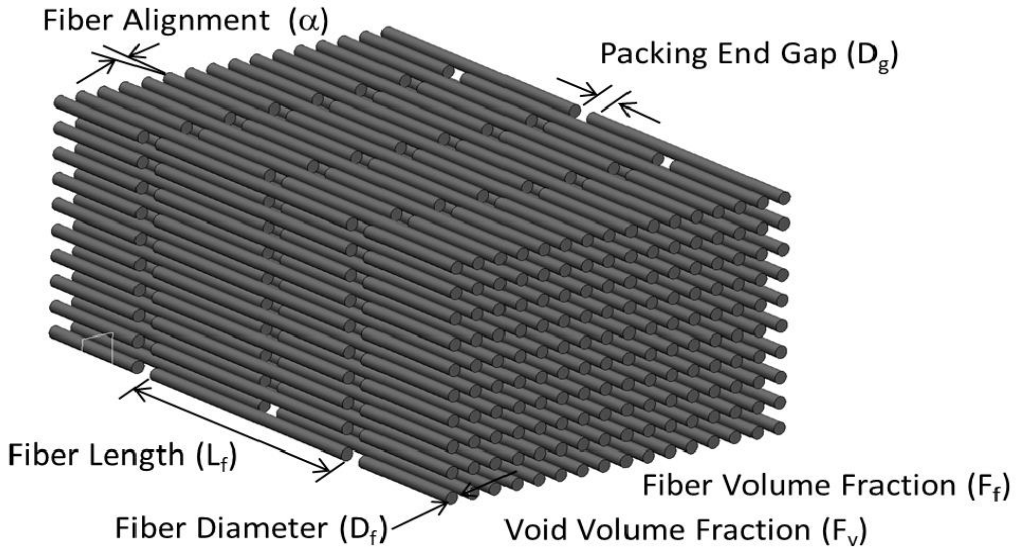


*Figure 31 schematic representation of ideal microstructural including topics of interest for characterisation [Heider et al. 2019]*

With these four parameters, multiple quantitative microstructural descriptors can be defined which express fibre packing efficiency. These include among others: fibre-to-fibre (FTF) spacing and $V_f$. Besides these, the average fibre diameter can be evaluated by measuring all the minor axes and comparing it to the fibre diameter as specified by the vCF manufacturer. Although the fibre length distribution is not measured in this study, these values are known by the CF recycling company and research institute which can be of importance in later research when variations in aspect ratios are discussed to translate mechanical properties.

Both FTF spacing and $V_f$ can be measured on a global or local scale. The global values allow materials to be compared with each other on a material datasheet macro-level. For microstructural analysis, the local descriptors are of greater importance for evaluating the effect of processing on material quality. When $V_f$ is analysed on a local level across the complete cross-section, it essentially becomes a descriptor of Fibre Density Distribution (FDD). This FDD describes the change of fibre density or $V_f$ across the sample. This thesis uses local $V_f$ as a descriptor for finite values, and FDD when referring to graphs or figures which express the local $V_f$ over an area, or along a distance.

FTF spacing describes the fibre arrangement concerning its nearest neighbours. This microstructural feature is highly susceptible to imperfections which decrease efficiency as explained in paragraph 2.1. The ideal spatial distribution can be described as hexagonal packing which has a well-defined distance to its neighbours, as can be seen in Figure 32A. This perfect hexagonal packing can be achieved on a localised scale, as can be seen in Figure 32B, but since this microstructure is meta-stable, it is unobtainable in real life for the complete cross-section. When the FTF spacing is calculated for all fibres in the cross-section and plotted in a cumulative probability function, a quantitative characterisation can be made from the distribution in assessing the effectiveness of fibre packing.

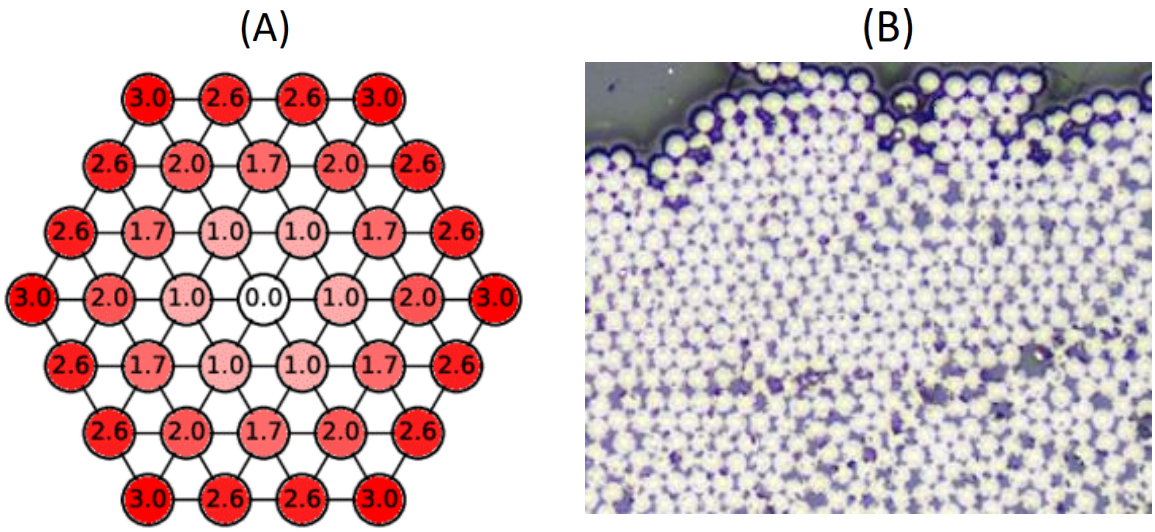


*Figure 32 (A) Distance to nearest neighbours expressed in fibre diameter on a square and triangular lattice [Mikael Fremling], (B) microscopy cross-section of compression test sample P at 20x magnification showing hexagon packing at high compression.*

# 4. Experimental

This chapter explains which specific rCF materials were researched, how samples were created and how these were analysed to quantitively characterise the microstructure. Paragraph 4.1 expends on the four distinct material sets which were researched and how they were processed into samples. Paragraph 4.2 covers issues encountered during image acquisition for microscopy analysis and their solutions for optimising image quality. Paragraph 4.3 explains the image processing used to analyse the microstructure.

## 4.1 Materials and sample preparation

To examine the effects of processing parameters used during the manufacturing process of rCF, four material sets with varying processing parameters were studied. The specific processing parameter are subject to Intellectual property (IP) of the collaborating companies and will therefore not be disclosed during the thesis.. In the table below an overview is given of the sample nomenclature and their specifics. Sample sets 1-2-4 were post-processed in the aerospace department at TUDelft with a varying number of layers and compaction to reveal effects on microstructure and analysis. Sample set 3 was surplus material processed by CF recycling company and functioned in this thesis as a test to see if the characterisation method could handle materials with high amounts of $V_f$.

| Processing parameters | Sample name | Quantity of samples | Layers of tape | Compaction |
|---|---|---|---|---|
| 1 | A1 – A5 | 5 | 1 | Vacuum |
| | B1 – B5 | 5 | 1 | Vacuum |
| | C1 – C5 | 5 | 2 | Vacuum |
| | D1 –D5 | 5 | 5 | Vacuum |
| 2 | L1 – L1-5 | 5 | 1 | Vacuum |
| | L5 – L5-5 | 5 | 5 | Vacuum |
| 3 | P1 – P2 | 2 | 28 | >80 Bar |
| 4 | S1 – S4 | 4 | 1 | Atmosphere |

### 4.1.1 Resin Impregnation and compaction of tape material

Sample sets 1-2-3 were impregnated with resin and then compacted under vacuum. Tests were done to see which process yielded the best results for microscopy analysis. Both resin infusion and wet layup (with vacuum bag) were tried. The resin infusion process yielded poor results, among others because of voids still present in the tape. The wet layup process gave far better results. For this reason, wet layup was chosen as production technique throughout the thesis project. Because the texture of the dry tapes tended to retain small air bubbles after wetting, a low viscosity (infusion) resin was chosen. The resin used during the wet layup procedures was the Epikote and Epicure 04908 resin system by Hexion, which has a low exothermic 24-hour cure time.

After mixing, the resin was degassed, the dry tape was submerged in resin and both were degassed again. The wetted tape samples were gently draped on a section of vacuum bagging film. When samples were made with multiple layers, each layer was draped on top of each other piece by piece. Afterwards, the vacuum bagging film was folded onto the wetted tape in a lengthwise direction in a draping manner. To ensure a minimum amount of air was trapped in the tape after the bagging film envelope was folded, the surplus resin was removed out between the envelope by using a squeegee to push the excess resin and trapped air out. Excess vacuum bagging film was cut from the envelope at a margin from the tape edges. The samples were placed on an aluminium base plate, covered with peel-ply, breather, and vacuum bag after which the samples were cured under vacuum for 12 hours at ambient temperature. When samples were made with multiple layers, a caul plate was placed on top of the envelope between the layer of peel-ply and bleeder, as can be seen in Figure 33. The addition of the caul plate was found to be of help with compressing the multiple layers into a more densely packed sample with two straight sides.

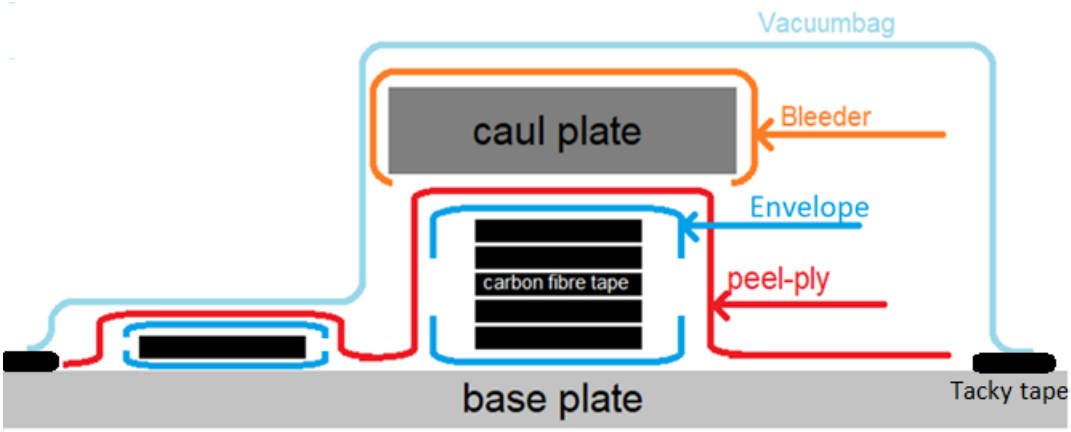


*Figure 33 Visualisation of wet layup curing under vacuum setup with 1 layer and 5-layer samples*

### 4.1.2 Embedding, grinding and polishing

For microscopy imaging, the dry and cured tape samples had to be fixated in a vertical position and polished to clearly show the fibre cross-sections. The procedure for dry uncompressed and cured compressed tape samples varied. The dry uncompressed samples were clamped in a brass spring sample holder, as can be seen in Figure 34A. Unconventional to normal embedding of microscopy samples, the opposing side of the tape not clamped by the sample holder would be the microscopy cross-section and thus uncompacted. Care was taken to position this side parallel the bottom of the embedding cup when still dry. The cured and compressed tape samples were cut by angle disk into 2cm pieces, then clamped in a five-piece sample holder, as can be seen in Figure 35A and placed in embedding cups likewise to Figure 34B. Both samples were then embedded in Struers EpoFix, a room temperature curing epoxy resin. The EpoFix resin was mixed and degassed before carefully pouring the resin into the sample cup with a Citovac vacuum impregnation unit. It was found that when the resin wasn't degassed before pouring, resin with too much-expanding air was introduced

into the sample cups, causing the clamped sample to float introducing a bias angle in sample orientation. Any remaining air was removed from the sample with the CitoVac unit by holding the submerged samples at the highest machine vacuum setting (0.9 mBar) for 45 min, after which vacuum was removed and samples were left to cure at ambient pressure for 12 hours.

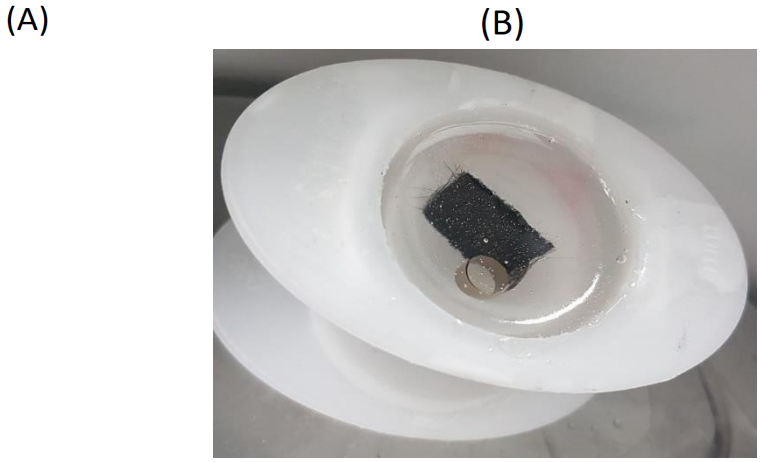


*Figure 34 (A) uncompressed sample material set 4 in dry state, (B) during atmospheric*.

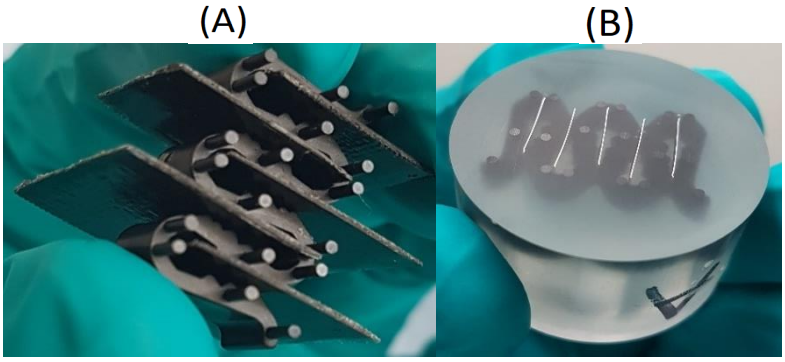


*Figure 35 (A) Pre-embedding clamped samples. (B) Sample cross-section after grinding.*

The cured embedded samples were ground and polished with a Tegramin 20 automatic grinding and polishing machine. Best surface finish results were achieved with the procedure as given in Table 1.

*Table 1 Grinding and polishing procedure*

| # | surface | Lubricant | Time [sec] | Rotation speed floor [rpm] | Rotation speed head [rpm] | Rotation direction of head with floor | Pressure [N] |
|---|---|---|---|---|---|---|---|
| 1 | SiC #500 | Water | 30 | 300 | 150 | Co-rotation | 40 |
| 2 | SiC #1000 | Water | 30 | 300 | 150 | Co-rotation | 40 |
| 3 | SiC #2000 | Water | 30 | 300 | 150 | Co-rotation | 30 |
| 4 | SiC #4000 | Water | 40 | 300 | 150 | Counter-rotation | 15 |
| 5 | Chem Polish | OP-S nondry | 180 | 150 | 150 | Counter-rotation | 15 |
| 6 | Chem Polish | Water | 60 | 150 | 150 | Counter-rotation | 15 |

## 4.2 Optimising image acquisition and stitching

Microscopy images were taken at the TUDelft aerospace faculty on a Keyence 3D laser scanning VK-X1000. This microscope has an automated stitching procedure, which generates one large image from multiple smaller ones, making it possible to image the full material cross-section at high magnification. Multiple magnifications were tried to assess which machine setting produced the best possible image with the least amount of scan time. The cross-sectioned material micrographs which gave the best detail on individual fibres were performed at the highest available magnification of 50x. The downside was that this magnification level took multiple hours to image the complete cross-section. Scans that were performed at 20x took 30-45 minutes and gave sufficient information about the position of the individual fibres but not their shape. Therefore, 50x was used in subsequent analysis to measure fibre shape and position.

Problems were encountered with image quality when images were stitched with the Keyence Stitching Module VK-H2J. This build-in software package can handle roughly 25 million pixels of stitched image build volume. When build resolutions were higher than these 25 million pixels, the image quality was automatically decreased. Image series acquired of the material studied in this thesis at 50x and 20x often exceeded this limit significantly, leading to disappointing image resolutions. Besides total pixel limitations, the automatic overlap alignment for the stitching procedure was often lacking in precision, causing diffuse areas where the images overlapped, as can be seen in Figure 36a. To retain the original micrograph image resolution and get better stitching performance, the raw image data was extracted by python script and stitched with the Grid/Collection Stitching module in ImageJ. The python script for extracting raw image data from Keyence VK4 files can be found in appendix A&B. The improved image quality by this new approach can be seen in Figure 36b.

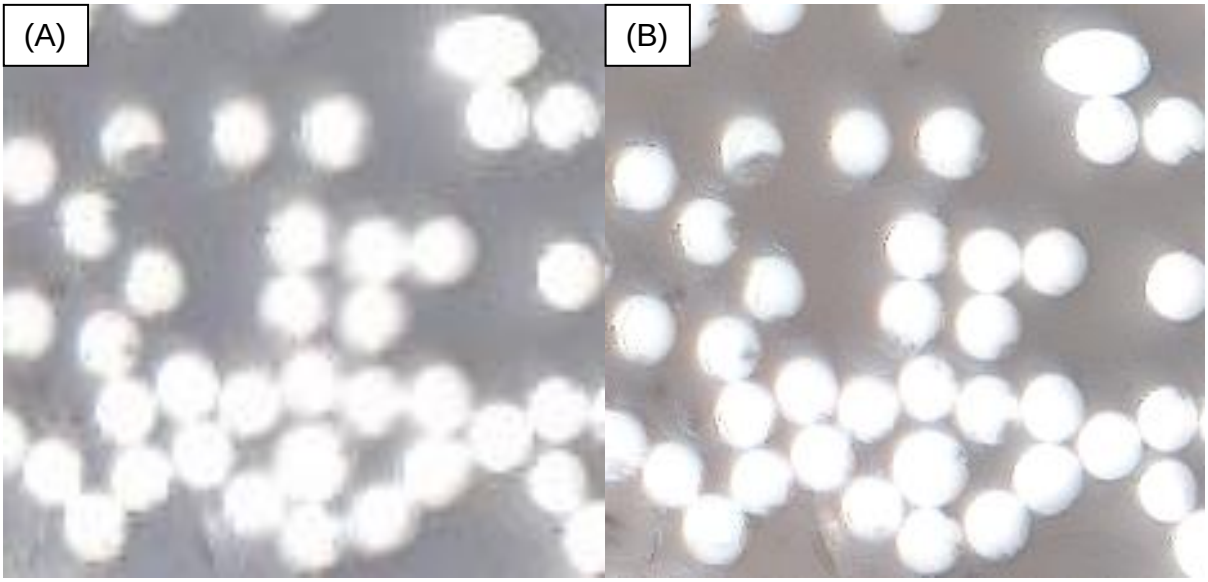


*Figure 36 Comparison image quality between (A) Keyence stitching module, (B) Python stitching method.*

## 4.3 Image processing

The image processing pipeline as visualised in Figure 37 consists out of five steps after which the resulting data can be analysed for microstructural characterisation. Steps one and two are covered in paragraph 4.3.1. Steps three and four are explained in paragraph 4.3.2. The implementation of step 5 and the application of data from this analysis pipeline on the characterisation of fibre morphology is explained in paragraph 4.3.3. Steps 3 to 5 have been translated into a FIJI ImageJ macro which can be found in Appendix D & E. The python code used to analyse all image data can be found in Appendix F

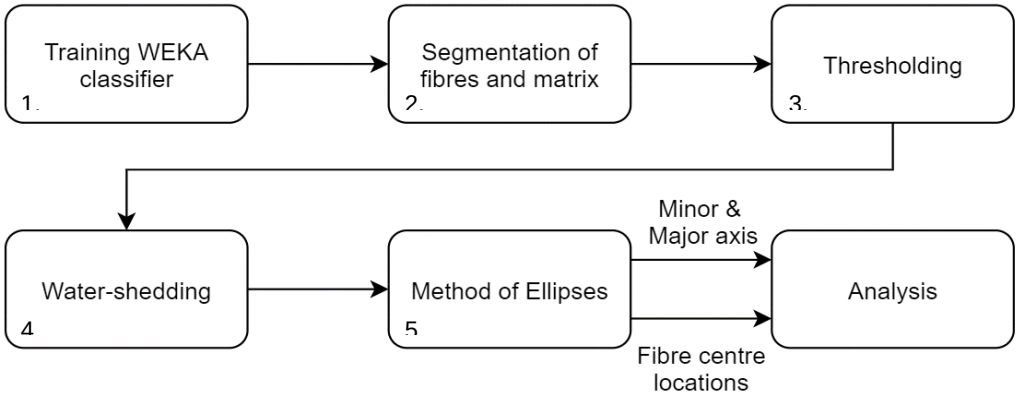


*Figure 37 Image processing pipeline*

### 4.3.1 WEKA Segmentation

The number of fibres within the material cross-section can range from a few thousand to fifty thousand depending on the material set and tape layers. All these fibres must be identified and segmented from the matrix to allow for microstructural analysis. The identification and segmentation are done with the open-source Waikato Environment for Knowledge Analysis (WEKA) semi-supervised machine learning tool in FIJI ImageJ.[49]

This WEKA segmentation tool allows the “supervisor” to select and classify a small selection of features and areas in the microscopy image. These selected regions are then used by the machine learning process to classify and segment the cross-section on a pixel-intensity value, as can be seen in Figure 38.

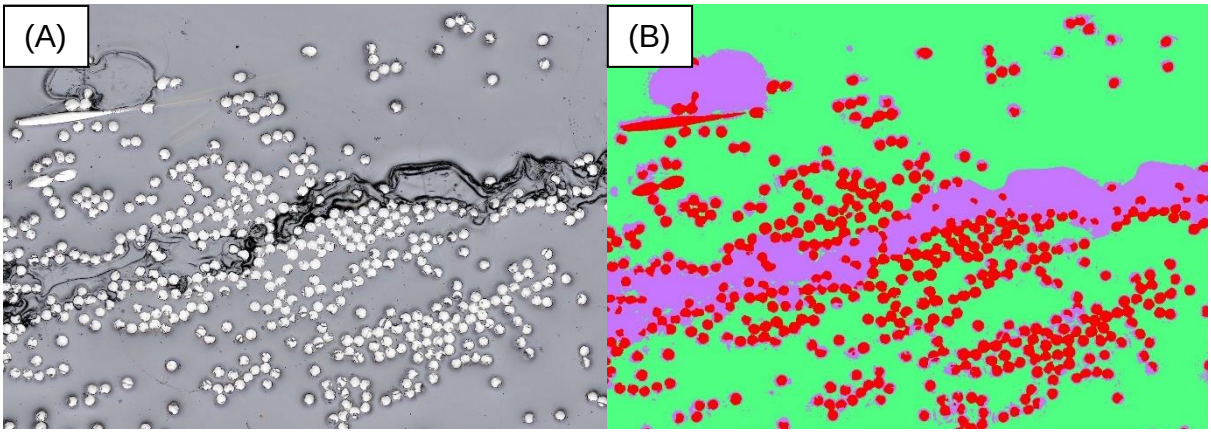


*Figure 38 (A) original image, (B) classified image which features classified phases*

Selection and assigning a class are done by hand using the drawing tools available in Fiji ImageJ and adding them to predefined classes. After features of interest are selected and assigned to a class, the WEKA segmentation tool can be applied to the microscopy image. The initial segmentation result can vary in accuracy depending on micrograph quality, number of selected features, and precision of the feature selection. To improve segmentation accuracy, the WEKA tool can be trained by selecting incorrectly classified areas and classifying them as the correct phase, after which the classifier can be run again to create a new classified image. This training procedure can be repeated till the user is satisfied with the segmentation quality of the image, as can be seen in Figure 39.

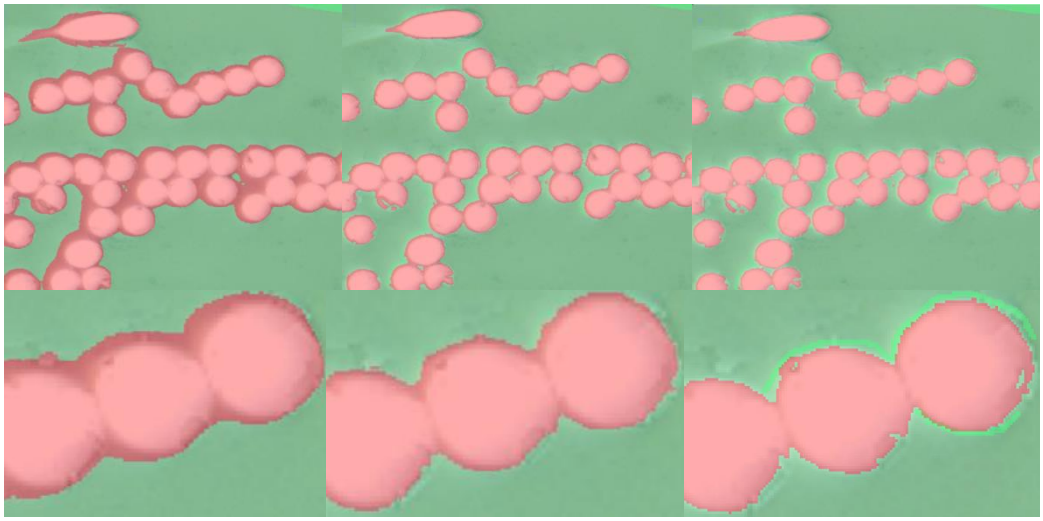

*Figure 39 Overview of classifier training steps and their effect on segmentation quality*

During initial segmentation and further training of the classifier, a small section (±2000 x 2000 pixels) of the parent image was used instead of the complete cross-section to reduce computing power and required memory. After the results from the trained classifier were satisfying on the smaller image, the classifier was applied to the complete cross-section. The segmentation of full microscopy cross-sections with a trained classifier frequently led to out-of-memory errors. To reduce the amount of RAM memory necessary for segmentation of a complete cross-section, a tiling sequence in FIJI ImageJ was applied to process segments of the cross-section one at a time. This tiling sequence macro code can be found in appendix C.

During this thesis research project, several classifiers were trained for multiple material sets and samples. The reason for needing to train multiple classifiers and not just one for applying to all samples was caused by the micrograph images having different pixel intensity values for fibres and matrix. This is caused by image contrast varying between-samples, because of the difference in reflectiveness between sample. The fibres within the polished samples are highly reflective, thus samples which have higher $V_{f,}$ or which contain more fibres are more reflective, resulting in different pixel intensity values for fibres and matrix.

The Keyence VK-X1000 microscope used during this study automatically sets the light intensity and exposure time for every image it takes during the stitching procedure, even when the raw images are extracted and stitched with the improved method as explained in paragraph 4.2 the contrast differs greatly between samples, as can be seen in Figure 40.

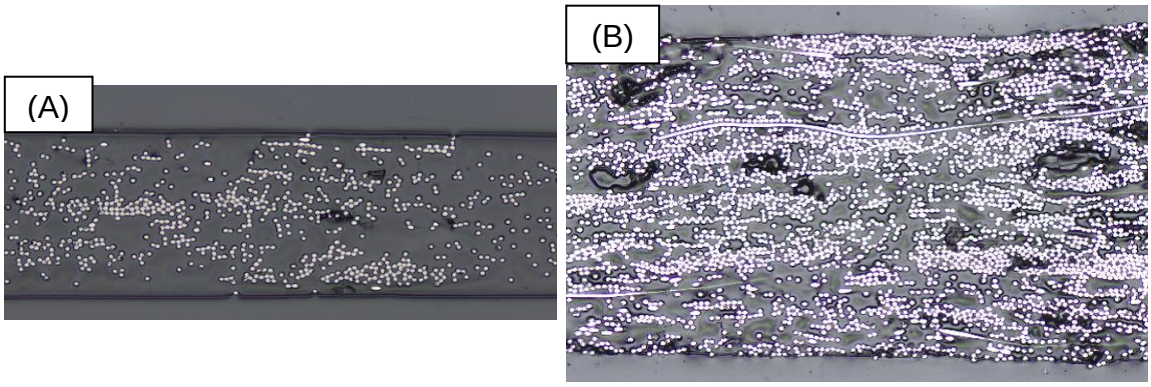


*Figure 40 Comparison between contrast in sample set 2 for samples (A) L1 x20 1 and (B) L5 x20 3*

After the trained WEKA segmentation tool is applied, an 8-bit probability map is generated specifying on a scale of 0 till 255 what the probability is of a pixel being either fibre or matrix, as can be seen in Figure 41. The quality of segmentation by the WEKA tool can be assets by the gradient of change between matrix-fibre, and fibre-fibre. A steeper change on the boundary between phases indicates a higher degree of certainty at identification. The distinction between matrix and fibres is a relatively easy one for the WEKA segmentation tool because of the large difference in contrast and thus pixel intensity in the original image. The boundary between touching fibres is a more difficult one, as can be seen in the inserts of Figure 41. This problem will continue to grow when fibre compaction increases and areas of only touching fibres are present. Increasing image resolution, contrast and visibility of fibre boundaries in the original micrograph will decrease this problem. However, touching fibres will remain difficult to separate based on probability mapping. Solutions to this problem are explained in the next paragraph.

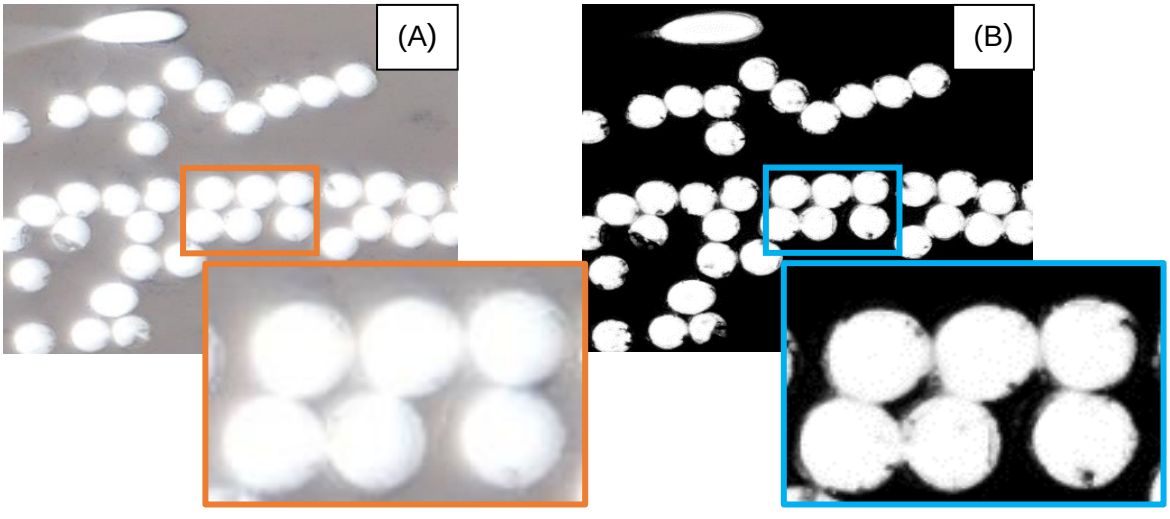


*Figure 41 Result from segmentation (A) origional microscopy image C1 50X (B) Probability map C1 50X*

### 4.3.2 Thresholding and water-shedding

The probability map as produced by the WEKA segmentation tool must be further processed to be used for microstructure analyses. The probability map doesn't definitively tell which pixels are fibres but gives a probability ranging from 0 to 255 in pixel grey value intensity for an 8-bit image.

To get a definite answer, a threshold must be defined between 0 and 255 which excepts or declines the possibility of a pixel to be a fibre. This thresholding procedure yields a binary image where the pixel intensity is either 0 or 1. For all probability maps analysed in this thesis, an Otsu thresholding method has been applied in FIJI ImageJ.[50] This Otsu method sets the limit by finding the point of maximum variance in pixel intensity between the fibre and matrix. The difference in probability or gradient between fibre and matrix is significantly dissimilar when a well-trained WEKA segmentation tool is applied, resulting in the Otsu threshold limit being in the middle of the probability range (±127) indicating the maximum amount of variance between the two phases.

After applying the Otsu threshold, close-packed and touching fibres are often fused as can be seen in Figure 42A. This is caused by pixel intensity at the boundary between touching fibres being higher than the Otsu threshold.

Manually setting a stricter threshold will decrease this conglomeration of fibres. However, setting a stricter threshold that separates the boundary between touching fibres also affects the fibre shape to the point where the original fibre shape is no longer recognizable. This technique can be used when the identification of fibre centres in highly compacted materials or micrographs with low contrast are is needed.

To separate the conglomerated fibres a distance transform watershed [51] procedure is applied in FIJI ImageJ. This procedure transforms the binary image with the conglomerated fibres to a distance map which expresses the distance from mass centres to borders, as can be seen in Figure 42B. The water-shedding step separates the fibres at the furthest distance between centres, as can be seen in Figure 42C. The downside to this procedure is that fibres now feature straight lines at the former border, distorting fibre shape. Luckily, this distortion does not impact the fitment of the ellipses noticeably, as explained in paragraph 3.1 and demonstrated in paragraph 5.1.

(A) (B) (C)

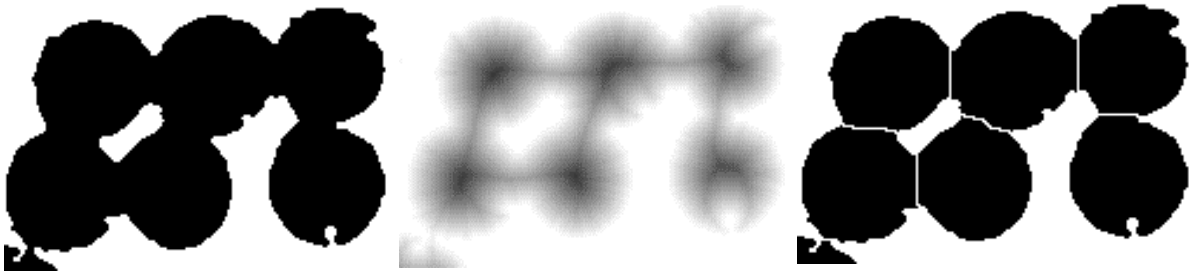

*Figure 42 Result from (A) Otsu Thresholding, (B) distance transform and (C) watershedding C1 x50*

### 4.3.3 Method of ellipses and image analysis

The MoE is applied in FIJI ImageJ employing the “analyse particles” tool, The FIJI ImageJ macro code to run this procedure automatically can be found in appendix D. First, centroid and fit ellipse are selected in the “set measurement” dialogue box for the analysing tool to measure the necessary parameters. After which a minimum and maximum are set for particle size and circularity. The minimum particle size is defined as 85 % of the cross-sectional area as calculated with the mean fibre radius. The 85 % originates from the fact that the image processing procedure reduces the fibre diameter on average by roughly 8 % and a maximum of 15 %, as measured experimentally. The maximum particle size was set to a fibre under an angle of 70 degrees. This maximum particle size was set to 70 degrees to discard conglomerated fibres that were not successfully separated by water-shedding thus had large nonphysical cross-sections. The impact on detection rate of high angle fibres was neglectable, the likelihood of detection of fibres at higher angles than 70 degrees was far below 0,01 % as per Eq 7. The minimum circularity was set to 0.2 which was found to be effective in disregarding fractured and broken fibres from the analysis.

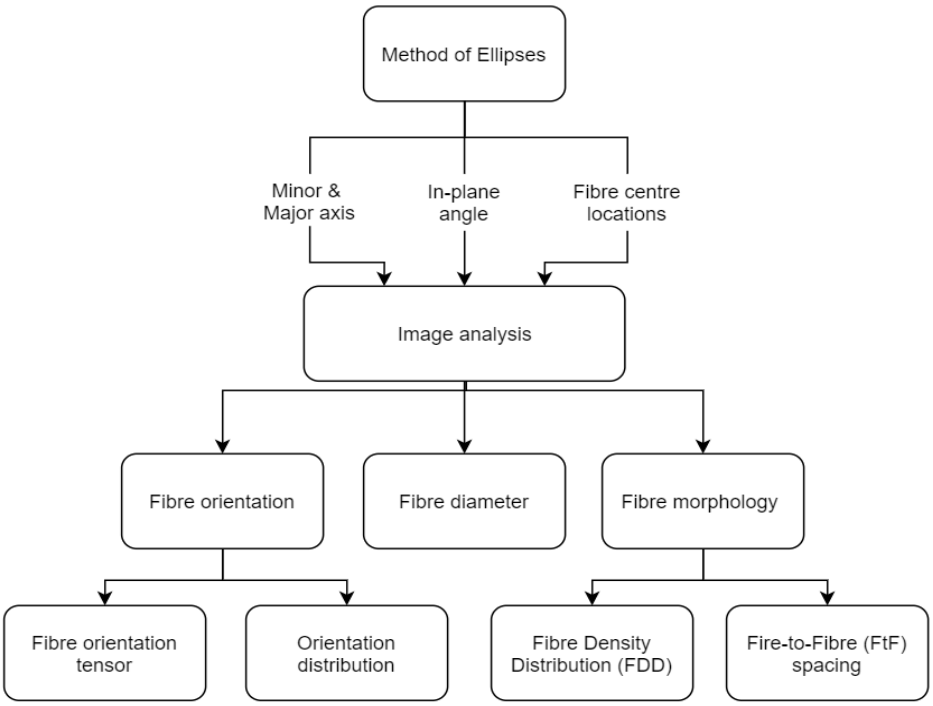


*Figure 43 method of ellipses outputs and analysis flow chart*

The MoE yields three parameters sets as output in csv file format, these are minor and major axes, in-plane angle and fibre centre coordinates. These parameters are used to analyse the microstructure descriptors: fibre orientation, diameter and morphology. From the fibre orientations analysis, two other descriptors can be derived, orientation tensor and orientation distribution. From the fibre morphology analysis, FDD and FtF spacing can be derived. An overview of the outputs and process flow can be seen in Figure 43. The specifics of analysis and derivation for the descriptors are further explained in their respective paragraphs in chapter 5.

# 5 Results

This chapter provides the experimental results on a general basis that apply to all studied materials. The difference between samples is covered in the discussion chapter paragraph 6.2 The experimental results are divided into four sections: image processing, fibre diameter measurement, fibre orientation analysis and fibre morphology analysis. Codes used to obtain these results can be found in appendix A - F.

## 5.1 Image quality and image processing

The quality of microstructural analysis is depended on the ability of the method to identify and measure fibres. During image acquisition and image processing, the chance of affecting the fibre cross-section is highest. To grade the effectiveness of image processing, the change of fibre cross-section has been monitored throughout the process. four stages have been identified in the characterisation method which irreversible affect the quality of microstructural analysis. These are image acquisition, segmentation, binarization and ellipse fitting.

Acquisition of the original micrograph on the Keyence VK-X1000 has been done at x20 and x50 magnification. Micrographs that have been acquired at x20 magnification can't be used for fibre shape-dependent analysis, i.e. orientation measurements. As can be seen in Figure 44, the image resolution of 1.45 pixel/micron is high enough to identify fibre but is too low for accurately measuring fibre shape. By using the fibre centre location and assigning an average fibre diameter to every fibre, a simplified approach can be used to calculate global and local $V_f$.

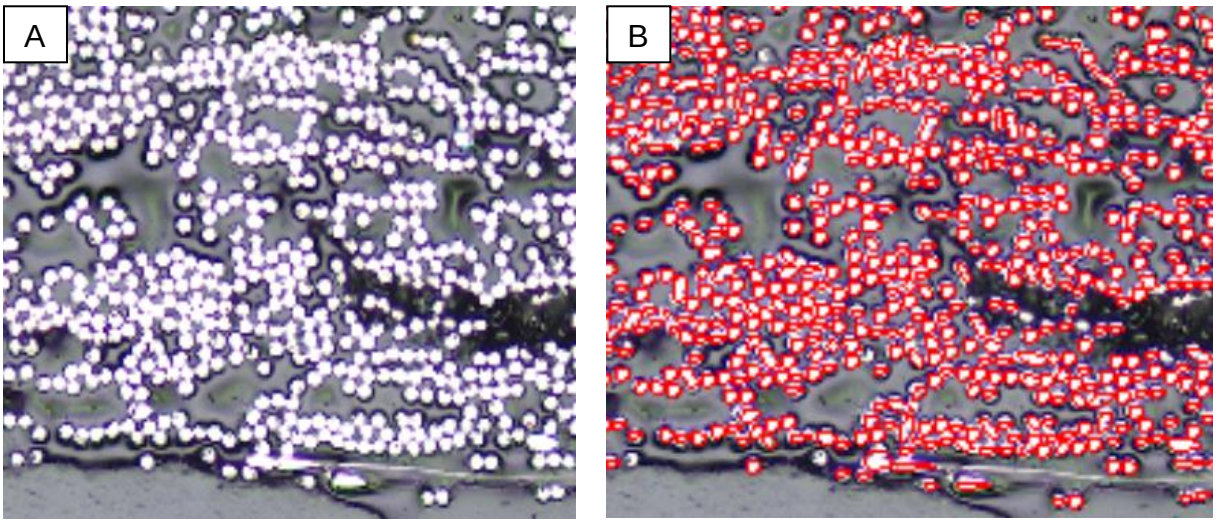


*Figure 44 (A) micrograph of sample L5 -3 at 20x magnification, (B) Disappointing fitment of ellipses on fibre cross-sections*

Micrographs that have been acquired at x50 times magnification are suitable for the analysis of individual fibres. These micrographs have a resolution of 3.63 pixels/micron which is high enough to identify and measure the shape of individual fibres, as seen in Figure 45A. This fibre was measured by hand in FIJI ImageJ and found to have a minor and major axis of 23 and 24 pixels, respectively. Noticeable is that the fibre boundary

in Figure 45A is still semi-difficulty to distinguishing by eye, thus the hand measurement has a degree of operator bias. All optical micrographs with high fibre packing and $V_f$ suffer from a lighting/shadow bias caused by the highly reflective fibres. Therefore, the fibre boundary on the "light" side is difficult to pinpoint. This effect was considered when training the WEKA segmentation tool.

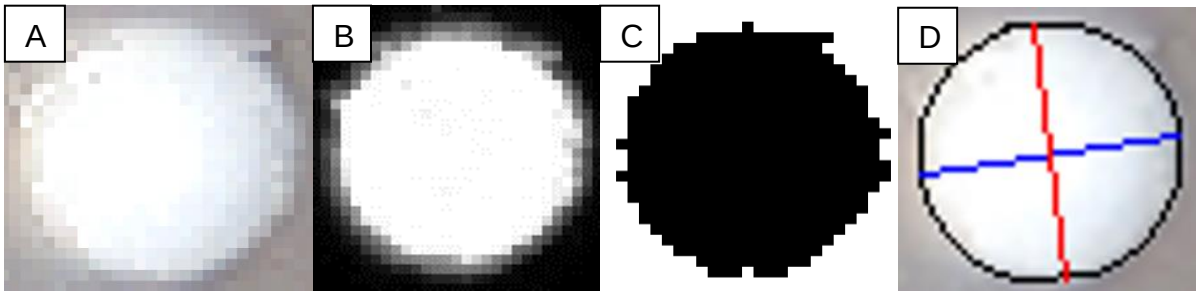


*Figure 45 comparison between (A) original image C1 50x, (B) probability map after segmentation, (C) binary image after thresholding and (D) fitted ellipse with minor and major axis (red and blue, respectively)*

During segmentation, the original micrograph is translated into an 8-bit probability map as can be seen in Figure 45B. The original fibre shape remains visible with a gradient at the borders. A grey value line-measurement was taken in FIJI ImageJ horizontally across the centre of the same fibre to measure the probability gradient, displayed in Figure 46.

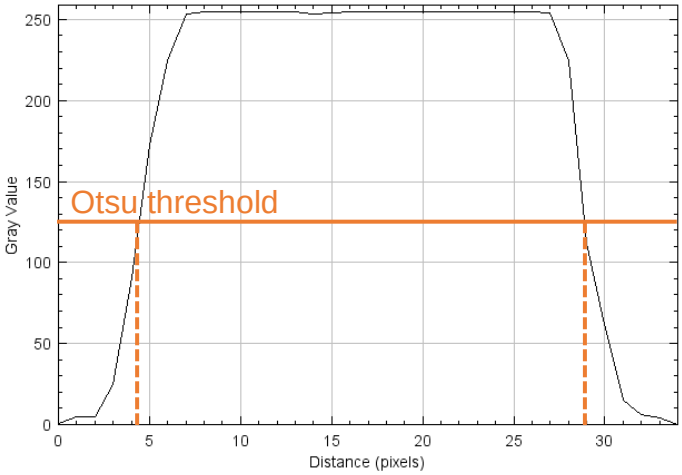


*Figure 46 Grey value line measurement across fibre, including Otsu threshold level.*

This line measurement shows the segmentation achieved a gradient at the borders from 0 to 255 of ±5 pixels, this shows that the WEKA segmentation could accurately classify the different phases without notably altering the fibre cross-section. The complete diameter measured from grey value ±0-255-0 is around 30 pixels. This length measurement includes the pixels which the WEKA segmentation is uncertain of if these are pure fibre or pure matrix. A hand measurement, done in FIJI ImageJ similar to the original measurement, gives a minor and major axis of 25 and 26 pixels, respectively. This measurement again includes a degree of operator bias because the boundary isn't distinctly defined by the probability.

The last stage in image processing is the thresholding of the probabilitymap. The Otsu thresholding method set the threshold for this probability map on the numeric value of 125 grey value intensity, as can be seen in Figure 46 other micrograph sample image processing procedures resulted in similar values. This is another indicator that the variance between fibre and matrix is significantly high after WEKA segmentation, suggesting that the quality of segmentation is adequate. After applying the Otsu threshold, the probability map is transformed into a binary image as can be seen in Figure 45C. Yet again the shape of the original fibre cross-section translates into the processed image. Hand measurement of the binary cross-section yields a minor and major axis of 22 and 23 pixels. The difference in minor and major axis including operator bias between the original and binary cross-section is only 1 pixel. This shows that fibre segmentation and thresholding has a limited amount of effect on the fibre shape and diameter.

The last step in the image processing is applying the MoE, the fitted ellipse is shown in Figure 45D. This automated process yielded a measurement for the minor and major axis of 24.17 and 24.28 pixels, respectively. These values are decibel numbers because the automated method in FIJI ImageJ identifies and measures the absolute axes length which can be under an angle on a cartesian grid. The automated method calculated the axes length with roughly 1-pixel accuracy relative to the original micrograph hand measurement. Other measurements done in a similar way across samples have resulted in similar accuracies.

The biggest challenge for the presented method is to accurately identify and measure close-packed and touching fibres, as explained in 4.3.1. By applying the distance transform water-shedding procedure, touching fibres have been separated from each other. Unfortunately, this procedure results in straight lines on the former boundary between fibres. When applying the MoE as developed in this thesis, the straight watershed lines have little effect on the shape and fitment of the ellipse as can be seen in Figure 47.

This shows that the developed method can accurately identify, segment, threshold and measure the fibre shape in a microscopy image.

*Figure 47 visualisation of minor and major axis measurement on binarized image sample C1 x50*

## 5.2 Fibre diameter

To validate the accuracy of the method, and allow for future aspect ratio analysis, the fibre diameters of all fibres have been measured. Intermediate modulus (IM) CF often has a stated fibre diameter of 7µm as specified by the original manufacture. Mesquita et al. [52] has shown that the fibre diameter of IM CF is not a fixed value but shows distribution around the stated fibre diameter as can be seen in Figure 48.

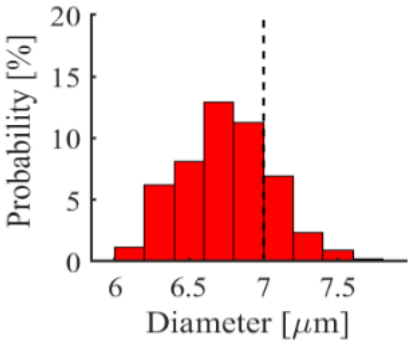


*Figure 48 Histogram fibre diameter carbon fibres [ Mesquita et al.]*

The minor axis of a fitted ellipse represents the fibre diameter. The minor axis was measured for 14299 fibres in sample C1 x50 and displayed in Figure 49. The mean and median fibre diameter was found to be 6.9µm with a standard deviation of 0.37µm, this agrees with the values found by Mesquita et al. indicating that determination and measurement of the minor axis are accurate.

Histogram: length minor axis – fibre diameter
Sample C1 x50

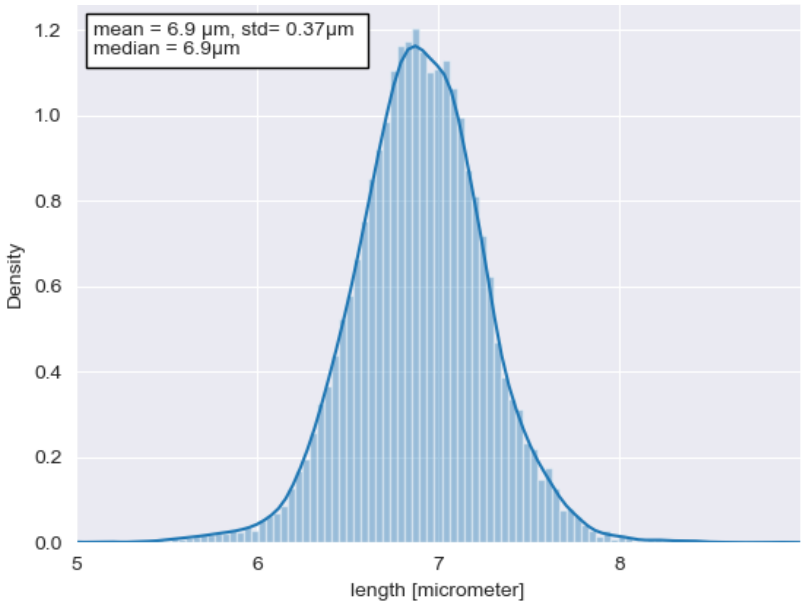


*Figure 49 C1 50x Length of minor axis which defines the measured fibre diameter. Mean value length 6.9 µm with a standard deviation of 0.37µm*

## 5.3 Fibre orientation

Fitment of the ellipses to the original fibre cross-sections is a direct indication of the accuracy of the method. To visually validate the fitment of ellipses to the original fibres, the ellipses were superimposed on the original image. On initial review, the fitment of ellipses is satisfying, with some ellipses showing minor deviations from the original cross-section, as can be seen in Figure 50.

Worth noting that; damaged or fractured fibres have been ignored during particle measurement in FIJI ImageJ by setting a threshold for minimum circularity of 0.2.

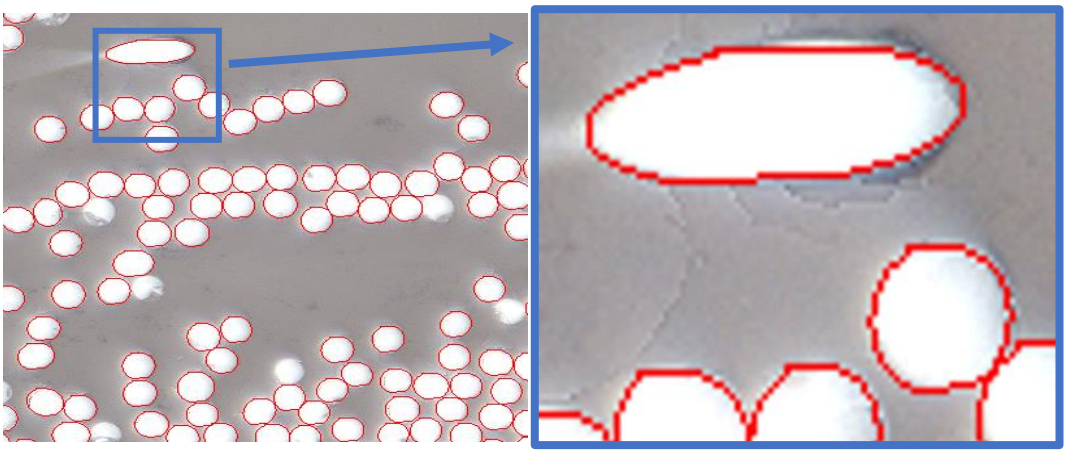

*Figure 50 C1 50x ellipses superimposed on small section of the original image, including enlarged section.*

The orientation of all 14299 measured fibres for sample C1 50x are plotted in Figure 51 below. The histogram shows a mean OoP orientation of 20.23 degrees with a standard deviation of 8.7 and a median of 18.96 degrees.

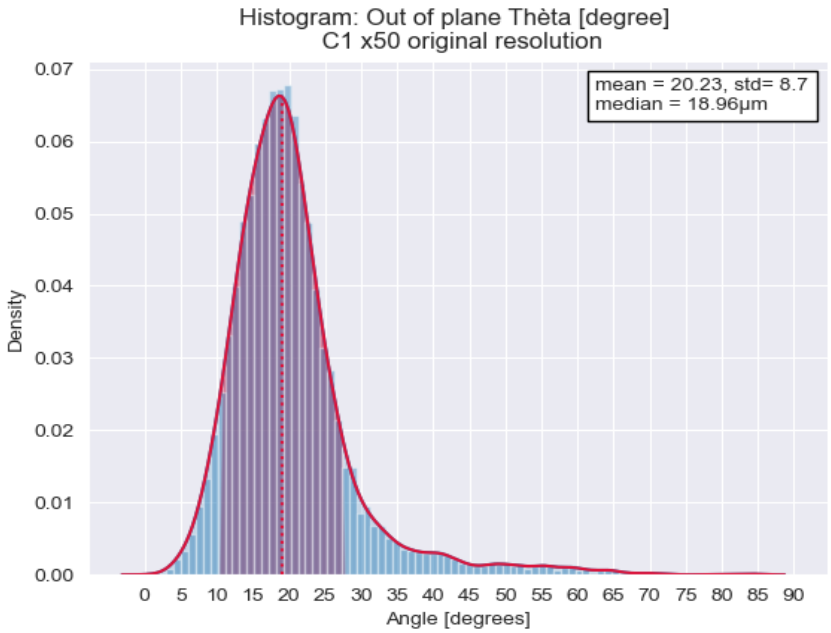


*Figure 51 C1 50x Histogram OoP angle original resolution. Mean value 20.23 with a standard deviation of 8.6 degrees*

To verify whether the histogram was correct, minor and major axes of every ellipse were plotted and superimposed on the original image to check for fitment and anomalies, as can be seen in Figure 52.

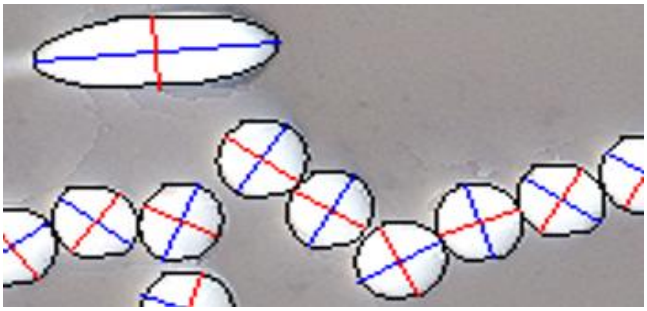

*Figure 52 C1 50x superimposed ellipses with axis on original image, red being the minor axis and blue being the major.*

To compare the difference in minor and major axes, both are plotted as a histogram to see the difference in distribution, as can be seen in Figure 53.

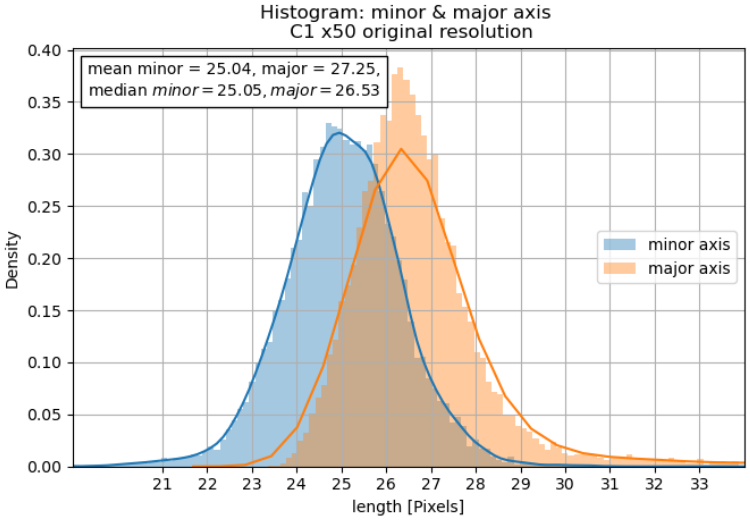


*Figure 53 C1 50x Histogram of both minor and major axes.*
*Mean values for minor and major axes are 25.04 and 27.25, respectively*

The mean for the minor and major axes is 25.4 and 27.25 pixels, and the median for the minor and major axes is 25.05 and 26.53 pixels. The difference in mean and median values for the minor axis is negligible, indicating a close-fitting normal distribution around the fibre diameter. The difference between the mean and median for the major axis is caused by the presence of high angle fibres outside the range of Figure 53, these fibres are not present in large numbers, but affect the distribution including the KDE line. The difference in mean values is 2.21 pixels or 7 %, which equates to 0.6µm. And the difference in median values is 1.48 pixels or 5.5 % resulting in a difference of 0.4µm. The maximum resolution of the Keyence VK-X1000 is stated as ±300-400nm for optical light measurements by the manufacture, indicating that the developed method is measuring a difference in length for the minor and major axis at the limit of the microscope. This 5-7 % difference in the ellipticity of the fibre cross-sections is causing the 18–20-degree OoP orientation as can be seen in Figure 51

After the analysis of multiple samples resulted in similar OoP mean distributions, as can be seen in Figure 54. The focus was shifted to the method of calculating OoP orientation.

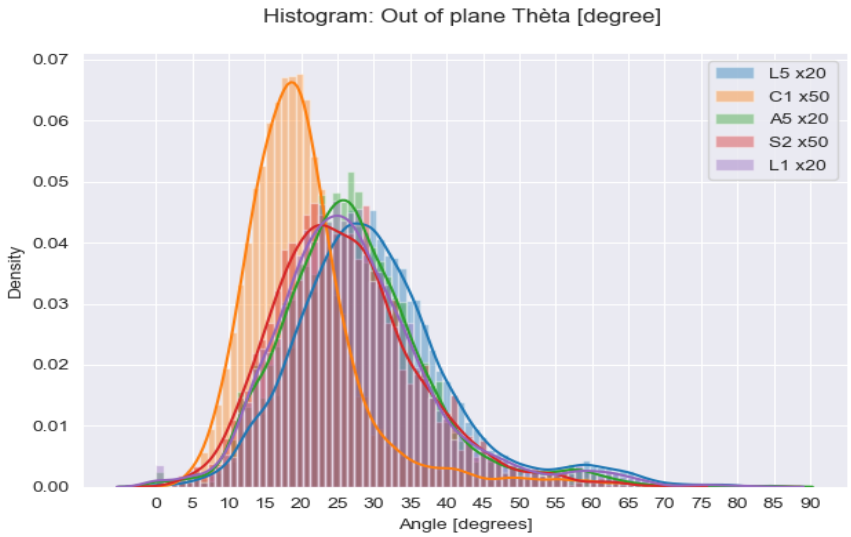


*Figure 54 Selection of multiple samples and their OoP orientation*

When reviewing the behaviour of the arccosines function as shown in Figure 55, the function is non-linear and highly sensitive to small differences in minor to major ratio. This especially manifests near the minor-major ratio of 1, meaning a circular cross-section. A deviation of 1 % from this perfect circle produces an OoP angle of 8 degrees.

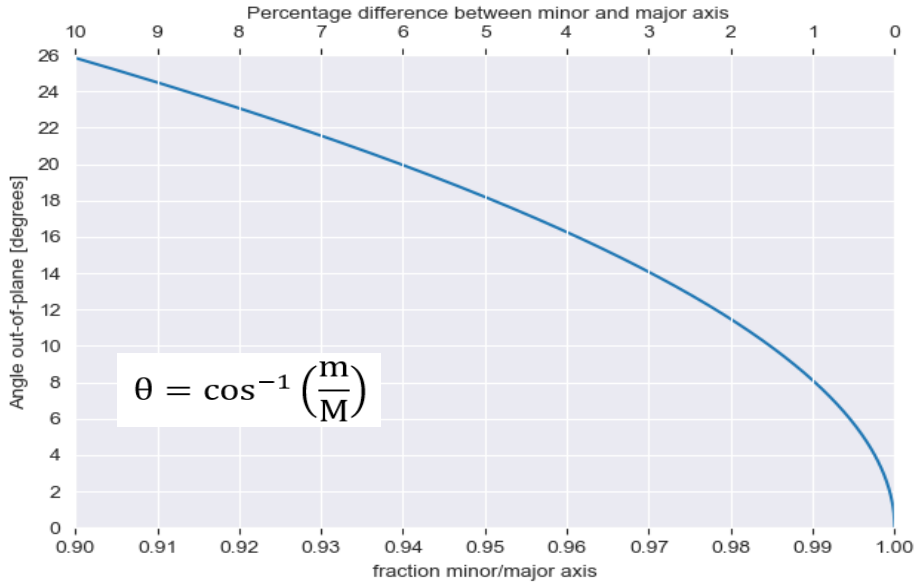


*Figure 55 arccosines function*

To achieve this 1 % difference in minor/major ratio would equate to a required accuracy or minimum resolution of 0.07µm (0.25 pixels) when the minor axis is 25 pixels. This 70-nanometre resolution is unobtainable with an optical light microscope.

As discussed in paragraph 5.1, the developed method has an accuracy of roughly 1 pixel or 4 % when translating fibre shape from micrographs taken at x50 into binary images. Therefore, the theoretical minimum OoP orientation is 16 degrees when considering a 25-pixel minor axis.

It was investigated whether digitally increasing resolution would reduce the error sensitivity of the method. Resolutions were increased by 200 % via image scaling with cubic interpolation in the open-source image manipulation program GIMP version 2.10, as can be seen in Figure 56. This resulted in a virtual resolution of 7.26 pixel/µm or 1-pixel equalling 138nm. The biggest visual effect caused by the increased resolution was smoothing of the boundary between fibre and matrix.

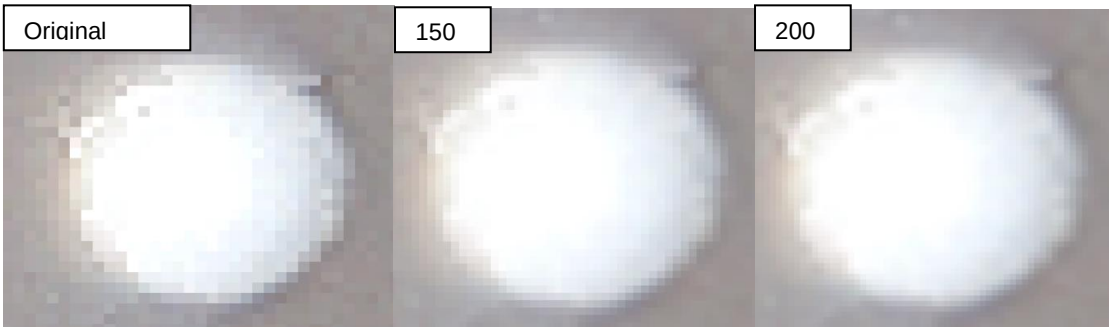


*Figure 56 Difference in image sharpness between resolutions.*

The image processing pipeline was repeated on the 200 % high-resolution image, including training a new WEKA classifier. To check fitment, ellipses with axes are superimposed on the 200 % micrograph image. These show good if not better fitment to the fibre cross-sections when compared to the original resolution, because of the smoother ellipses and axes.

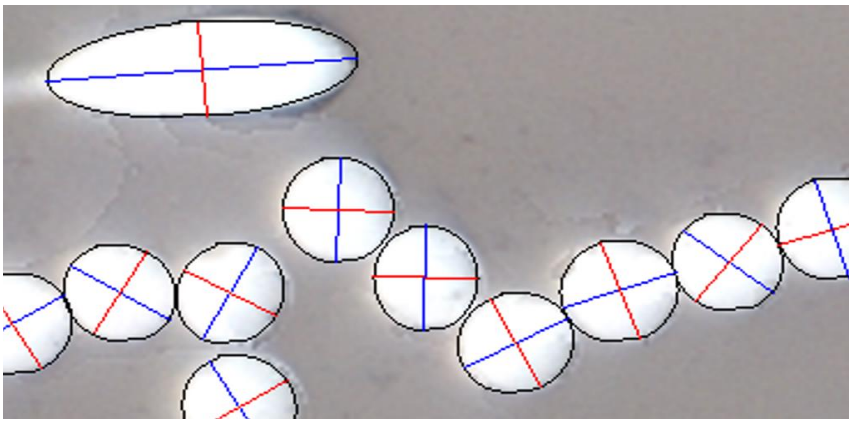

*Figure 57 Fitment of ellipses in 200 % resolution image of C1 50x*

The OoP orientation and minor-major axis of 13944 fibres were measured and displayed are in Figure 58.

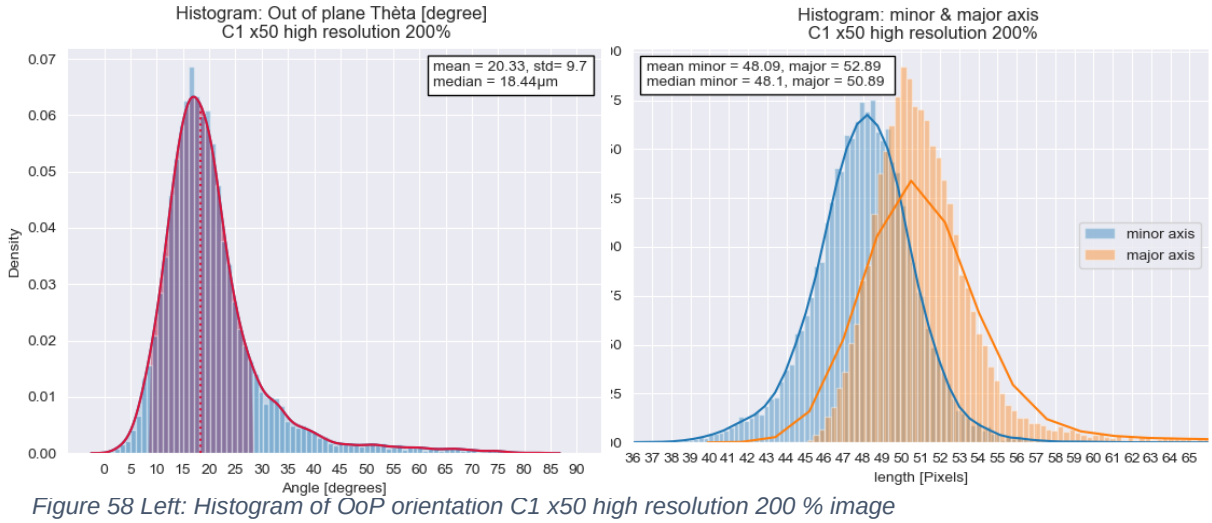


*Figure 58 Left: Histogram of OoP orientation C1 x50 high resolution 200 % image*
*Right: Histogram both minor and major axis C1 50x high 200 % resolution*

The mean and median OoP orientation is 20.33 and 18.44 degrees, respectively with a standard deviation of 9.7 degrees. When comparing the original and increased resolution histogram, the difference between the two is minimal.

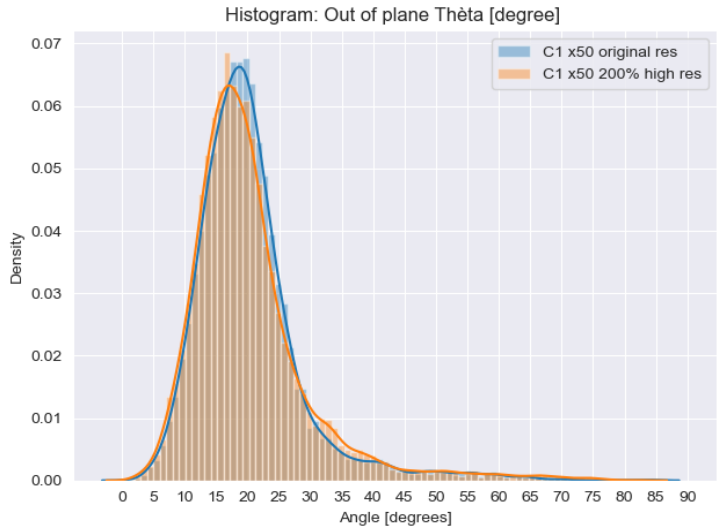


*Figure 59 Histogram OoP orientation of sample C1 x50*

The mean and median minor-major axes were found to be 48.09 - 52.89 pixels and 48.1 – 50.89 pixels, repetitively. By increasing the resolution by 200 % the minor-major axes have nearly doubled in length. Not being precisely double in length can be a combined effect of a difference in the WEKA segmentation tool and more smooth and thus less sharply distinguishable boundary between fibre and matrix, which makes segmenting harder. More notably, the width of both the minor and major distribution has doubled, indicating a more inaccurate measurement. The difference in mean minor-major axis is 4.8 pixels or 10 %, the median variance is 2.79 pixels or 6 %. The conclusion can be made that digitally increasing resolution by 200 % has little to no effect on decreasing the error sensitivity of the method, furthermore, it harms the accuracy of minor-major axis distribution.

### 5.3.1 Verification of fibre orientation measurement

To verify the presented method tendency to yield biased OoP orientation distributions, a known aerospace-grade thermoplastic PEEK tape (1 layer) micrograph cross-section was analysed in the same manner as the other samples. A partial section from the complete cross-section is shown in Figure 60. This aerospace reference material was supplied and studied by Gomarasca et al. [53] which measured the microstructure with both optical microscopy and micro CT, characterising its 3D fibre morphology. The reported orientation for 95 % of its fibres was found and proven to be within ±3° with respect to the main axis.

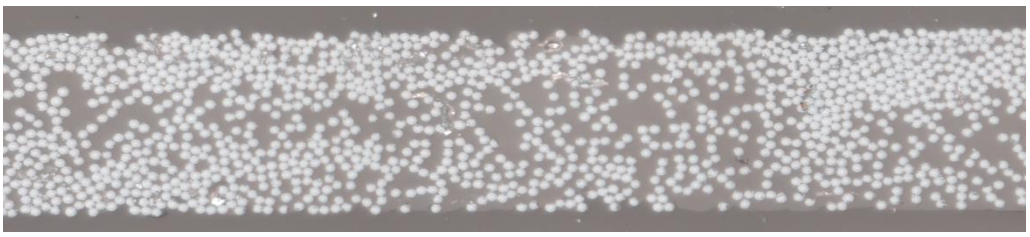

*Figure 60 cross-section overview taken at 50x of aerospace tape, image provided by Silvia Gomarasca*

Results from applying the developed method on the aerospace reference material yielded a mean and median OoP distribution of 20 and 19.41 degrees, with a standard deviation of 6.85 as can be seen in Figure 61. This verifies that the developed method has an intrinsic bias of measuring OoP angles around 20-25 degrees in a varying degree of materials with distinctly different surface textures because of the high error sensitivity of the arccosines function used to calculate the OoP orientation.

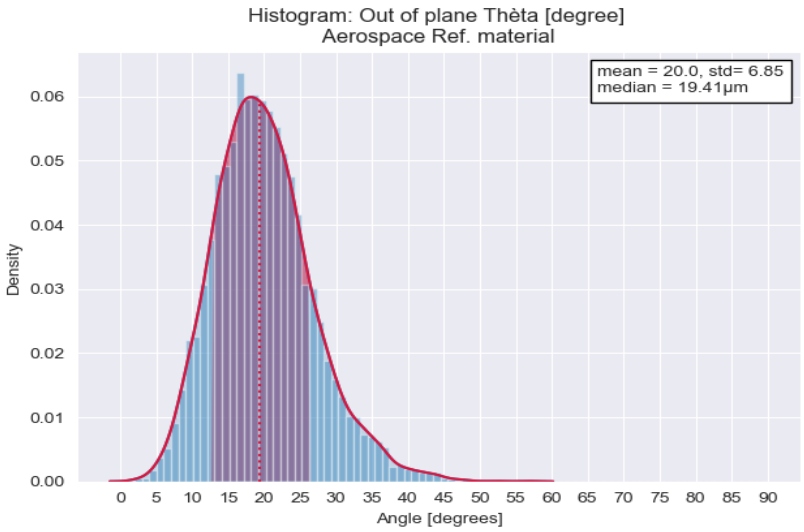


*Figure 61 Histogram of aerospace grade reference material*

## 5.4 Orientation tensor

The accuracy of the orientation tensor is directly related to the calculated OoP orientation angle. This value has proven to be problematic since it shows a bias towards 20 degrees across various samples with noticeably different surface textures and fibre angles. When this value is combined with the in-plane angle in the non-linear and quadratic functions to construct the orientation tensor, a non-reliable value or descriptor is calculated.

The decision was made to provide results for the A11 and A22 orientation tensor components in this paragraph to show the behaviour of a proven biased measurement. In Figure 62 the through-thickness $A_{11}$ and $A_{22}$ components for both the C1 x50 and aerospace reference material have been calculated with bin step size 1 % of the thickness. These through thickness measurements display the change of tensor component as a mean average across the width of the tape material when moving from top to bottom. These measurements can also be performed for analysing the change across the width when moving from left to right. Both $A_{11}$ and $A_{22}$ show average values between 0.2 and 0.3 for the C1 x50 and aerospace reference sample, with a standard deviation of roughly the same size as the mean. Indicating an inaccurate measurement.

For this reason, the unambiguous orientations were not measured by consecutively grinding and polishing the sample to calculate $A_{13}$ and $A_{23}$. This process uses the originally measured in- and OoP orientations to verify the new position of the fibres, but since the measured orientations have large biases, the new positions were all out of range and could not be identified. The code to calculate and analyse $A_{11}$-$A_{22}$ components can be found in Appendix G.

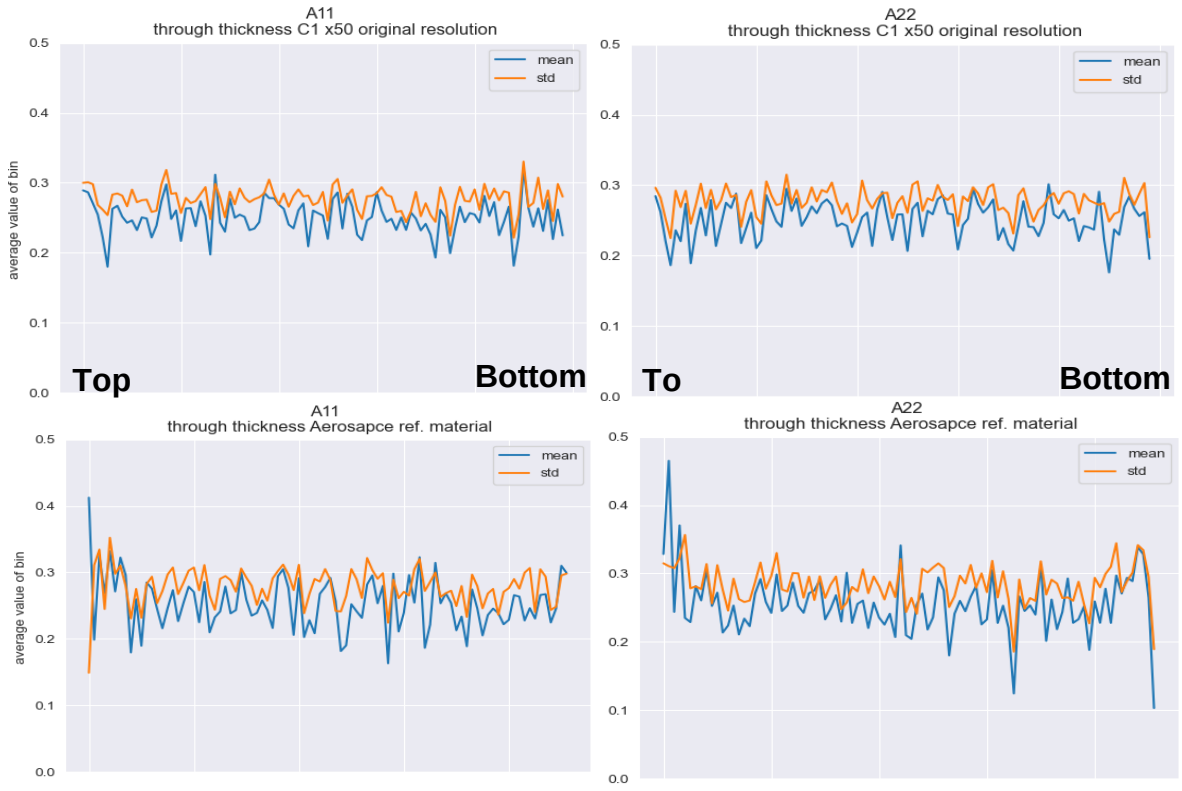


*Figure 62 Tensor components A11 and A22 for the C1 x50 and Aerospace reference material.*

## 5.5 Orientation distribution

The precise OoP orientation cannot be trusted since the error sensitivity of the arccosines introduces a biased result. Nevertheless, the method is reliable in finding areas with orientations deviating from the mean. In Figure 63 the through-thickness and across width OoP measurements are shown. The average OoP was calculated per bin slice. Binning was done with a constant step size of 1 % thickness or width, respectively. The through-thickness graph shows a characteristic spike near the bottom of the tape. When this graph is compared with the orientation map shown in Figure 64, a clear correspondence is found near the bottom enclosed in blue with an insert showing the real cross-section.

Two other areas near the top have been enclosed in blue with a corresponding insert showing the sensitivity of this method to locate deviating orientations. The across width graph is less sensitive to areas with deviating orientations, this is because the bunching of highly orientated fibres is an effect that occurs mainly across the width, thus measurable with the through-thickness measurement.

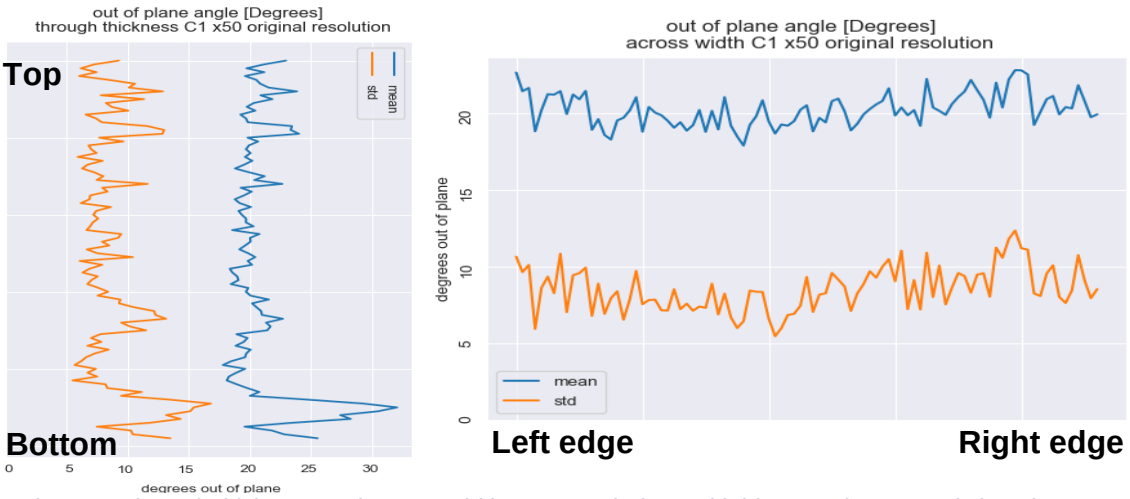


*Figure 63 through thickness and across width OoP graph done with bin step size 1 % axis length*

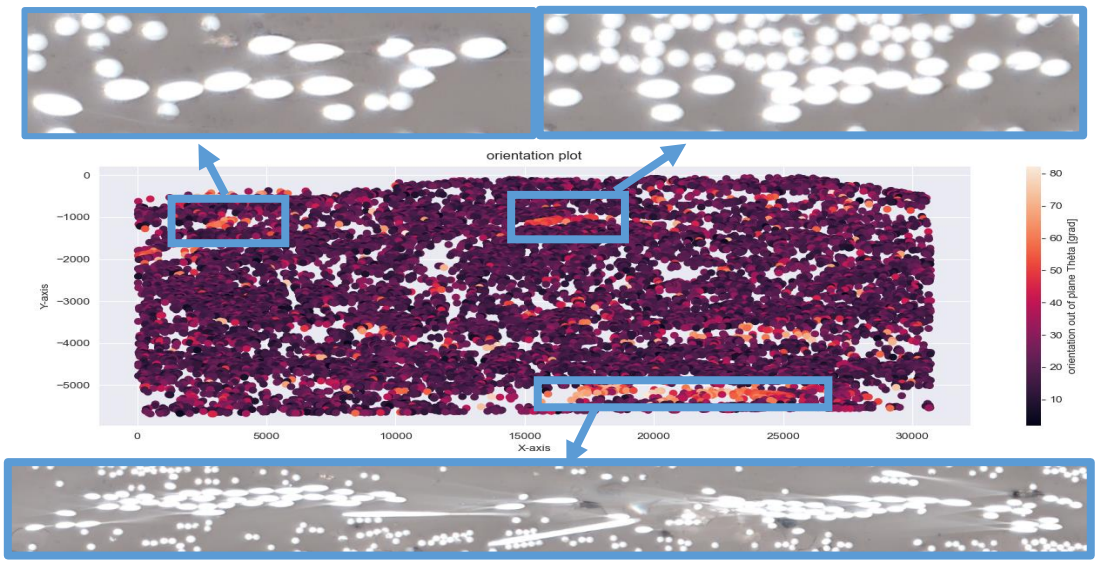


*Figure 64 OoP orientation map C1 x50*

## 5.6 Fibre morphology

### 5.6.1 Fibre Density Distribution (FDD)

The FDD was measured through-thickness and across the width. Binning was done with a constant step size of 1 % thickness or width, respectively. This respective step size was multiplied by total width or thickness to calculate the total surface area of the specific slice. The area covered by ellipses within the slice was divided by the slice area to calculate the average local $V_f$.

Figure 65 shows the result of the FDD across the width of sample C1 x50 with its cross-section seen in the insert. Figure 66 shows the FDD through-thickness of sample C1 x50 with the left half of the cross-section as insert. Multiple dips and peaks can be seen in both FDD which correspond with the fibre rich and poor areas. The relatively low $V_f$ values are calculated through and across the samples, this is caused by the comparatively large resin areas between the fibre packs, and resin areas surrounding the sample still in the frame of the cross-section.

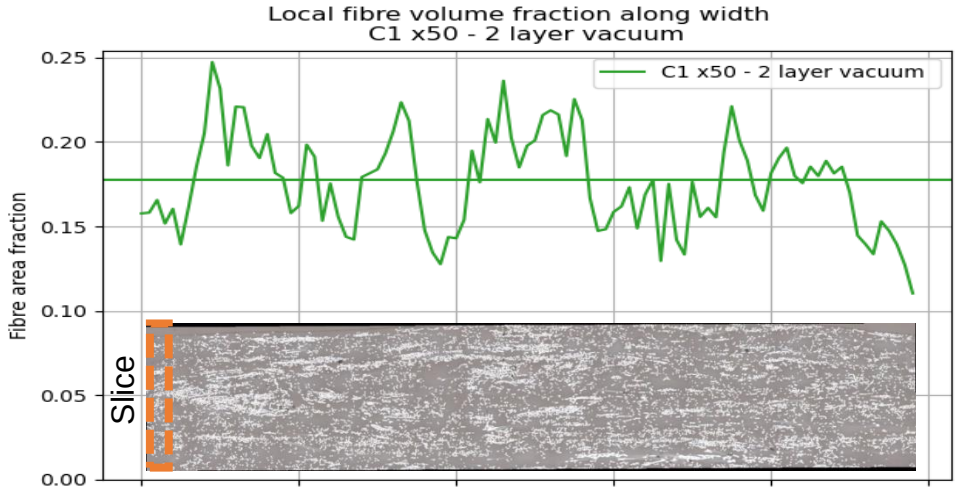


*Figure 65 Local Vf across width in sample C1 x50*

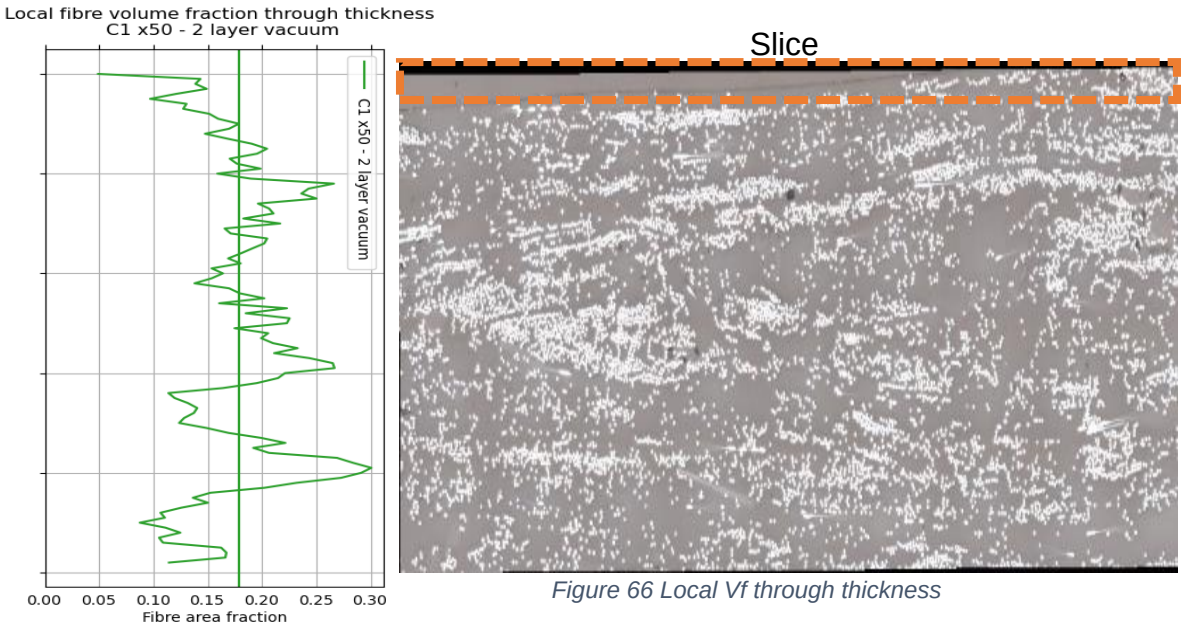


*Figure 66 Local Vf through thickness*

To get a more accurate localised $V_f$ result, the FDD is superimposed on the original image. The localised FDD is calculated by dividing the micrograph cross-section into segments of 100x100 pixels or 27.54x27.54 µm, roughly four fibre diameters. The centre locations and surface areas of all fibres are known from the MoE. The surface area of every fibre is assigned to its centre coordinate, afterwards, the area of all fibres within the segment were divided by the segment area, yielding the localised $V_f$. When lower resolution 20x magnification micrograph samples were analysed, segments of 40x40 pixels equivalent to 27.54x27.54 µm or roughly four fibre diameters were used. Because the MoE didn't result in reliable fibre shape measurements in 20x magnification images, a perpendicular fibre surface area with a diameter of 6.8 µm was assigned to every centre location to calculate local $V_f$. This will result in a slightly lower localised $V_f$.

When reviewing the localised FDD in sample C1 x50, as can be seen in Figure 67, areas of low and zero $V_f$ can be seen between areas of high $V_f$ causing the relatively low global $V_f$. Some squares show >0.7 $V_f$ this can be accounted for by the fact that $V_f$ is calculated by assigning the surface area of the complete fibre to the centre location, if the centre location is just within the segment the complete fibre surface is counted to be within that segment. The effect also works the other way around, where part of the fibre is in the square but the centre location is not, thus not adding to $V_f$.

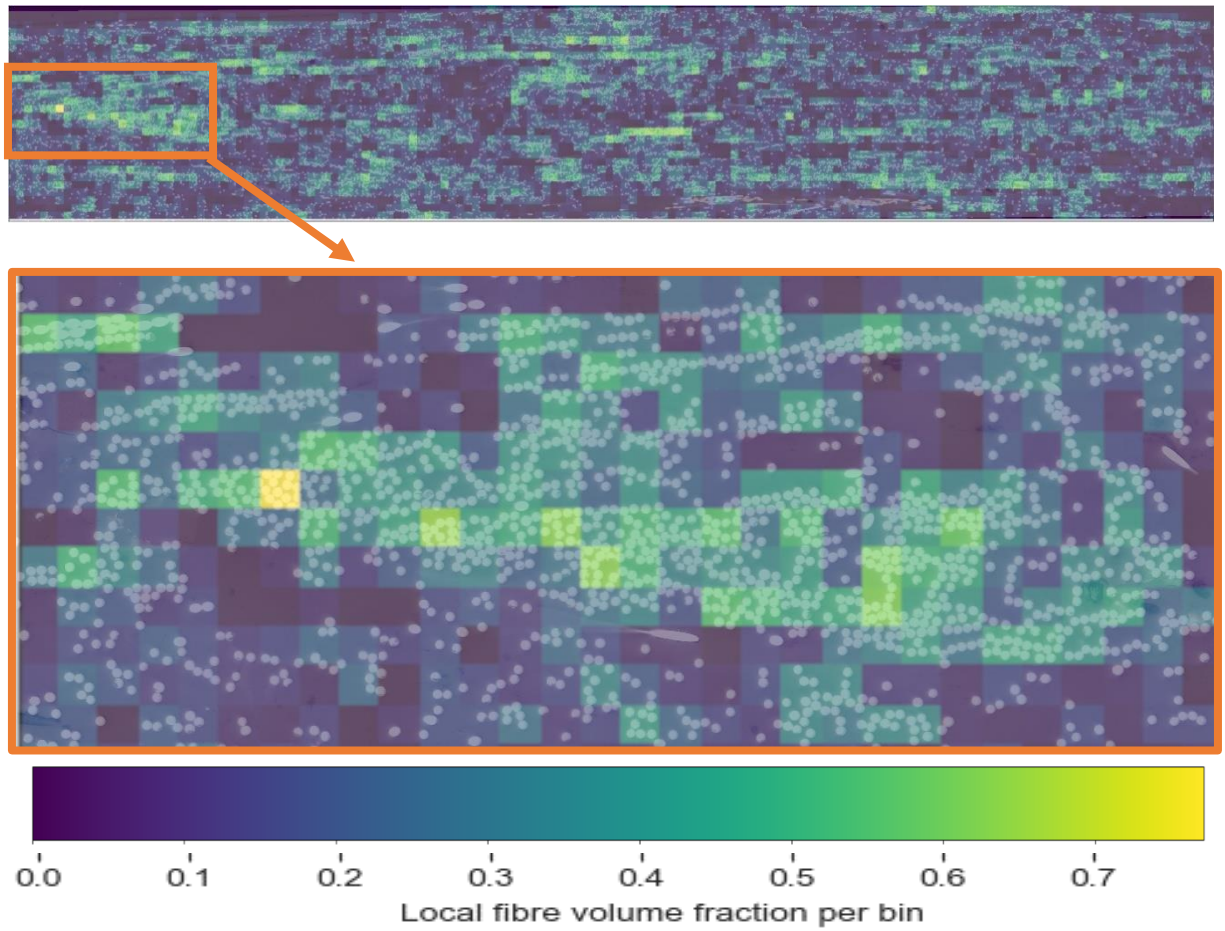


*Figure 67 C1 x50 FDD displaying local Vf*

### 5.6.2 Fibre-to-Fibre spacing

To measure the nearest neighbours in material samples, a K-D tree is constructed in python by the Scipy spatial KDTree function. For every fibre, a distance query is created with an array containing the first four nearest neighbours. The distance of those four nearest neighbours is plotted on a cumulative KDE plot as can be seen in Figure 68. The neighbouring distance is normalised by subtracting the average fibre diameter, in some cases, this leads to the lower tail of the cumulative KDE plot at zero micron not showing fibres that have a slightly smaller diameter than average. The 80$^{th}$ percentile is calculated for the first four nearest neighbours.

For the C1 x50 sample, this results in the distances: 1.9, 6.25, 9.2, 11.75 µm. As a reference the cumulative KDE for the aerospace reference material is also shown in Figure 68, this aerospace-grade material measures 0.87, 1.97, 3.85, 5.77 µm for the 80$^{th}$ percentile of the first four neighbour distances.

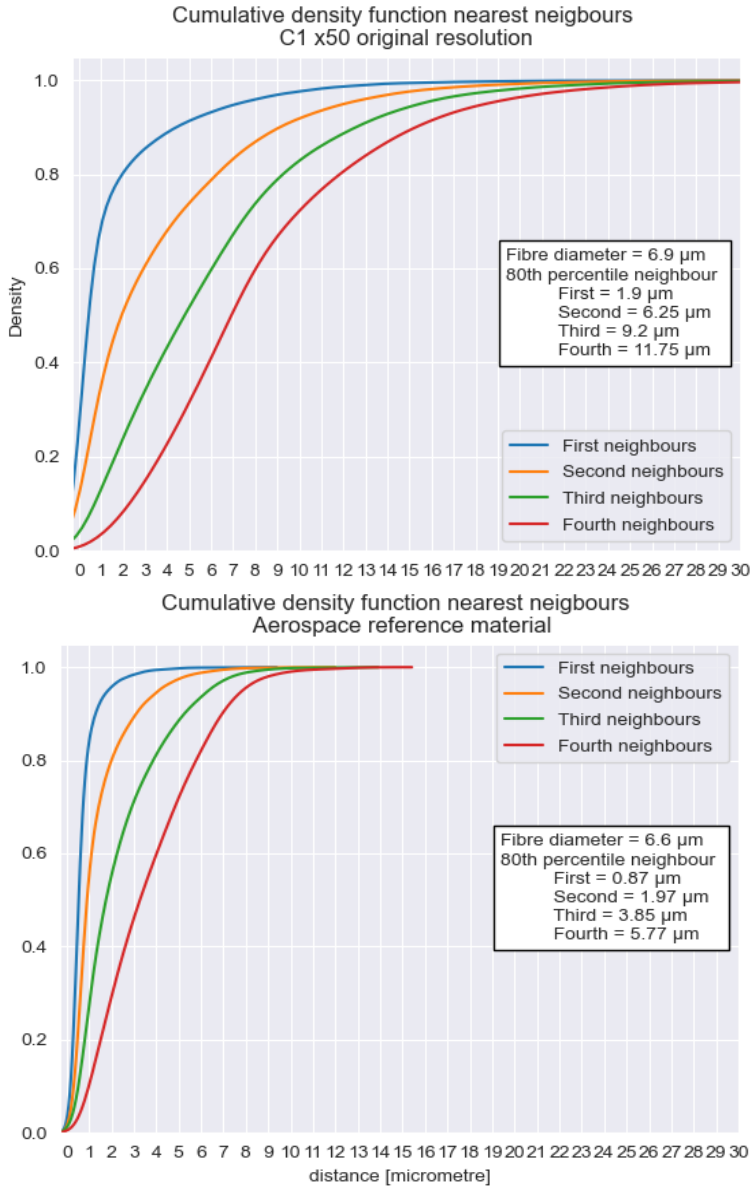


*Figure 68 C1 50x first four nearest neighbours*

# 6 Discussion

This chapter discusses the shortcomings of the developed characterisation method and solutions on how to resolve the error sensitivity of the method. Afterwards, a comparison between a selection of samples is made to compare the analysis results.

## 6.1 Method of ellipses

Literature reports extensively on results obtained from the MoE on both randomly orientated and highly aligned glass and carbon fibre samples. These aligned fibre reinforced samples were studied in perpendicular or near perpendicular cross-sections.

It was expected from these results that the MoE would allow for accurate orientation measurements. However, after analyses of multiple samples, including virgin aerospace-grade unidirectionally thermoplastic tape, all measurements showed a similar OoP orientation bias of ±20-25° with a standard deviation of ±6-10°. The ±20° OoP orientation cannot be taken as a zero value for the method because samples with clearly different and inhomogeneous surface textures and fibre orientation show similar values, making the normalised value void.

After excluding errors introduced by embedding, image acquisition and analysing, the same biased measurements were observed. The culprit was eventually found to be the trigonometric way of calculating the OoP orientation. From studying the error sensitivity of the arccosines, it was hypothesized that increasing resolution would decrease the error sensitivity of the method. However, the 50x magnification micrographs already had a resolution of roughly 0.3µm per pixel which is near the theoretical limit of optical light microscopy.

This implies that a limit has been reached in image resolution and thus fibre orientation measurements accuracy achievable by desktop optical light microscopy. Using a scanning electron microscope to achieve higher resolutions would have been possible, but then again defeats the idea behind the thesis of promoting the development of rCF composites by quick and affordable R&D. The effect of image processing steps on the accuracy of the developed method has been disused earlier in their respective results paragraph, other factors which impact the accuracy of the orientation measurements which thus far has been unmentioned are mapping of a circular fibre onto an array of square pixels and the actual shape of CFs.

Examples of bean-shaped CFs are abundant in literature, and even for high-quality CFs it has been experimentally found by O'Connell and Duckett [54] that the upper bound deviation in the ellipticity of CFs was around e=0.011 or 1.1 %. When the minimal achievable OoP orientation is reviewed by the geometrical relation:

$$\text{minimal}\,\theta = \cos^{-1}(1 - e)$$

where e is the degree of ellipticity. [35] The results indicate that the minimum achievable OoP orientation of fibres when perfect perpendicular to the cross-sectional

plane would be calculated to be at a mean angle of 8° because of the error sensitivity of the arccosines function. This combined with the errors induced by fibre shape measurements and image processing equates to the standard MoE being unfit for determining fibre angle in high UD materials when studied in perpendicular cross-sections.
Therefore, research publications that merely use the MoE on (near)perpendicular cross-sections to evaluate orientations of re-aligned UD materials and claim high alignment, should be reviewed critically. Research results often state that they have achieved a standard or two sigma deviation (68 - 95 % respectively) of fibres orientation within a few degrees.
Analysis of the standard MoE shows that the method simply cannot produce reliable information about orientation distributions of highly aligned UD materials because of its inherent over-sensitivity.
The orientation distribution, often stated as an “x-percentage” of fibres are within “±y-orientation”, are more likely to be the sigma-deviation measured from the biased orientation distribution. For example, multiple measurements performed during this thesis show standard deviations of fibres with alignment within ±6 - 10 degrees, as can be found in paragraph 5.3. This could be claimed as a success considering the tremendous effort it takes to re-align discontinuous fibres – but this statement does not consider that the distribution was biased around an angle of roughly 20° originating from a proven error sensitive calculation method.

After the presented shortcomings of the MoE became apparent during this thesis research project, it was found by re-examination literature that the topic is hardly ever discussed in detail by studies that use the MoE method research.

When specifically searching for literature on the problems encountered with the MoE yielded studies from the 1990s and early 2000s. [55]–[57] These studies suggest an alternative to the common perpendicular cross-sectional micrographs measurements. They have proven that analysing highly elliptical fibre cross-sections, rather than near-circular, will result in better estimates of fibre orientation. This is due to an error in measuring minor-major axis results in a smaller fractional impact on elliptical value. The stated technique for minimising the orientation errors is to section the sample at an angle α of 45º, or even 60º to the main fibre axis Z, as can be seen in Figure 69A. Afterwards, the induced angle α can be transformed back to the perpendicular plane to yield the main fibre orientation direction by:

$$\theta = \cos^{-1}\left(\sin\alpha \cdot \sin\theta' \cdot \sin\phi' + \cos\alpha \cdot \cos\theta'\right)$$

$$\phi = \tan^{-1}\left(\frac{\cos\ \alpha \sin\ \theta' \sin\ \phi' - \sin\ \alpha \cos\ \theta'}{\sin\ \theta' \cos\ \phi'}\right)$$

To compare the reasoning behind the transform, as stated earlier when analysing a perpendicular cross-section, a 5 and 1 % difference in minor-major ratio results in 18 and 8° OoP orientation, respectively.
When analysing the 45° sectioned samples a 5 and 1 % difference in minor-major ratio would lead to a 3 and 0.5° OoP angle, respectively. When analysing 60° sectioned samples this error would reduce to 1.64 and 0.33° for the 5 and 1 % difference in a minor-major ratio. This small linear error sensitivity would allow for normalising the OoP orientation distribution. The possible introduced error by sectioning or cutting the sample can be accounted for by applying the earlier mentioned transformation equations.
The difference in resulting OoP measurements with varying sectioning angles are shown in Figure 69B.

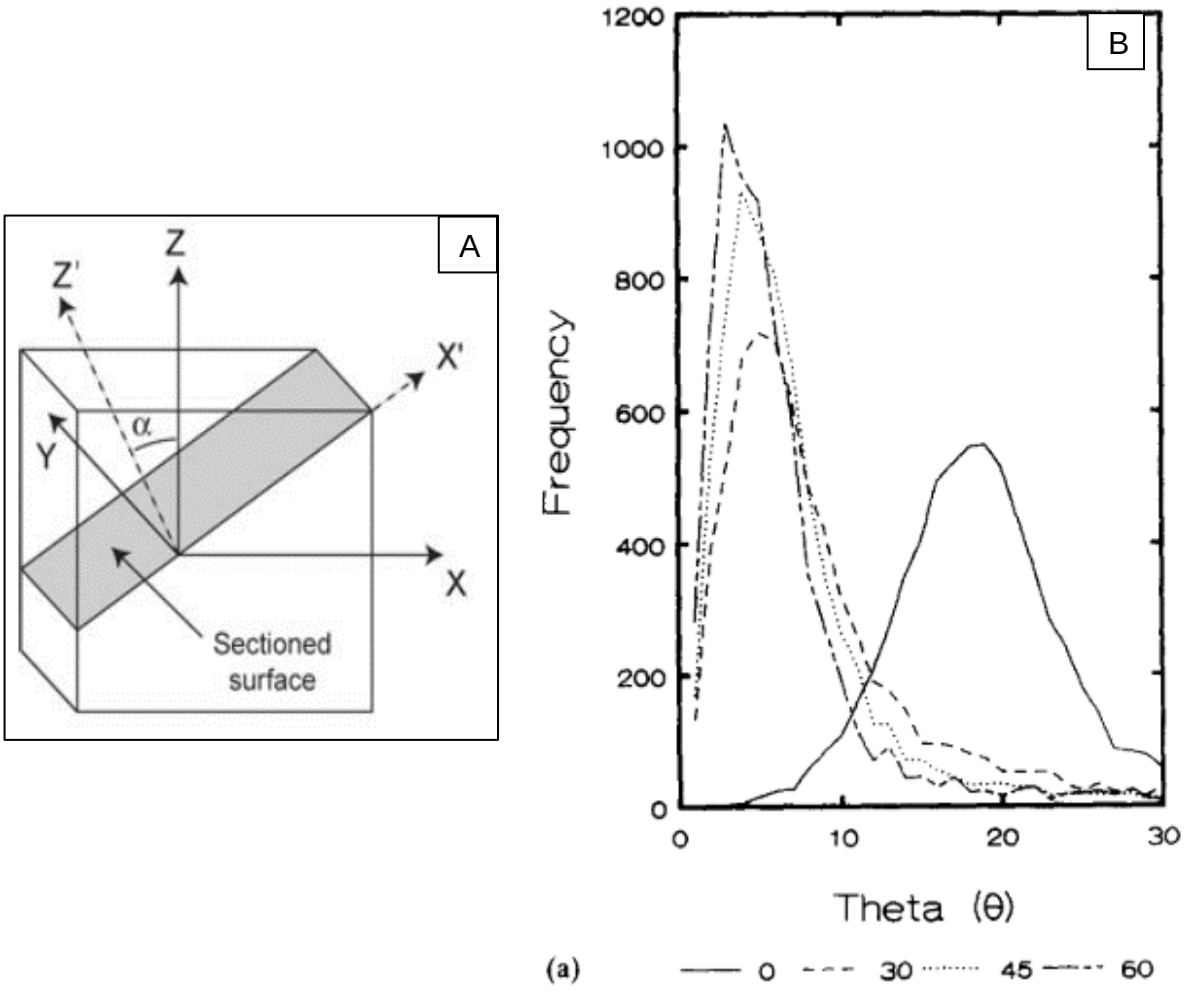


*Figure 69 (A) overview of primary plane and induced cutting angle alpha. [ Clarke et al. 2000] (B) results of different sectioning angles on the orientation distribution [ Hine et al 1993]*

## 6.2 Microstructure difference between samples sets

During the sample preparation, it became apparent that the different sample sets featured distinctly different surface textures and FOD. Material from sample sets 1 (A-B-C-D) had superior surface textures when compared to material from set 2 (L1) and 4 (S). Material from sample sets 2 and 4 had a distinguishable waviness along the length of the tape. Because the FOD measurements were flawed, as discussed earlier, this waviness has not been characterised. Besides this waviness, sample set 2 and 4 had a fluffy and less reflective surface texture.

It is hypothesized that the surface texture and microstructural quality in tapes are directly related to the sheen or reflectiveness of the material.
Increasing the reflectiveness of the material by decreasing the “fluffiness” or skewed fibres on the material surface would also directly impact the $V_f$ in multi-layer composites.
As can be seen in Figure 70, it only takes one skewed fibre in between a highly compacted area to impact the local $V_f$ significantly. It has been observed in microscopy images that highly orientated single or bunches fibres are always distributed across the tape width, as can be seen in Figure 71 and Figure 72. No through-thickness fibre angulation has been observed.

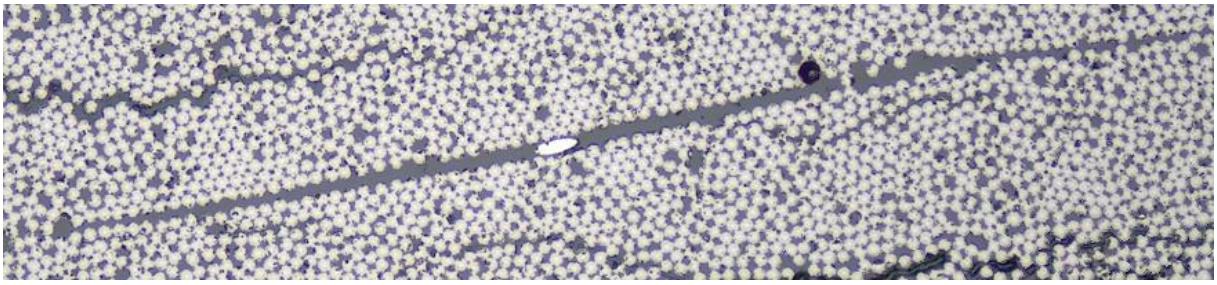

*Figure 70 P sample compressed at 100Bar imaged at 20x*

*Figure 71 width wise distribution of skewed fibres in sample C1 x50*

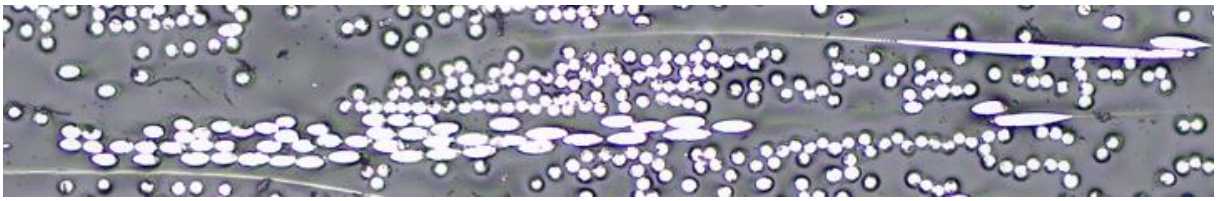

*Figure 72 width wise distribution of skewed fibres in sample L5 x20*

When analysing the micrographs, it became apparent that layer thickness impacts the packing density and thus $V_f$ of the samples.
To quantitively measure this difference, FDD through-thickness and across width measurements were compared with each other. Unfortunately, the results for these

analyses were skewed by the fact that the tape and thus cross-sections were not complete square and flat after impregnation and curing. This resulted in resin-rich areas from the micrograph frame edges being included with the analysis, resulting in low values for global $V_f$ and FDD. Therefore the absolute values from these graphs are not to be considered correct but the trend can be seen as informative on FDD. The effect of resin-rich areas on the frame edges is distinguishable in the FDD plots, as seen in Figure 73Figure 74-Figure 75, where the top, bottom and both side edges always begin with low $V_f$ values and quickly rise to the global value (straight horizontal line).

The results for FDD line plots can be improved by analysing only square sections which exclude the pure resin areas surrounding the embedded material.

The local $V_f$ plots included in appendix H do show that the higher layer count samples have higher bunching and global $V_f$, but these figures also show that the material suffers from large resin-rich areas inside the tape. Whether this is an effect of compaction pressure or material quality has to be studied.

It is hypothesized that compaction pressure does impact $V_f$ up to a certain value (~40% when reviewing comparative re-aligned rCF studies), from this point on the microstructure and homogeneity which is heavily impacted by a few skewed fibres, as expressed earlier, halts the further improvement of $V_f$.

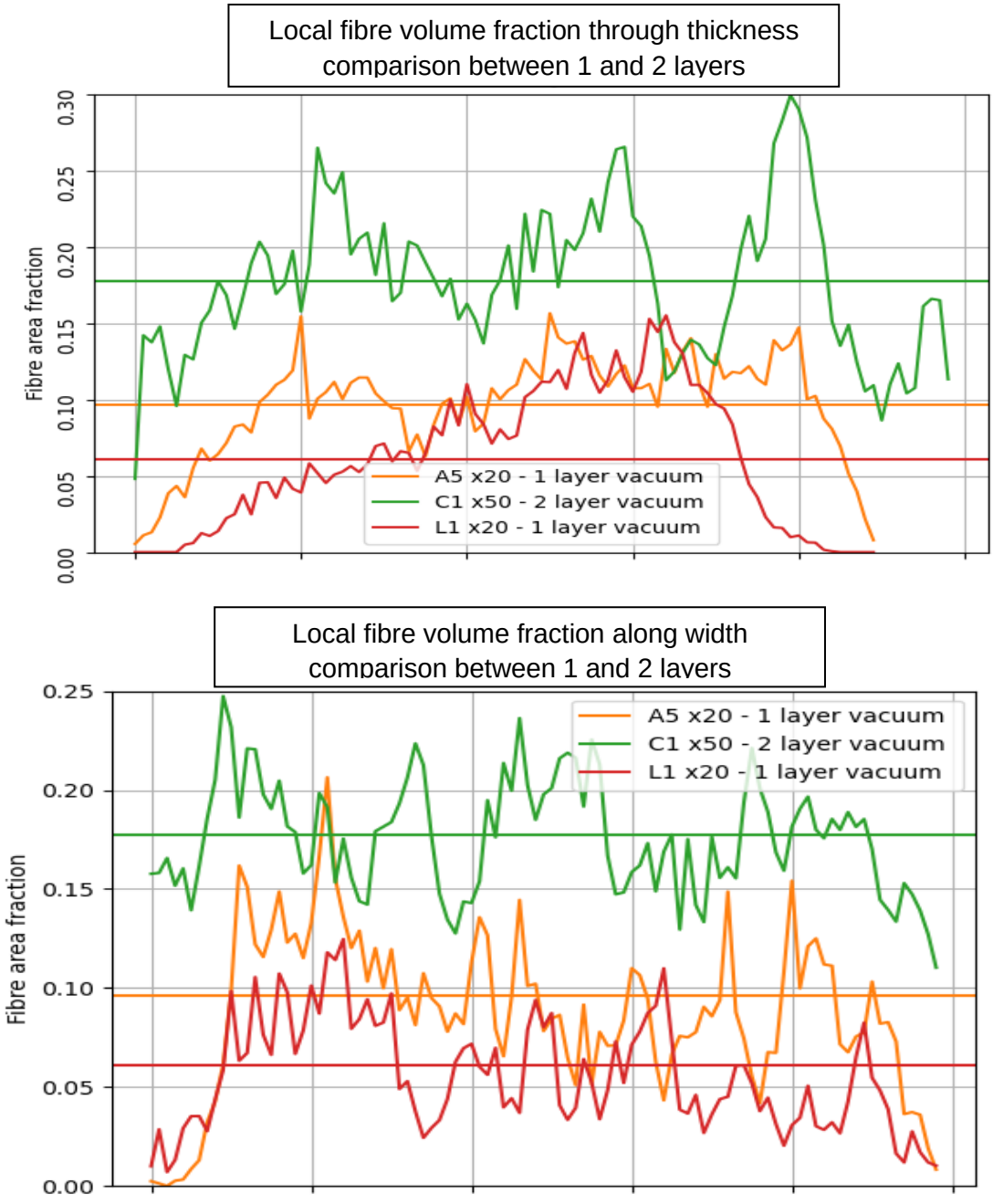
Local fibre volume fraction through thickness
comparison between 1 and 2 layers
Fibre area fraction
0.00
0.05
0.10
0.15
0.20
0.25
0.30
A5 x20 - 1 layer vacuum
C1 x50 - 2 layer vacuum
L1 x20 - 1 layer vacuum
Local fibre volume fraction along width
comparison between 1 and 2 layers
Fibre area fraction
0.00
0.05
0.10
0.15
0.20
0.25
A5 x20 - 1 layer vacuum
C1 x50 - 2 layer vacuum
L1 x20 - 1 layer vacuum

*Figure 73*

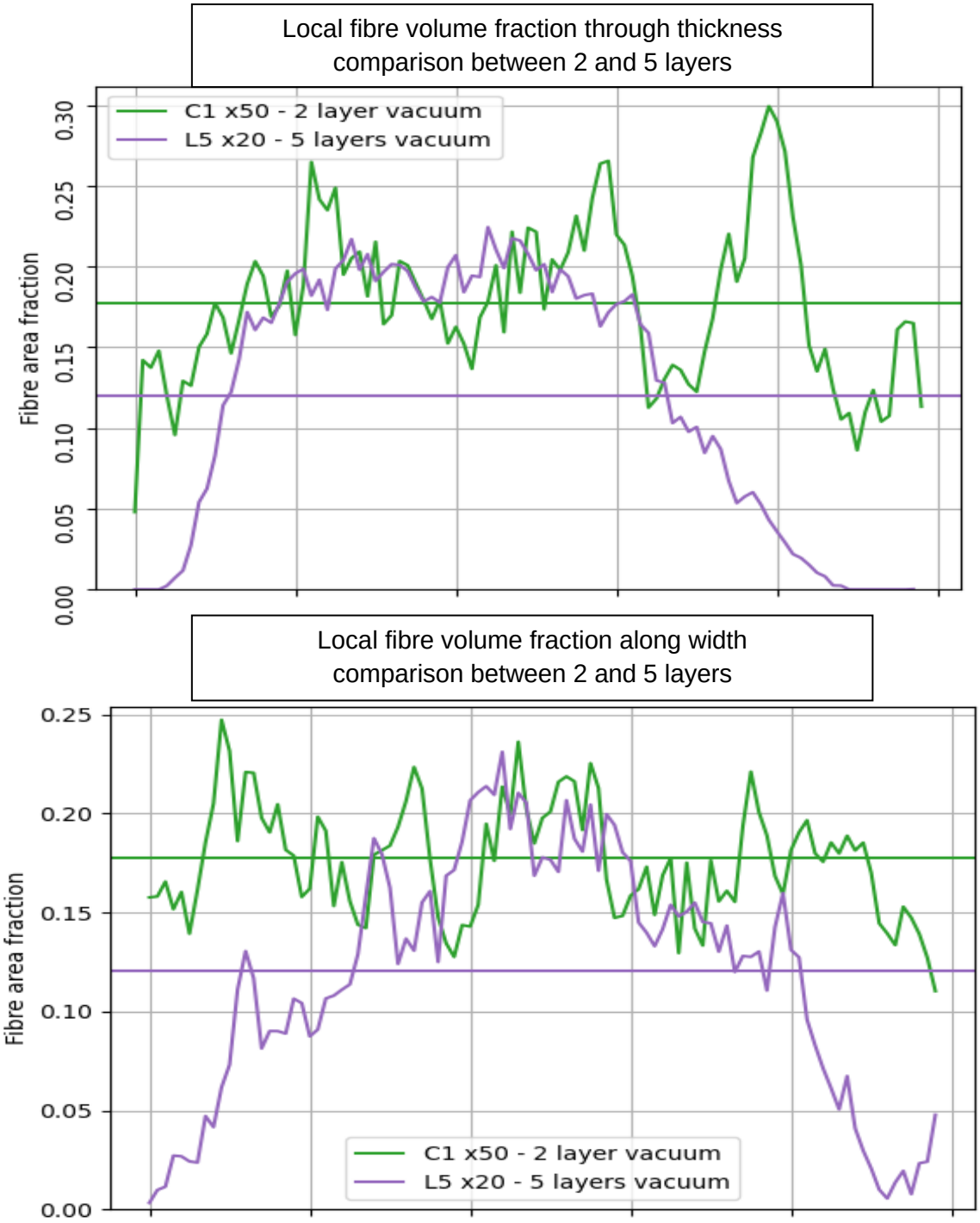
Local fibre volume fraction through thickness
comparison between 2 and 5 layers
C1 x50 - 2 layer vacuum
L5 x20 - 5 layers vacuum
Fibre area fraction
0.00
0.05
0.10
0.15
0.20
0.25
0.30
Local fibre volume fraction along width
comparison between 2 and 5 layers
Fibre area fraction
0.00
0.05
0.10
0.15
0.20
0.25
C1 x50 - 2 layer vacuum
L5 x20 - 5 layers vacuum

*Figure 74*

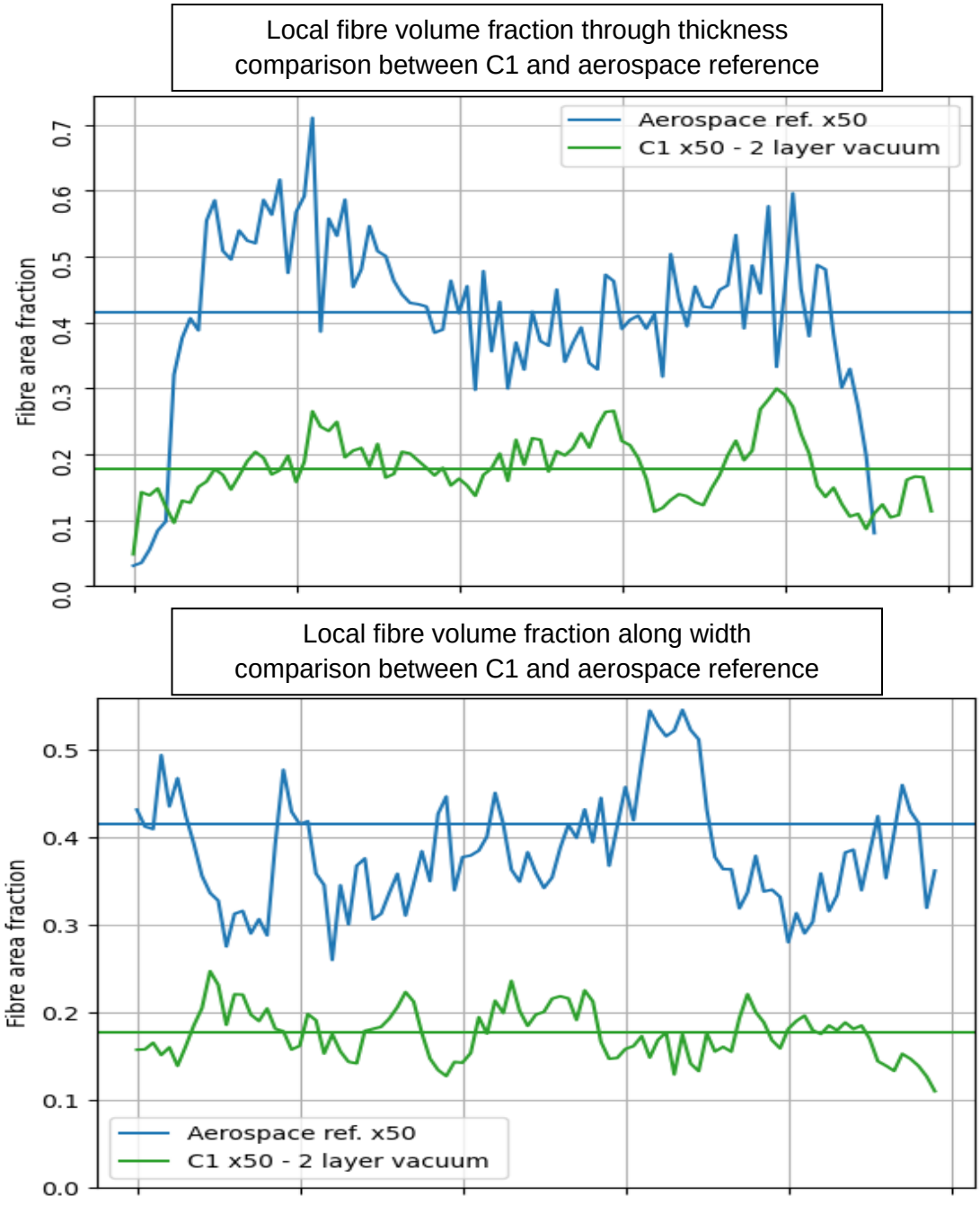
Local fibre volume fraction through thickness
comparison between C1 and aerospace reference
Aerospace ref. x50
C1 x50 - 2 layer vacuum
Fibre area fraction
0.0
0.1
0.2
0.3
0.4
0.5
0.6
0.7
Local fibre volume fraction along width
comparison between C1 and aerospace reference
Fibre area fraction
0.0
0.1
0.2
0.3
0.4
0.5
Aerospace ref. x50
C1 x50 - 2 layer vacuum

*Figure 75*

# 7. Conclusion

It was concluded from literature research that the preferred microstructure in realigned discontinuous carbon fibre composites can be characterised as having:

- Highly homogenous distributed, orientated and aligned fibres
- Fibre volume fractions greater than 50 %.
- Fibre lengths that are minimally five times longer than the critical fibre length for obtaining stiffness moduli equal to continuous carbon fibre composites. Alternatively, having a length to diameter aspect ratio close to 1000 for obtaining equal strength characteristics when compared to continuous carbon fibre composites.

The parameters which can quantitatively describe the discontinuous microstructure from a two-dimensional micrograph cross-section are in- & out-of-plane fibre orientation, global & local volume fraction and fibre-to-fibre spacing.

An initial quantitative characterisation method that can assess these microstructural parameters and therefore the quality of recycled carbon fibre materials has been developed. The method allows for the identification and measurement of fibres in 20x and 50x magnification cross-sectional optical light micrographs. The elliptical footprints left by the carbon fibres on the cross-section are identified and segmented by means of the open-source WEKA semi-supervised machine learning tool.
This WEKA segmentation tool yields a probability map that specifies the likelihood of pixels being a certain predefined class. This probability map is subsequently translated to a binary image by Otsu thresholding for further fibre measurement. The final fibre measurement is done by the MoE which extracts information on centre coordinates and elliptical shape of every fibre in the micrograph. The ellipse shape is defined by minor-major axes and in-plane angle, which together with the centre coordinates are used to quantitatively describe the material microstructure.

Measurement results show that the developed method has high accuracy in identifying and measuring fibre footprints in a micrograph cross-section. No limitation was found in the maximum number of fibres that could be identified and analysed from one cross-section. Micrographs that were taken at 20x magnification could be used for fibre identification but not fibre shape measurement, as the resolution was too low. Therefore, these scans can be used to calculate a simplified global-local fibre volume and fibre-to-fibre spacing, but no fibre orientation measurements could be performed. Micrographs that were taken at 50x magnification could be used for both fibre identification and fibre shape measurement because resolution allowed for accurate fibre shape measurements. Therefore, the developed methods preferers the higher resolution images such that fibres could be identified with high accuracy.

Results for calculating global-local fibre volume fractions, and fibre-to-fibre spacing show promising results. These descriptors can be used to compare the effect of different processing parameters on final microstructural quality.

Unfortunately, all fibre orientation measurements were flawed by the inherent susceptibility of the MoE to calculate fibre orientation with large biases. The bias was caused by the error sensitivity of the arccosines function which calculates the OoP orientation with the minor to major axes ratio.
When used to characterise the orientation of near perpendicular fibres or near-circular cross-sections, small deviations in the minor-major axes ratio will result in large nonlinear errors in the orientation.
For example, a one-pixel difference equivalent to less than 400nm in minor and major axis causes a 16° OoP angle for micrographs taken at 50x magnification. Across multiple samples with clearly distinguishable differences in surface texture and fibre orientation, the bias always centred around ±20-25°.
When verifying the method on an aerospace-grade unidirectional thermoplastic tape, with a known orientation distribution of having 95 % of its fibre within ±3° of the main axis, results by the developed method were again centred around an OoP orientation of ±20° with a standard deviation of 6.85°.
This indicates that the developed method is bound to an inherent inaccuracy caused by the arccosines function when measuring near perpendicular fibres.

# Bibliography


[1] S. Das, J. Warren, D. West, and S. M. Schexnayder, “Global Carbon Fiber Composites Supply Chain Competitiveness Analysis,” *Oak Ridge Natl. Lab.*, no. May, p. 102, 2016.

[2] J. Zhang, V. S. Chevali, H. Wang, and C. H. Wang, “Current status of carbon fibre and carbon fibre composites recycling,” *Compos. Part B Eng.*, vol. 193, no. December 2019, p. 108053, 2020.

[3] M. Kühnel and T. Kraus, “The global CFRP market 2016,” 2016.

[4] S. J. Pickering, Z. Liu, T. A. Turner, and K. H. Wong, “Applications for carbon fibre recovered from composites,” *IOP Conf. Ser. Mater. Sci. Eng.*, vol. 139, no. 1, 2016.

[5] G. Oliveux, L. O. Dandy, and G. A. Leeke, “Current status of recycling of fibre reinforced polymers: Review of technologies, reuse and resulting properties,” *Prog. Mater. Sci.*, vol. 72, pp. 61–99, 2015.

[6] S. Karuppannan Gopalraj and T. Kärki, “A review on the recycling of waste carbon fibre/glass fibre-reinforced composites: fibre recovery, properties and life-cycle analysis,” *SN Appl. Sci.*, vol. 2, no. 3, pp. 1–21, 2020.

[7] S. Job, G. Leeke, P. T. Mativenga, G. Oliveux, S. Pickering, and N. A. Shuaib, “Composites recycling : Where are we now ?,” p. 11, 2016.

[8] S. R. Naqvi, H. M. Prabhakara, E. A. Bramer, W. Dierkes, R. Akkerman, and G. Brem, “Resources , Conservation & Recycling A critical review on recycling of end-of-life carbon fi bre / glass fi bre reinforced composites waste using pyrolysis towards a circular economy,” *Resour. Conserv. Recycl.*, vol. 136, no. April, pp. 118–129, 2018.

[9] E. Pakdel, S. Kashi, R. Varley, and X. Wang, “Recent progress in recycling carbon fibre reinforced composites and dry carbon fibre wastes,” *Resour. Conserv. Recycl.*, vol. 166, no. November 2020, p. 105340, 2021.

[10] S. Pimenta and S. T. Pinho, “Recycling carbon fibre reinforced polymers for structural applications: Technology review and market outlook,” *Waste Manag.*, vol. 31, no. 2, pp. 378–392, 2011.

[11] H. Guo, “Effect of epoxy coatings on carbon fibers during manufacture of carbon fiber reinforced resin matrix composites,” *Mater. Des.*, 2010.

[12] F. C. Campbell, *Structural Composite Materials*. ASM International, 2010.

[13] N. Q. Nguyen, M. Mehdikhani, I. Straumit, L. Gorbatikh, L. Lessard, and S. V. Lomov, “Micro-CT measurement of fibre misalignment: Application to carbon/epoxy laminates manufactured in autoclave and by vacuum assisted resin transfer moulding,” *Compos. Part A Appl. Sci. Manuf.*, vol. 104, pp. 14–23, 2018.

[14] D. Grund, M. Orlishausen, and I. Taha, “Determination of fiber volume fraction of carbon fiber-reinforced polymer using thermogravimetric methods,” *Polym. Test.*, 2019.

[15] I. M. Daniel and I. Ori, *Engineering Mechanics of Composite Materials (2nd Edition)*. 2006.

[16] P. K. Mallick, *Fiber-Reinforced Composites*. CRC Press, 2007.

[17] J. Henry and S. Pimenta, “Semi-analytical simulation of aligned discontinuous composites,” 2017.

[18] A. Gillet, O. Mantaux, and G. Cazaurang, “Characterization of composite materials made from discontinuous carbon fibres within the framework of

composite recycling," *Compos. Part A Appl. Sci. Manuf.*, vol. 75, pp. 89–95, 2015.
[19] K. L. Goh, "Discontinuous-Fibre Reinforced Composites Fundamentals of Stress Transfer and Fracture Mechanics," 2017.
[20] S. Yarlagadda, J. Deitzel, D. Heider, J. Tierney, and J. W. G. Jr, "TAILORABLE UNIVERSAL FEEDSTOCK FOR FORMING ( TUFF ): OVERVIEW AND PERFORMANCE," 2019.
[21] H. Yu, K. D. Potter, and M. R. Wisnom, "A novel manufacturing method for aligned discontinuous fibre composites (High Performance-Discontinuous Fibre method)," *Compos. Part A Appl. Sci. Manuf.*, vol. 65, pp. 175–185, 2014.
[22] G. Nilakantan and S. Nutt, "Reuse and upcycling of aerospace prepreg scrap and waste," *Reinf. Plast.*, vol. 59, no. 1, pp. 44–51, 2015.
[23] E. Uhlmann and P. Meier, "Carbon Fibre Recycling from Milling Dust for the Application in Short Fibre Reinforced Thermoplastics," in *Procedia CIRP*, 2017, vol. 66, pp. 277–282.
[24] S. J. Pickering, "Recycling technologies for thermoset composite materials-current status," *Compos. Part A Appl. Sci. Manuf.*, vol. 37, no. 8, pp. 1206–1215, 2006.
[25] L. Ausheyks, "Recycling of long carbon fibers," *Kunststoffe Int.*, vol. 108, no. 5, pp. 44–48, 2018.
[26] Y. N. Kim *et al.*, "Application of supercritical water for green recycling of epoxy-based carbon fiber reinforced plastic," 2019.
[27] K. W. Kim, H. M. Lee, J. H. An, D. C. Chung, K. H. An, and B. J. Kim, "Recycling and characterization of carbon fibers from carbon fiber reinforced epoxy matrix composites by a novel super-heated-steam method," *J. Environ. Manage.*, vol. 203, pp. 872–879, 2017.
[28] S. Pimenta and S. T. Pinho, "The effect of recycling on the mechanical response of carbon fibres and their composites," *Compos. Struct.*, vol. 94, no. 12, pp. 3669–3684, 2012.
[29] F. Meng, J. McKechnie, T. A. Turner, and S. J. Pickering, "Energy and environmental assessment and reuse of fluidised bed recycled carbon fibres," *Compos. Part A Appl. Sci. Manuf.*, vol. 100, pp. 206–214, 2017.
[30] K. H. Wong, T. A. Turner, S. J. Pickering, and N. A. Warrior, "The potential for fibre alignment in the manufacture of polymer composites from recycled carbon fibre," *SAE Int. J. Aerosp.*, vol. 2, no. 1, pp. 225–231, 2010.
[31] S. Kar, S. Pattnaik, and M. K. Sutar, "Development of pseudo ductile behavior of carbon fiber reinforced composites-An overview," *Mater. Today Proc.*, vol. 18, pp. 4315–4321, 2019.
[32] J. Wellekötter, J. Resch, S. Baz, G. T. Gresser, and C. Bonten, "Insights into the Processing of Recycled Carbon Fibers via Injection Molding Compounding," *J. Compos. Sci.*, vol. 4, no. 4, p. 161, 2020.
[33] B. Xiao *et al.*, "Characterization and elastic property modeling of discontinuous carbon fiber reinforced thermoplastics prepared by a carding and stretching system using treated carbon fibers," *Compos. Part A Appl. Sci. Manuf.*, vol. 126, no. March, p. 105598, 2019.
[34] G. Yin *et al.*, "NOVEL CARDING PROCESS TO IMPROVE MECHANICAL PROPERTIES OF RECYCLED CARBON FIBER CARD WEB REINFORCED THERMOPLASTICS," *Int. Conf. Compos. Mater.*, 2017.
[35] G. M. Vélez-García, P. Wapperom, D. G. Baird, A. O. Aning, and V. Kunc, "Unambiguous orientation in short fiber composites over small sampling area in

a center-gated disk," *Compos. Part A Appl. Sci. Manuf.*, vol. 43, no. 1, pp. 104–113, 2012.
[36] J. T. Hofmann, G. M. Vélez-Garcia, D. G. Baird, and A. R. Whittington, "Application and evaluation of the method of ellipses for measuring the orientation of long, semi-flexible fibers," *Polym. Compos.*, vol. 34, no. 3, pp. 390–398, 2013.
[37] G. Régnier, D. Dray, E. Jourdain, S. Le Roux, and F. M. Schmidt, "A simplified method to determine the 3D orientation of an injection molded fiber-filled polymer," *Polym. Eng. Sci.*, vol. 48, no. 11, pp. 2159–2168, 2008.
[38] B. N. Sharma, D. Naragani, B. N. Nguyen, C. L. Tucker, and M. D. Sangid, "Uncertainty quantification of fiber orientation distribution measurements for long-fiber-reinforced thermoplastic composites," *J. Compos. Mater.*, vol. 52, no. 13, pp. 1781–1797, 2018.
[39] H. Yu, K. D. Potter, and M. R. Wisnom, "A novel manufacturing method for aligned discontinuous fibre composites (High Performance-Discontinuous Fibre method)," *Compos. Part A Appl. Sci. Manuf.*, vol. 65, pp. 175–185, Oct. 2014.
[40] D. Heider *et al.*, "CLOSED LOOP RECYCLING OF CFRP INTO HIGHLY ALIGNED HIGH PERFORMANCE SHORT FIBER COMPOSITES USING THE TUFF PROCESS."
[41] J. W. Gillespie, J. Sun, J. M. Sietins, and D. Knorr, "MICROSTRUCTURAL EVALUATION OF ALIGNED , SHORT FIBER TUFF MATERIAL."
[42] N. van de Werken, M. S. Reese, M. R. Taha, and M. Tehrani, "Investigating the effects of fiber surface treatment and alignment on mechanical properties of recycled carbon fiber composites," *Compos. Part A Appl. Sci. Manuf.*, vol. 119, no. December 2018, pp. 38–47, 2019.
[43] S. G. Advani and C. L. Tucker, "The Use of Tensors to Describe and Predict Fiber Orientation in Short Fiber Composites," *J. Rheol. (N. Y. N. Y).*, vol. 31, no. 8, pp. 751–784, 1987.
[44] Harald Cramér, *Mathematical Methods of Statistics*. Princeton University Press, 1999.
[45] C. N. E. A Clarke, C Eberhardt, "Microscopy Techniques for Materials Science Chapter III," 2000, pp. 160–225.
[46] Y. T. Zhu, W. R. Blumenthal, and T. C. Lowe, "Determination of Non-Symmetric 3-D Fiber-Orientation Distribution and Average Fiber Length in Short-Fiber Composites:," *http://dx.doi.org/10.1177/002199839703101302*, vol. 31, no. 13, pp. 1287–1301, Jul. 2016.
[47] G. M. Vélez-Garcia *et al.*, "Improvement in orientation measurement for short and long fiber injection modled composites," *Soc. Plast. Eng. - 10th Annu. Automot. Compos. Conf. Exhib. 2010, ACCE 2010*, no. January, pp. 799–809, 2010.
[48] R. S. Bay and C. L. Tucker, "Stereological measurement and error estimates for three-dimensional fiber orientation," *Polym. Eng. Sci.*, vol. 32, no. 4, pp. 240–253, Feb. 1992.
[49] I. Arganda-Carreras *et al.*, "Trainable Weka Segmentation: a machine learning tool for microscopy pixel classification," *Bioinformatics*, vol. 33, no. 15, pp. 2424–2426, Aug. 2017.
[50] N. Otsu, "THRESHOLD SELECTION METHOD FROM GRAY-LEVEL HISTOGRAMS.," *IEEE Trans Syst Man Cybern*, vol. SMC-9, no. 1, pp. 62–66, 1979.
[51] D. Legland, I. Arganda-Carreras, and P. Andrey, "MorphoLibJ: integrated library

and plugins for mathematical morphology with ImageJ," *Bioinformatics*, vol. 32, no. 22, pp. 3532–3534, Nov. 2016.
[52] F. Mesquita, Y. Swolfs, S. Bucknell, Y. Leray, S. V Lomov, and L. Gorbatikh, "TWENTY-SECOND INTERNATIONAL CONFERENCE ON COMPOSITE MATERIALS (ICCM22) TENSILE PROPERTIES OF SINGLE CARBON FIBRES TESTED WITH AUTOMATED EQUIPMENT."
[53] S. Gomarasca, D. M. J. Peeters, B. Atli-Veltin, and C. Dransfeld, "Characterising microstructural organisation in unidirectional composites," *Compos. Sci. Technol.*, vol. 215, no. August, p. 109030, 2021.
[54] P. A. O'Connell and R. A. Duckett, "Measurements of fibre orientation in short-fibre-reinforced thermoplastics," *Compos. Sci. Technol.*, vol. 42, no. 4, pp. 329–347, Jan. 1991.
[55] C. N. E. A Clarke, C Eberhardt, "Microscopy Techniques for Materials Science Chapter II," 2000.
[56] C. Eberhardt, A. Clarke, M. Vincent, T. Giroud, and S. Flouret, "Fibre-orientation measurements in short-glass-fibre composites—II," *Compos. Sci. Technol.*, vol. 61, no. 13, pp. 1961–1974, 2001.
[57] P. J. Hine, R. A. Duckett, N. Davidson, and A. R. Clarke, "Modelling of the elastic properties of fibre reinforced composites. I: Orientation measurement," *Compos. Sci. Technol.*, vol. 47, no. 1, pp. 65–73, 1993.

# Appendix

## A. Python VK4 raw image extraction

```
import numpy as np
from PIL import Image
import vk4extract #<----module has to be in the same folder as this file to run
import os

# Change directory to the folder with Keyence .vk files
os.chdir(r'C:\Users\fill\in\path\to\folder\with\all\VK4-files')
root = ('.\\')
vkimages = os.listdir(root) # Lists all the files in the folder as VKimages

#loops through vkimages to find .vk4 files and extract RGB data
for img in vkimages:
    if (img.endswith('.vk4')):
        with open(img, 'rb') as in_file:
            offsets = vk4extract.extract_offsets(in_file)
            rgb_dict = vk4extract.extract_color_data(offsets, 'peak', in_file)  # use
extract_img_data for light and height data

            rgb_data = rgb_dict['data']
            height = rgb_dict['height']
            width = rgb_dict['width']
            rgb_matrix = np.reshape(rgb_data, (height, width, 3))
            image = Image.fromarray(rgb_matrix, 'RGB')      # extract raw RGB images

            image.save(img.replace('.vk4', '.png'), 'PNG')    # saves the images as PNG in same
folder as root
```

## B. Python module VK4 raw image extraction

```
"""
vk4extract
Original authors
Wylie Gunn & Behzad Torkian
"""
import logging
import struct
import numpy as np
# import readbinary as rb

log = logging.getLogger('vk4_driver.vk4extract')

# extract offsets for data sections of vk4 file
def extract_offsets(in_file):
    """extract_offsets
    Extract offset values from the offset table of a vk4 file. Stores offsets
    and returns values in dictionary
    :param in_file: open file obj, must be vk4 file
    """
    log.debug("Entering extract_offsets()")

    offsets = dict()
    in_file.seek(12)
    offsets['meas_conds'] = struct.unpack('<I', in_file.read(4))[0]
    offsets['color_peak'] = struct.unpack('<I', in_file.read(4))[0]
    offsets['color_light'] = struct.unpack('<I', in_file.read(4))[0]
    offsets['light'] = struct.unpack('<I', in_file.read(4))[0]
```

```
    in_file.seek(8, 1)
    offsets['height'] = struct.unpack('<I', in_file.read(4))[0]
    in_file.seek(8, 1)
    offsets['clr_peak_thumb'] = struct.unpack('<I', in_file.read(4))[0]
    offsets['clr_thumb'] = struct.unpack('<I', in_file.read(4))[0]
    offsets['light_thumb'] = struct.unpack('<I', in_file.read(4))[0]
    offsets['height_thumb'] = struct.unpack('<I', in_file.read(4))[0]
    offsets['assembly_info'] = struct.unpack('<I', in_file.read(4))[0]
    offsets['line_measure'] = struct.unpack('<I', in_file.read(4))[0]
    offsets['line_thickness'] = struct.unpack('<I', in_file.read(4))[0]
    offsets['string_data'] = struct.unpack('<I', in_file.read(4))[0]
    # not sure if reserved is necessary
    offsets['reserved'] = struct.unpack('<I', in_file.read(4))[0]

    log.debug("Exiting extract_offsets()")
    return offsets

# color peak and color + light data extracted with extract_color_data
def extract_color_data(offset_dict, color_type, in_file):
    """extract_color_data
    Extracts RGB metadata and raw image data from a vk4 file. Stores data and
    returns as dictionary
    :param offset_dict: dictionary - offset values in vk4
    :param color_type: string - type of data, must be 'peak' or 'light'
    :param in_file: open file obj, must be vk4 file
    """
    log.debug("Entering extract_color_data()")
    rgb_types = {'peak': 'color_peak', 'light': 'color_light'}
    rgb_color_data = dict()
    rgb_color_data['name'] = 'RGB ' + color_type
    in_file.seek(offset_dict[rgb_types[color_type]])
    rgb_color_data['width'] = struct.unpack('<I', in_file.read(4))[0]
    rgb_color_data['height'] = struct.unpack('<I', in_file.read(4))[0]
    rgb_color_data['bit_depth'] = struct.unpack('<I', in_file.read(4))[0]
    rgb_color_data['compression'] = struct.unpack('<I', in_file.read(4))[0]
    rgb_color_data['data_byte_size'] = struct.unpack('<I', in_file.read(4))[0]
    rgb_color_arr = np.zeros(((rgb_color_data['width'] * rgb_color_data['height']),
                              (rgb_color_data['bit_depth'] // 8)), dtype=np.uint8)

    i = 0
    for val in range(rgb_color_data['width'] * rgb_color_data['height']):
        rgb = []
        for channel in range(3):
            rgb.append(ord(in_file.read(1)))
        rgb_color_arr[i] = rgb
        i = i + 1

    rgb_color_data['data'] = rgb_color_arr
    log.debug("Exiting extract_color_data()")
    return rgb_color_data
```

# C. ImageJ Tiling WEKA segmentation macro

Plugin Trainable_Segmentation-3.2.34 was used with this macro.

```
// @File(label="Input directory", description="Select the directory with input
images", style="directory") inputDir
// @File(label="Output directory", description="Select the output directory",
style="directory") outputDir
// @File(label="Weka model", description="Select the Weka model to apply")
modelPath
// @String(label="Result mode",choices={"Labels","Probabilities"}) resultMode
// @Integer(label="Number of tiles in X:", description="Number of image subdivision
in the X direction", value=3) xTiles
// @Integer(label="Number of tiles in Y:", description="Number of image subdivision
in the Y direction", value=3) yTiles
// @Integer(label="Number of tiles in Z (if 3D):", description="Number of image
subdivision in the Z direction (ignored when using 2D images)", value=3) zTiles

import trainableSegmentation.WekaSegmentation;
import trainableSegmentation.utils.Utils;
import ij.io.FileSaver;
import ij.IJ;
import ij.ImagePlus;

// starting time
startTime = System.currentTimeMillis();

// caculate probabilities?
getProbs = resultMode.equals( "Probabilities" );

// create segmentator
segmentator = new WekaSegmentation( zTiles > 0 );
// load classifier
segmentator.loadClassifier( modelPath.getCanonicalPath() );

// get list of input images
listOfFiles = inputDir.listFiles();
for ( i = 0; i < listOfFiles.length; i++ )
{
    // process only files (do not go into sub-folders)
    if( listOfFiles[ i ].isFile() )
    {
        // try to read file as image
        image = IJ.openImage( listOfFiles[i].getCanonicalPath() );
        if( image != null )
        {
         tilesPerDim = new int[ 2 ];
         if( image.getNSlices() > 1 )
         {
                 tilesPerDim = new int[ 3 ];
                 tilesPerDim[ 2 ] = zTiles;
         }
         tilesPerDim[ 0 ] = xTiles;
         tilesPerDim[ 1 ] = yTiles;
```

```
            // apply classifier and get results (0 indicates number of threads is
auto-detected)
            result = segmentator.applyClassifier( image, tilesPerDim, 0, getProbs
);

                        if( !getProbs )
                // assign same LUT as in GUI
                result.setLut( Utils.getGoldenAngleLUT() );

            // save result as TIFF in output folder
            outputFileName = listOfFiles[ i ].getName().replaceFirst("[.][^.]+$",
"") + ".tif";
            new FileSaver( result ).saveAsTiff( outputDir.getPath() +
File.separator + outputFileName );

            // force garbage collection (important for large images)
            result = null;
            image = null;
            System.gc();
        }
    }
}
// print elapsed time
estimatedTime = System.currentTimeMillis() - startTime;
IJ.log( "** Finished processing folder in " + estimatedTime + " ms **" );
System.gc();
```

## D.ImageJ probability map to ellipses macro

```
// Input file for this macro should be a Tiff. propability map image
// The first image in that propability map should be a fibres specific one
// This images is preferably produced by the script
tiling_segmenting_combining_script.bhs
// The aforementioned script is run with the Weka segmentation V3.1 model

// duplicates and selects the "Fibres" image of the tiff stack
run("Duplicate...", "use");
//selectWindow("Fibre");

// applies Otsu thresholding on fibres
setAutoThreshold("Otsu dark");
setOption("BlackBackground", false);
run("Convert to Mask");
run("Despeckle");
run("Watershed");

// analyses the particles and draws best fitting ellipses
// minimum size for particle analysis is 85  % surface area of fibre at zero
degrees -> surface area of a circle 0.85*pi*r^2
// maximum size for particle analysis is fibres at an anlge of 60degrees result in
minor/major fraction of cos(70)=0,34 -> surface area of ellipse
pi*(0.5*minor)*(0.5*major)
```

```
//run("Analyze Particles...", "size=1590-Infinity circularity=0.2-1.00
show=Ellipses display exclude");  // when analysing 50x mag 200  % size increased
// run("Analyze Particles...", "size=430-1435 circularity=0.2-1.00 show=Ellipses
display exclude");     // when analysing 50x origional image
run("Analyze Particles...", "size=66-230 circularity=0.2-1.00 show=Ellipses display
exclude");     // when analysing 20x origional image
```

## E. ImageJ draw minor-major axes ellipses macro

```
// this macro is for drawing ellipses and minor-major axes
// input for this macro can be a probability map with white fibres on black
background
//               or binary image with black fibres on white background

run("Duplicate...", "use");

//setAutoThreshold;
run("Set Measurements...", " area mean centroid fit ");
run("Auto Threshold", "method=Otsu white");
run("Convert to Mask");
run("Despeckle");
run("Watershed");

// set particle analyser to correct setting. i.e. resolution
run("Analyze Particles...", "size=200-Infinity circularity=0.20-1.00 display
show=Ellipses display exclude clear ");

run("RGB Color");

for(i=0; i<nResults; i++)
        {
        x=getResult('X',i);
        y=getResult('Y',i);
        d=getResult('Major',i);
        a = getResult('Angle',i)*PI/180;
        setColor("blue");
        drawLine(x+(d/2)*cos(a), y-(d/2)*sin(a), x-(d/2)*cos(a), y+(d/2)*sin(a));
        d=getResult('Minor',i);
        a=a+PI/2;
        setColor("red");
        drawLine(x+(d/2)*cos(a), y-(d/2)*sin(a), x-(d/2)*cos(a), y+(d/2)*sin(a));
        }
```

# F. Python code to process data from MoE csv data

```
import pandas as pd
import numpy as np
import seaborn as sns
import matplotlib.pyplot as plt
from matplotlib.offsetbox import AnchoredText

# ============================================================================
#  reads csv file and creates new column "out-of plane"
# ============================================================================
"""

"""

raw_data = pd.read_csv(r'C:\Users\jespe\surfdrive\Thesis\Weka\Silvia\processing\200
%\Results.csv', usecols=['X','Y','Major','Minor'])

raw_data["Out-of plane angle"] = np.degrees(np.arccos(raw_data['Minor'] /
raw_data['Major']))
raw_data["Area"] = np.pi*(0.5*raw_data['Minor'])*(0.5*raw_data['Major'])
data = raw_data.to_numpy()

"""
set resolution of image for further analysis
resolution 20x mag 1.452 pixels = 1 micron
resolution 50x original 3.63 pixels = 1 micron
resolution 50x 200  % highres 7.26 pixels = 1 micron
"""
sample_name = "Aerospace ref. x50 200  % high res"
resolution = 7.26

#%  %
# ============================================================================
# histograms fibre orientation
# ============================================================================
"""
"""
bins = np.linspace(0, 90, 90)
sns.set_style('darkgrid')
ax = sns.distplot(data[:,4], bins=bins)

ax.set_xticks(range(0,95,5))
ax.set_title('Histogram: Out of plane Thèta [degree] \n '+str(sample_name))
ax.set_xlabel("Angle [degrees]")

x = data[:,4]
ax = sns.kdeplot(x, fill=False, color='crimson')

kdeline = ax.lines[0]
xs = kdeline.get_xdata()
ys = kdeline.get_ydata()
middle = x.mean()
sdev = x.std()
left = middle - sdev
```

```
right = middle + sdev
ax.set_title('Histogram: Out of plane Thèta [degree] \n '+str(sample_name))
ax.set_xlabel("Angle [degrees]")

anc = AnchoredText(r"$mean = {}, std= {}$".format(round(middle,2),round(sdev,2)),
loc="upper right")
ax.add_artist(anc)
ax.vlines(middle, 0, np.interp(middle, xs, ys), color='crimson', ls=':')
ax.fill_between(xs, 0, ys, alpha=0.2)
ax.fill_between(xs, 0, ys, where=(left <= xs) & (xs <= right), interpolate=True,
facecolor='crimson', alpha=0.5)

#%  %
# ============================================================================
# histograms length minor axis
# ============================================================================
"""
"""
x_minor_min = 5
x_minor_max = 9
bins = np.linspace(x_minor_min, x_minor_max, 100)
ax = sns.distplot(data[:,3]/resolution, bins=bins, kde=True)

ax.set_xticks(range(x_minor_min,x_minor_max,1))
ax.set_title('Histogram: length minor axis \n ' +str(sample_name))
ax.set_xlabel("length [micrometer]")
# ax.set_xticks(range(6,31,1))
ax.set_xlim([x_minor_min, x_minor_max])

mean = (data[:,3].mean())/resolution
std = (data[:,3].std())/resolution
anc = AnchoredText(r"$mean = {} µm, std= {}µm$".format(round(mean,2),round(std,2)),
loc="upper left")
ax.add_artist(anc)

#%  %
# ============================================================================
# histograms minor and major axis
# ============================================================================
"""
"""
x_minor_min = 19        # needs to dubble when working with 200  % rez
x_minor_max = 31
mean_minor = (data[:,3].mean())
bins = np.linspace(x_minor_min, x_minor_max, 100)
ax = sns.distplot(data[:,3], bins=bins,label='minor axis', kde=True)
ax.set_xticks(range(x_minor_min,x_minor_max,1))

x_major_min = 19
x_major_max = 40
mean_major = (data[:,2].mean())
bins = np.linspace(x_major_min, x_major_max, 100)

ax = sns.distplot(data[:,2], bins=bins, label='major axis', kde=True)
ax.set_xticks(range(x_major_min,x_major_max,1))
```

```
ax.set_title('Histogram: minor & major axis \n ' +str(sample_name))
ax.set_xlabel("length [Pixels]")
ax.set_xlim([x_major_min, x_major_max])

anc = AnchoredText(r"$minor = {}, major =
{}$".format(round(mean_minor,2),round(mean_major,2)), loc="upper left")
ax.add_artist(anc)
ax.legend()

ax.set_xlim([x_minor_min, x_major_max])

#%  %
# ================================================================================
# Fibre point distribution and histogram of X & Y axis plot
# ================================================================================
sns.jointplot(x=data[:,0], y=(-1*data[:,1]))
plt.show()

#%  %
# ================================================================================
# calculate global volume fraction
# ================================================================================
"""
"""
tot_area_ellipse = raw_data['Area'].sum()

x_grid_length = raw_data['X'].max()-raw_data['X'].min()
y_grid_length = raw_data['Y'].max()-raw_data['Y'].min()

tot_area = x_grid_length*y_grid_length

global_vol_frac = tot_area_ellipse / tot_area

#% %
# ================================================================================
# Calculate local volume fraction + line plot
# ================================================================================
"""
resolutie 20x mag 1.452 pixels = 1 micron
resolutie 50x original 3.63 pixels = 1 micron
reolustie 50x highres 7.26 pixels = 1 micron

resolution 20x mag is too low to accuratly measure minor-major axis thus surface
area is useless
instead for every x-y coordinate a average fibre diameter (fibre_dia) is used to
calculate fibre surface and with this local vf
"""
    # use when analysing with 20x magnification
# fibre_dia_micron = 6.8 # micron    average dia from 50x measurements
# fibre_dia_pix = fibre_dia_micron * resolution # pixels
# raw_data["Area"] = np.pi*(fibre_dia_pix**2/4)  # surface area of the fibre in
pixels

    # step size of bin 1 % of complete width or height
# x_step_size = raw_data['X'].max()*0.01
```

```
# y_step_size = raw_data['Y'].max()*0.01

    # square bin size
# x_step_size = y_step_size = 40 # [ 40  x 40 pixels] for 20X mag
# x_step_size = y_step_size = 100 # [ 100  x 100 pixels] for origional 50X mag
x_step_size = y_step_size = 200     # [ 200  x 200 pixels] for highrez 200 % 50X
mag

    # local vf along X width
plt.figure(1)
df_x_area = raw_data.groupby(pd.cut(raw_data['X'],
bins=np.arange(raw_data['X'].min(),

round((raw_data['X'].max()), -1),

x_step_size)))['Area'].agg(['sum'])
df_x_area = df_x_area['sum']/(x_step_size*raw_data['Y'].max())
ax = df_x_area.plot(ylabel='Fibre area fraction', grid=True,
                    title= 'Local fibre volume fraction along width  \n
'+str(sample_name), label= str(sample_name))

plt.ylim(0, )  #
plt.xticks(color='w')
ax.legend()

# a=ax.get_xticks().tolist()
# a = ['', '-X', '-2/3X' , '-1/3X', '+1/3X', '+2/3X', '+X', 'xx','xxx', '+X' ]
# ax.set_xticklabels(a)

    # local vf along y thickness
plt.figure(2)
df_y_area = raw_data.groupby(pd.cut(raw_data['Y'],
bins=np.arange(raw_data['Y'].min(),

round((raw_data['Y'].max()), -1),

y_step_size)))['Area'].agg(['sum'])
df_y_area = df_y_area['sum']/(y_step_size*raw_data['X'].max())
ax = df_y_area.plot(ylabel='Fibre area fraction', grid=True,rot=90,
                    title= 'Local fibre volume fraction through thickness \n
'+str(sample_name),
                    label=str(sample_name))

plt.ylim(0,)
plt.xticks(color='w')
plt.yticks(rotation=90)
ax.legend()

# b= ax.get_xticks().tolist()
# b = ['', '+Y', '+2/3Y' , '+1/3Y', '-1/3Y', '-2/3Y', '-Y','']
# ax.set_xticklabels(b)

#% %
# ========================================================================
# Plot local volume fraction
```

```
# ============================================================================
"""
resolutie 20x mag 1.452 pixels = 1 micron
resolutie 50x original 3.63 pixels = 1 micron
reolustie 50x highres 7.26 pixels = 1 micron

resolution 20x mag is too low to accuratly measure minor-major axis thus surface
area is useless
instead for every x-y coordinate a average fibre diameter (fibre_dia) is used to
calculate fibre surface and with this local vf
"""

# fibre_dia_micron = 6.8 # micron    average dia from 50x measurements
# fibre_dia_pix = fibre_dia_micron * resolution # pixels  (9.8736)
# raw_data["Area"] = np.pi*(fibre_dia_pix**2/4)  # surface area of the fibre in
pixels

    # square bin size
# x_step_size = y_step_size = x_length_grid = y_length_grid = 40 # [ 100  x 100
pixels] for 20X mag
# x_step_size = y_step_size = x_length_grid = y_length_grid = 100     # [ 100  x
100 pixels] for origional 50X mag
x_step_size = y_step_size = x_length_grid = y_length_grid = 200     # [ 200  x 200
pixels] for highrez 200 % 50X mag

# step size [pixels] of bin 1 % of complete width or height
# x_step_size = raw_data['X'].max()*0.01
# y_step_size = raw_data['Y'].max()*0.01
# x_length = (raw_data['X'].max() - raw_data['X'].min())
# y_length = (raw_data['Y'].max() - raw_data['Y'].min())
# x_length_grid = x_length/x_step_size
# y_length_grid = y_length/y_step_size

surface_area_grid =int(x_length_grid*y_length_grid)

plt.hist2d(raw_data['X'], raw_data['Y'], weights =
raw_data['Area']/surface_area_grid,
           bins= [np.arange(0,round((raw_data['X'].max()),-1)+x_step_size,
x_step_size),
                  np.arange(0,round((raw_data['Y'].max()),-1)+y_step_size,
y_step_size)])

plt.xlim(min(raw_data['X']),max(raw_data['X']))
plt.ylim(max(raw_data['Y']),min(raw_data['Y']))  # flip y-axis

plt.title("Local fibre volume fraction")
plt.xlabel("width [pixels]")
plt.ylabel("Height [pixels]")

# grabs current axis (GCA) and sets aspect ratio to equal
axes=plt.gca()
axes.set_aspect("equal")

## add colorbar horizontally underneath the x-axis
cb = plt.colorbar(orientation = 'horizontal')
```

```
cb.set_label('Local fibre volume fraction per bin')

# axes.xaxis.set_visible(False)
# axes.yaxis.set_visible(False)
# axes.title.set_visible(False)
#% %
# ========================================================================
# heatmap of distribution  !!!!SLOW!!!!!
# ========================================================================
ax = sns.kdeplot(x=data[:,0], y=(-1*data[:,1]), cmap="Reds", shade=True,
bw_adjust=0.20)
ax.set_title('Fibre distribution density map')

#% %
# ========================================================================
# calculate four nearest neighbours and their distance to one another
# ========================================================================
"""
"""
from scipy.spatial import KDTree

xy = data[:,:2] # select the X and Y colums
kdtree = KDTree(xy)


nearest_distance =[]
for i in range(len(xy)):
    d, i = kdtree.query((xy[i]),k=5)  # k=5 for the 4 nearest neighbours because we
ignore it self
    nearest_distance.append(d[1:])  # ignore itself as nearest neighbour#  % %

distance_first_nearest_neighbours     = []
distance_second_nearest_neighbours    = []
distance_third_nearest_neighbours     = []
distance_fourth_nearest_neighbours    = []
for i in range(len(nearest_distance)):
    distance_first_nearest_neighbours.append(nearest_distance[i][0])
    distance_second_nearest_neighbours.append(nearest_distance[i][1])
    distance_third_nearest_neighbours.append(nearest_distance[i][2])
    distance_fourth_nearest_neighbours.append(nearest_distance[i][3])

    ## chance scale size/pixels when using origional resolution image
distance_first_nearest_neighbours_micrometre =
np.array(distance_first_nearest_neighbours)/resolution
distance_second_nearest_neighbours_micrometre =
np.array(distance_second_nearest_neighbours)/resolution
distance_third_nearest_neighbours_micrometre =
np.array(distance_third_nearest_neighbours)/resolution
distance_fourth_nearest_neighbours_micrometre =
np.array(distance_fourth_nearest_neighbours)/resolution

# plots the first, second and third nearest neighbours in a CDF histogram
ax = sns.kdeplot(distance_first_nearest_neighbours_micrometre, cumulative=True,
label='First neighbours')
```

```
ax = sns.kdeplot(distance_second_nearest_neighbours_micrometre, cumulative=True,
label='Second neighbours')
ax = sns.kdeplot(distance_third_nearest_neighbours_micrometre, cumulative=True,
label='Third neighbours')
ax = sns.kdeplot(distance_fourth_nearest_neighbours_micrometre, cumulative=True,
label='Fourth neighbours')
ax.set_title('Cumulative density function nearest neigbours \n '+str(sample_name))
ax.set_xlabel("distance [micrometre]")      #  when scale is known
# ax.set_xlabel("distance [pixels]")           #  when scale is unknown
mean = (data[:,3].mean())/resolution      # mean fibre diameter
plt.vlines(x=[(1*mean),(np.sqrt(3)*mean),(2*mean),(np.sqrt(7)*mean)],ymin=0,ymax=1,
label='theoretical nearest neighbour distance', linestyles='dotted')

ax.set_xticks(range(6,31,1))
ax.set_xlim([5, 30])

anc = AnchoredText(r"$Fibre diameter = {} µm$".format(round(mean,2)), loc="right")
ax.add_artist(anc)

ax.legend()
```

## G. Orientation tensor python code

```
#% %
# ================================================================================
# average distribution of A11-A22 through thickness per pixel bin
# ================================================================================

df_OoP = raw_data.groupby(pd.cut(raw_data['Y'],
bins=np.arange(raw_data['Y'].min(),raw_data['Y'].max(),raw_data['Y'].max()/100)))['
Out-of plane angle'].agg(['mean','median','std'])
df_A11 = raw_data.groupby(pd.cut(raw_data['Y'],
bins=np.arange(raw_data['Y'].min(),raw_data['Y'].max(),raw_data['Y'].max()/100)))['
A11'].agg(['mean','std'])    # 'std', 'size'
df_A22 = raw_data.groupby(pd.cut(raw_data['Y'],
bins=np.arange(raw_data['Y'].min(),raw_data['Y'].max(),raw_data['Y'].max()/100)))['
A22'].agg(['mean','std'])
df_OoP.plot(ylabel='degrees out of plane', title= "out of plane angle [Degrees] \n
through thickness "+str(sample_name))
plt.ylim(0,)
df_A11.plot(ylabel='average value of bin ', title= "A11 \n through thickness
"+str(sample_name))
plt.ylim(0,0.5)
df_A22.plot(ylabel='average value of bin ', title= "A22 \n through thickness
"+str(sample_name))
plt.ylim(0,0.5)

#% %
# ================================================================================
# average distribution of A11-A22 across width per pixel bin
# ================================================================================

df_OoP = raw_data.groupby(pd.cut(raw_data['X'], bins=np.arange(0,round(len(data),-
2),raw_data['X'].max()/100)))['Out-of plane angle'].agg(['mean','median','std'])
```

```
df_A11 = raw_data.groupby(pd.cut(raw_data['X'], bins=np.arange(0,round(len(data),-
2),raw_data['X'].max()/100)))['A11'].agg(['mean','std'])    # 'std', 'size'
df_A22 = raw_data.groupby(pd.cut(raw_data['X'], bins=np.arange(0,round(len(data),-
2),raw_data['X'].max()/100)))['A22'].agg(['mean','std'])
df_OoP.plot(ylabel='degrees out of plane', title= "out of plane angle [Degrees]  \n
across width "+str(sample_name))
plt.ylim(0,)
df_A11.plot(ylabel='average value of bin ', title= "A11 \n across width
"+str(sample_name))
plt.ylim(0,0.5)
df_A22.plot(ylabel='average value of bin ', title= "A22 \n across width
"+str(sample_name))
plt.ylim(0,0.5)
```

## H.Images of FDD in landscape mode

A5 x20

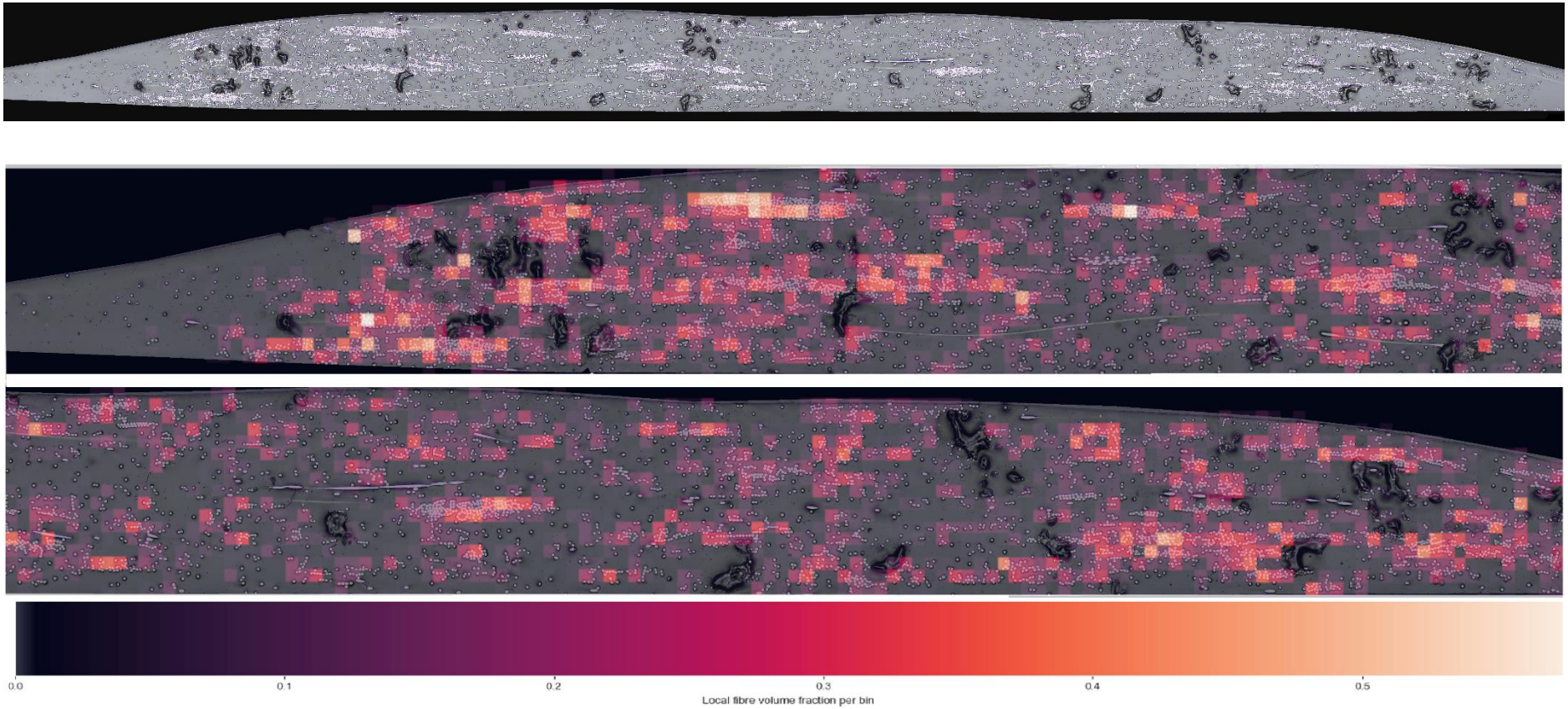

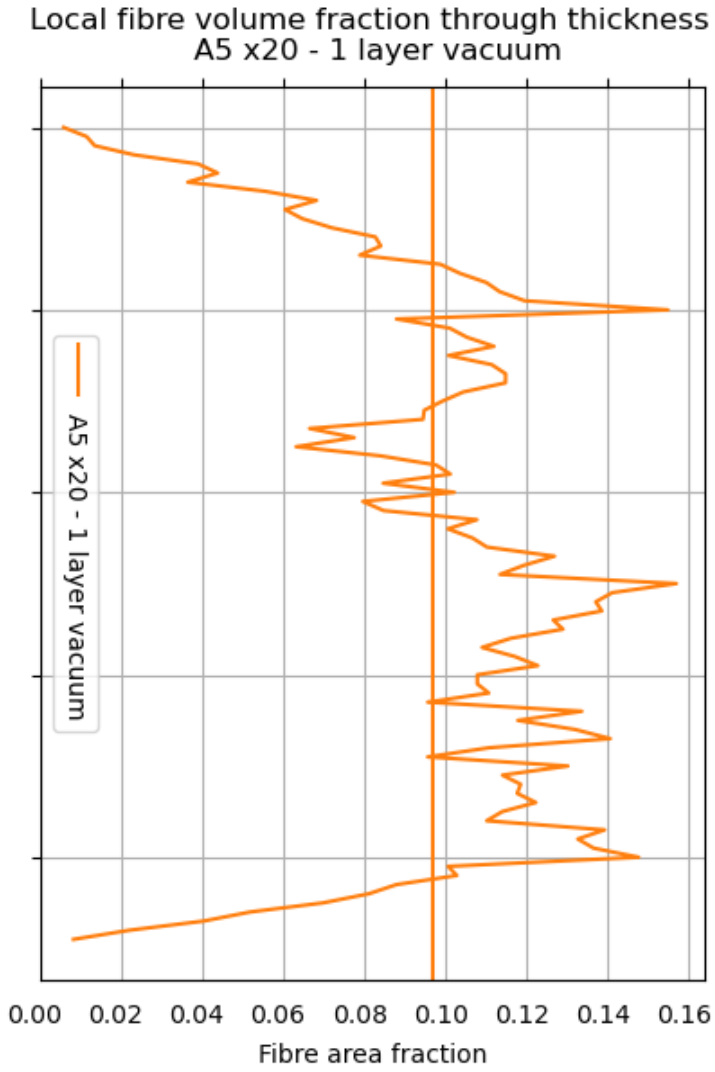
Local fibre volume fraction through thickness
A5 x20 - 1 layer vacuum
A5 x20 - 1 layer vacuum
0.00
0.02
0.04
0.06
0.08
0.10
0.12
0.14
0.16
Fibre area fraction

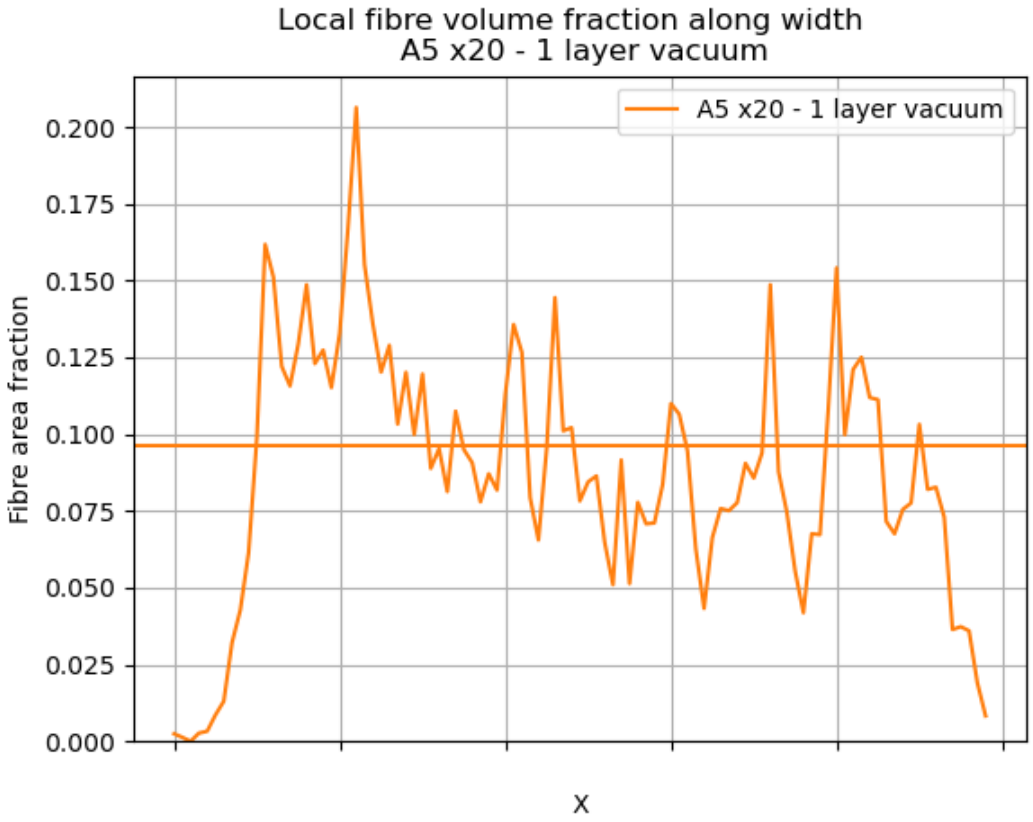
Local fibre volume fraction along width
A5 x20 - 1 layer vacuum
A5 x20 - 1 layer vacuum
0.200
0.175
0.150
0.125
0.100
0.075
0.050
0.025
0.000
Fibre area fraction
X

## C1 x50

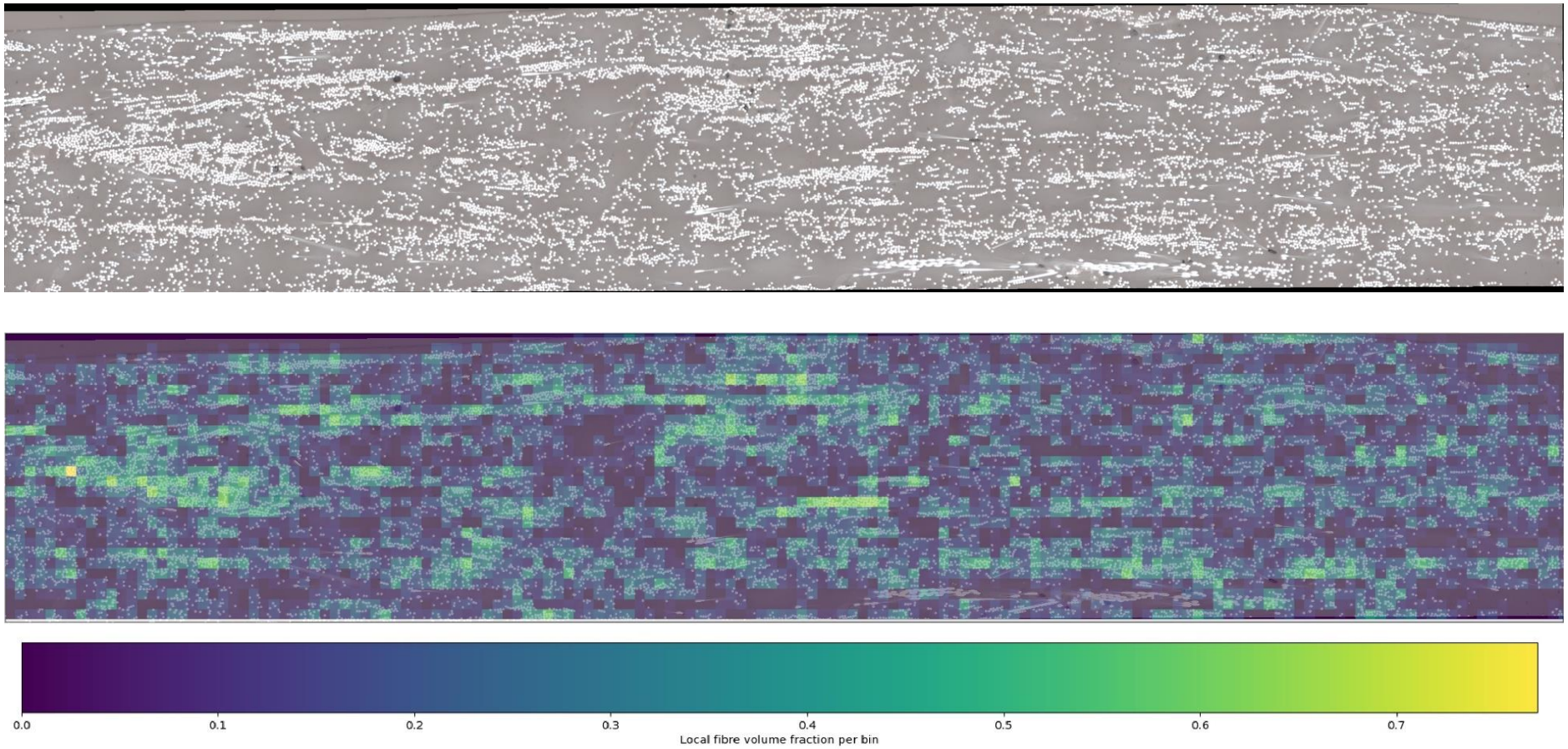

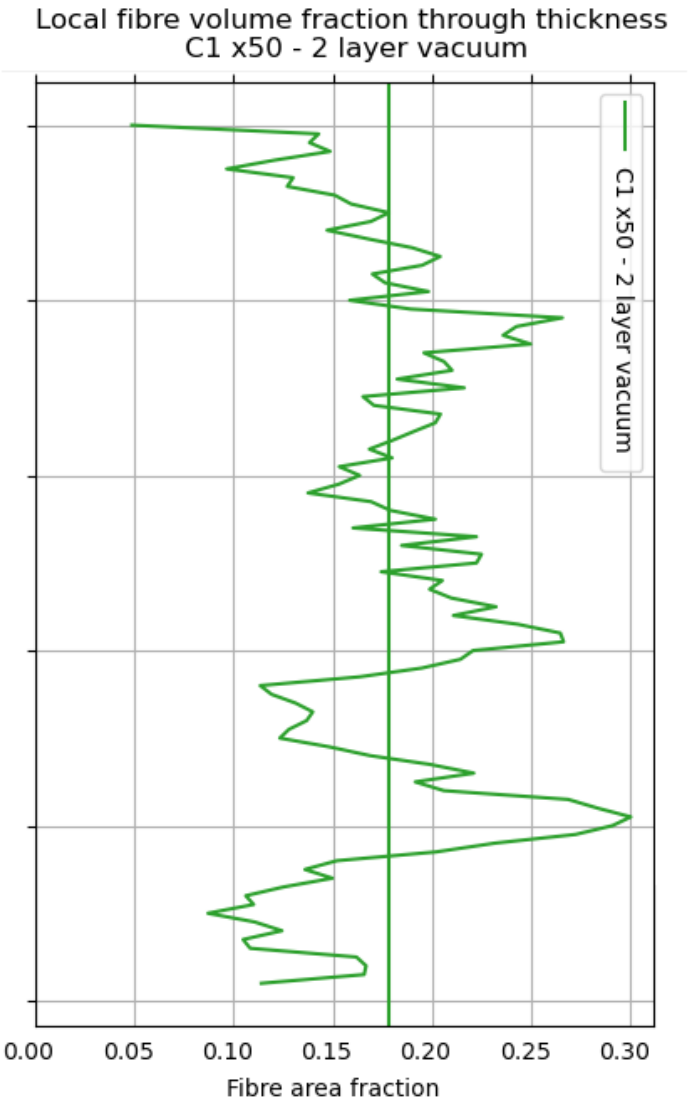
Local fibre volume fraction through thickness
C1 x50 - 2 layer vacuum
C1 x50 - 2 layer vacuum
0.00
0.05
0.10
0.15
0.20
0.25
0.30
Fibre area fraction

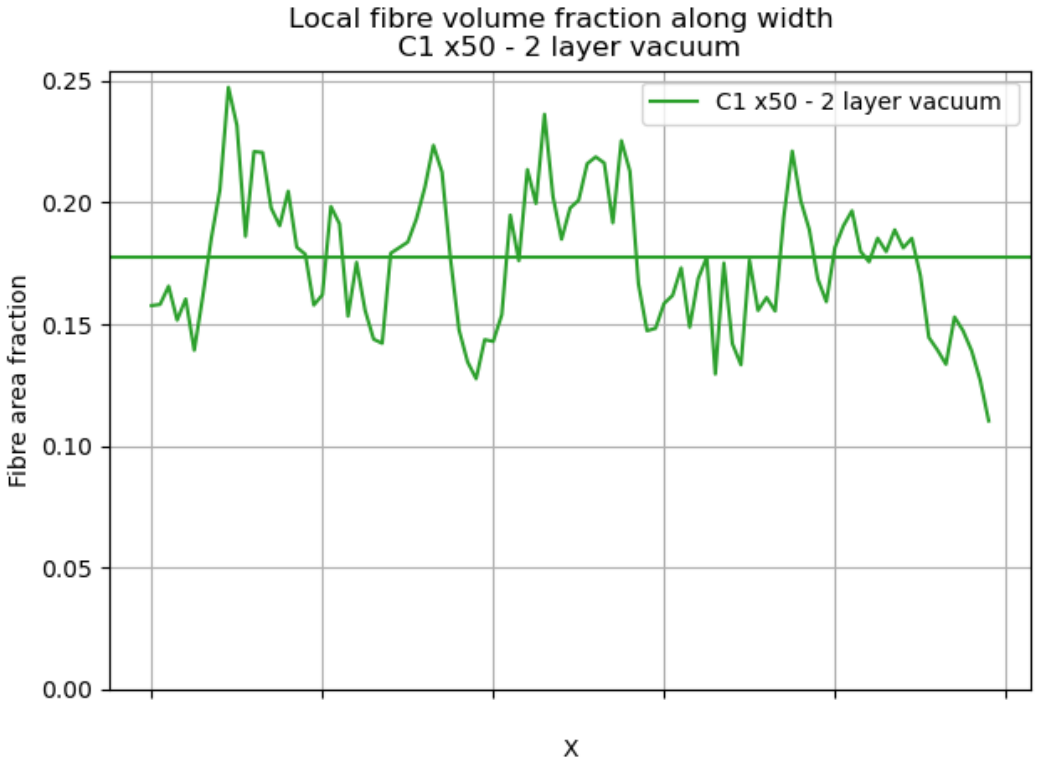
Local fibre volume fraction along width
C1 x50 - 2 layer vacuum
C1 x50 - 2 layer vacuum
0.25
0.20
0.15
0.10
0.05
0.00
Fibre area fraction
X

# L1 x20

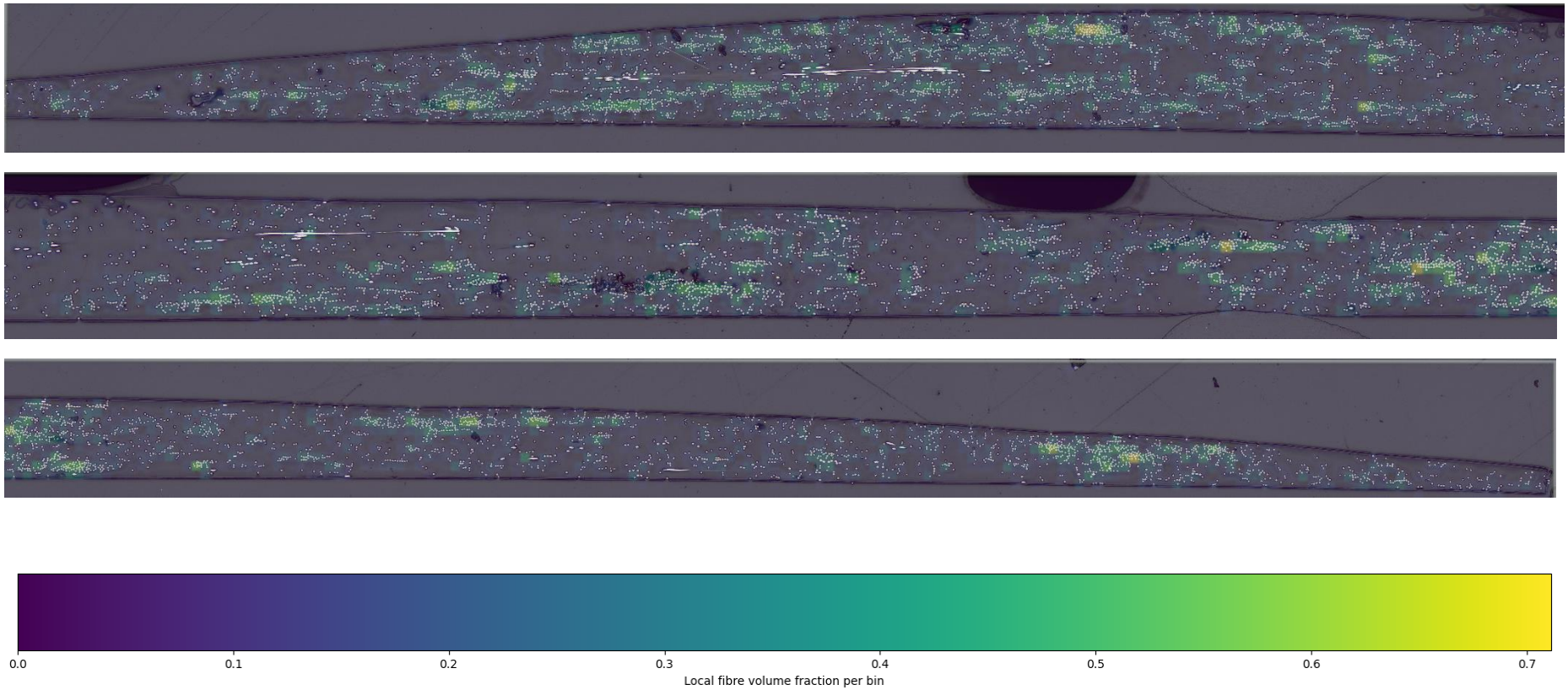

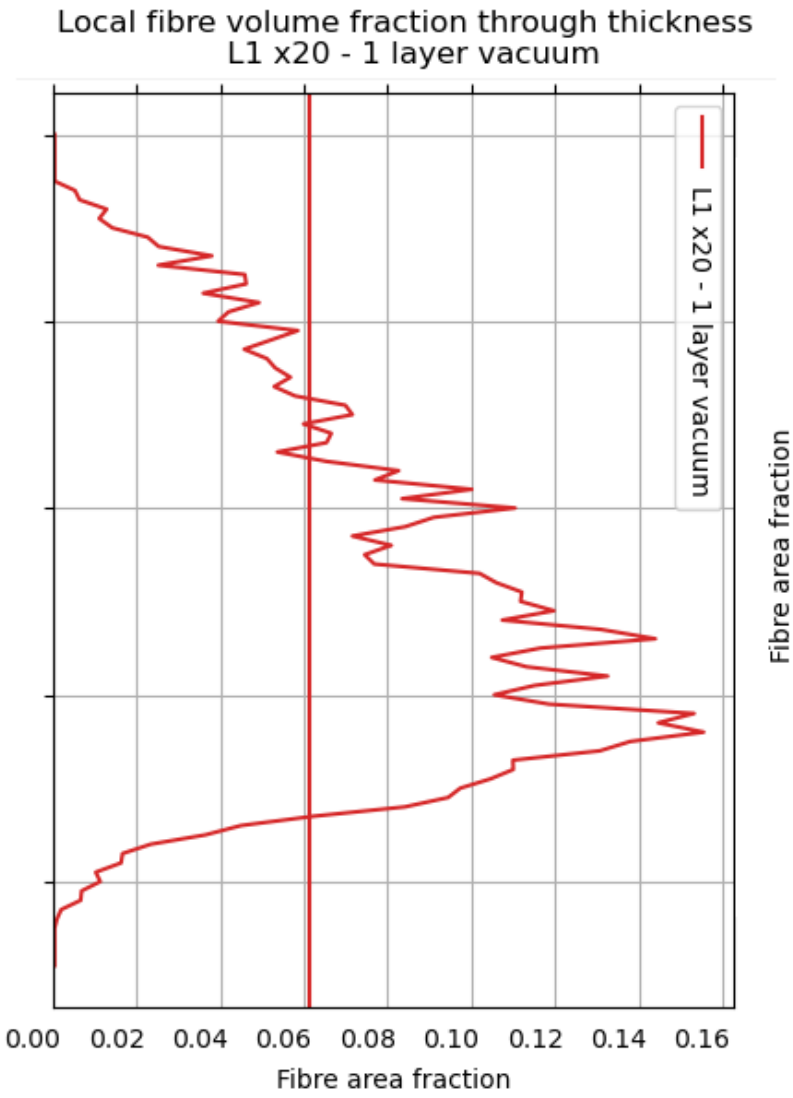
Local fibre volume fraction through thickness
L1 x20 - 1 layer vacuum
L1 x20 - 1 layer vacuum
0.00
0.02
0.04
0.06
0.08
0.10
0.12
0.14
0.16
Fibre area fraction

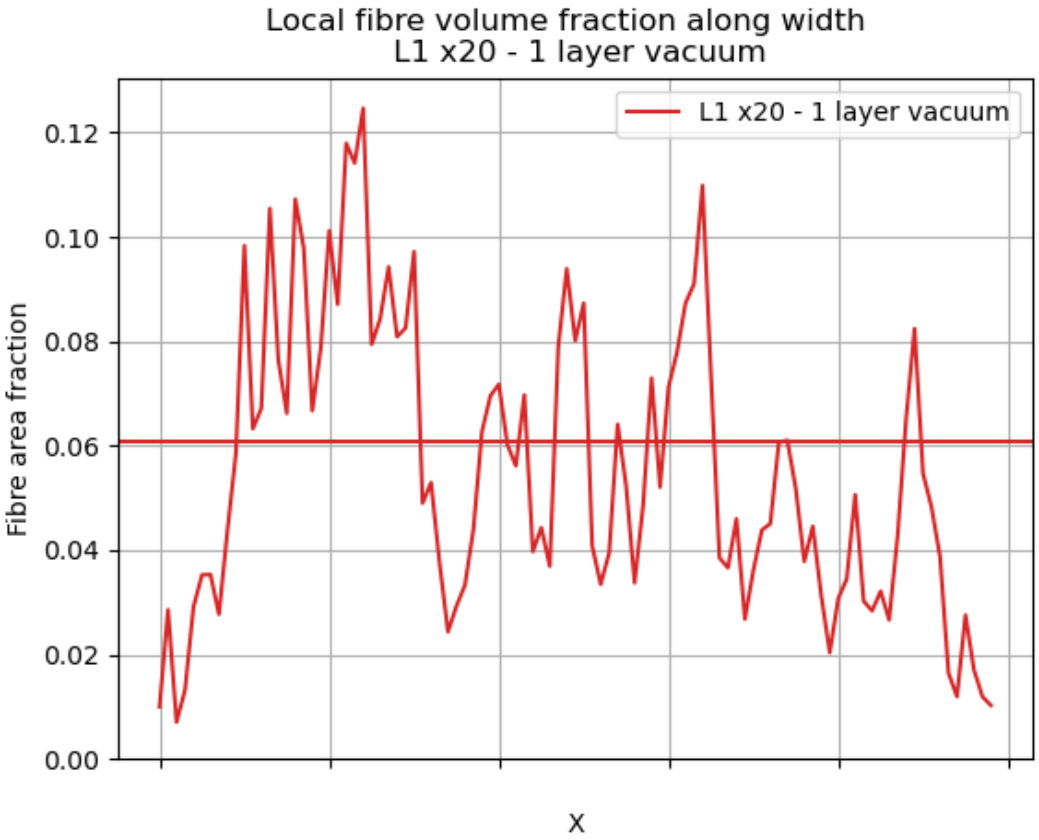
Local fibre volume fraction along width
L1 x20 - 1 layer vacuum
L1 x20 - 1 layer vacuum
0.12
0.10
0.08
0.06
0.04
0.02
0.00
Fibre area fraction
X

## L5 x20

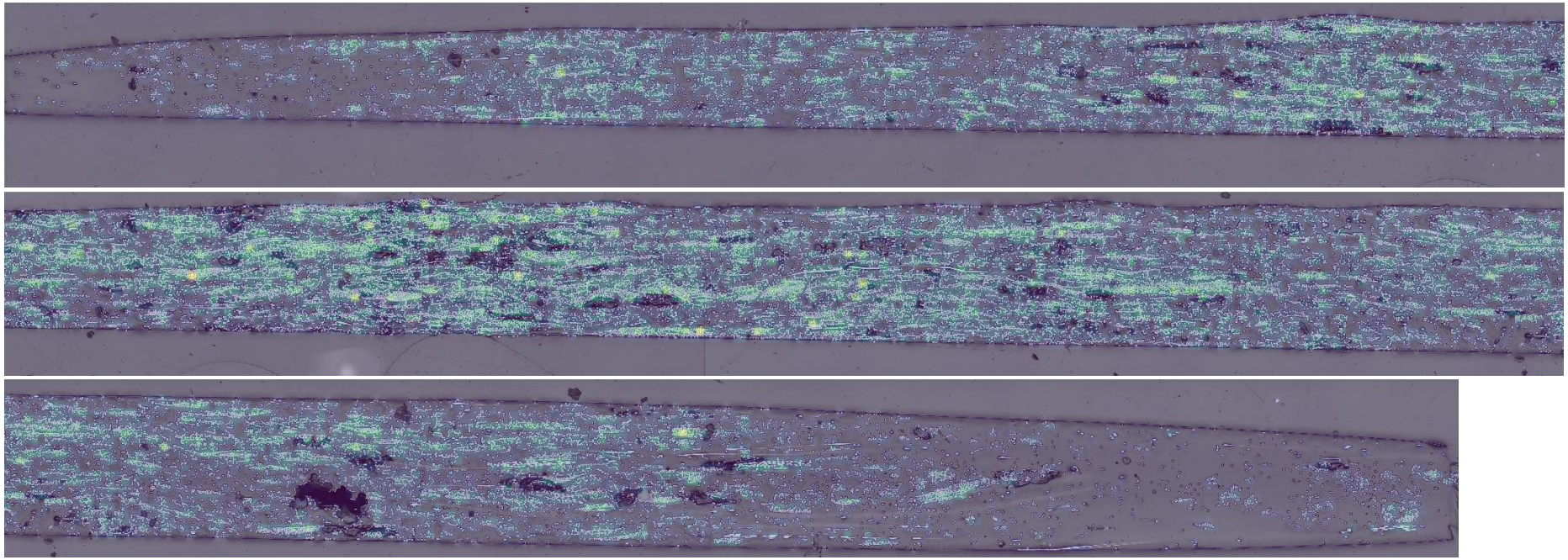

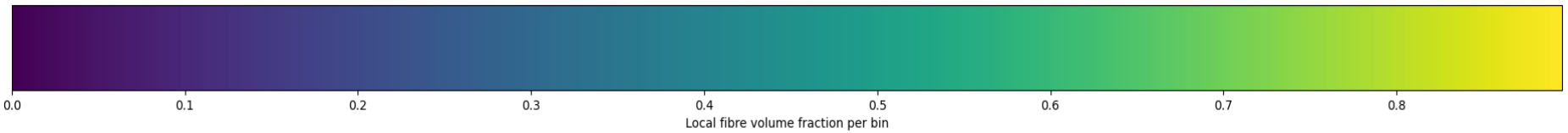

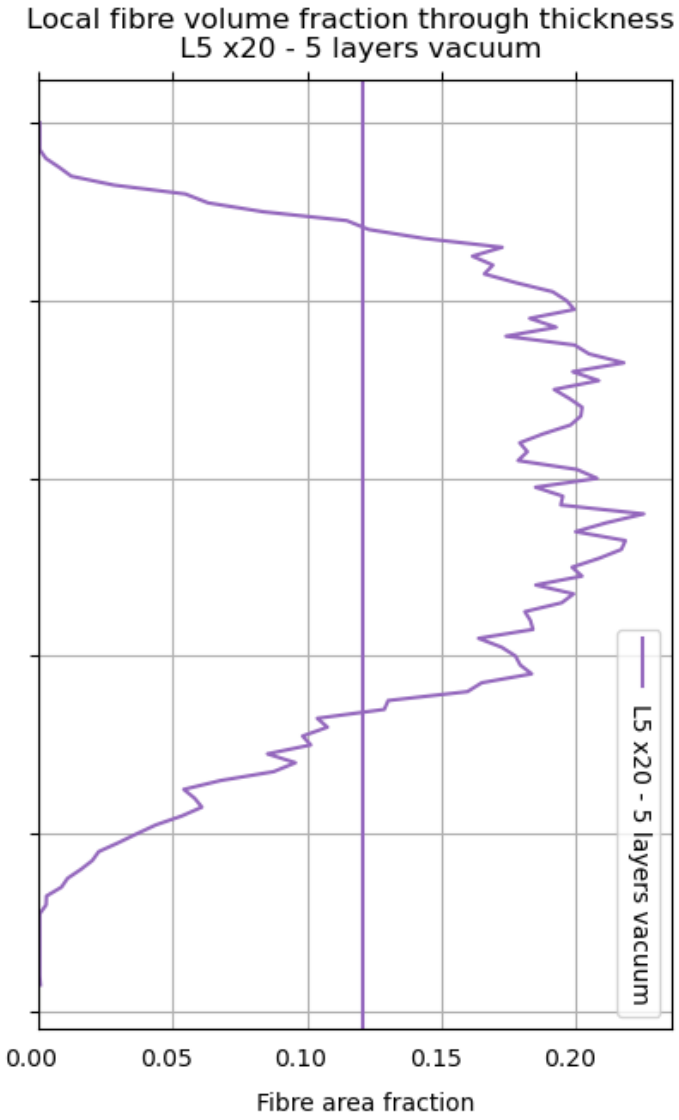
Local fibre volume fraction through thickness
L5 x20 - 5 layers vacuum
L5 x20 - 5 layers vacuum
0.00
0.05
0.10
0.15
0.20
Fibre area fraction

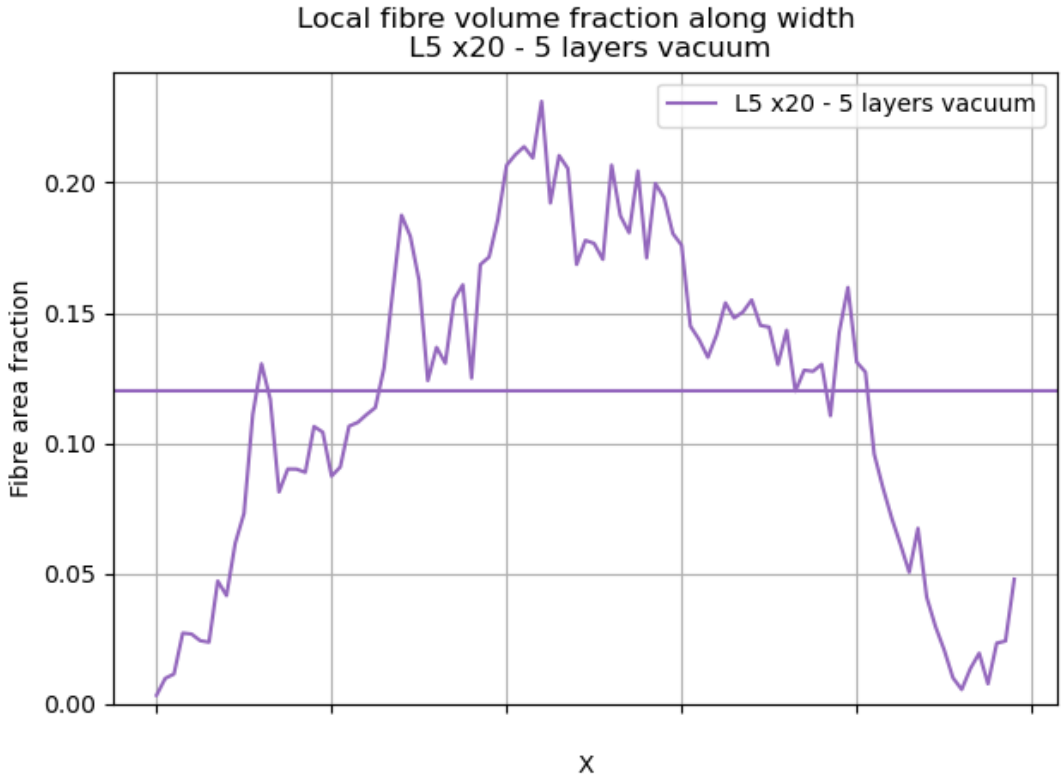
Local fibre volume fraction along width
L5 x20 - 5 layers vacuum
L5 x20 - 5 layers vacuum
0.00
0.05
0.10
0.15
0.20
Fibre area fraction
X

## S2 x50

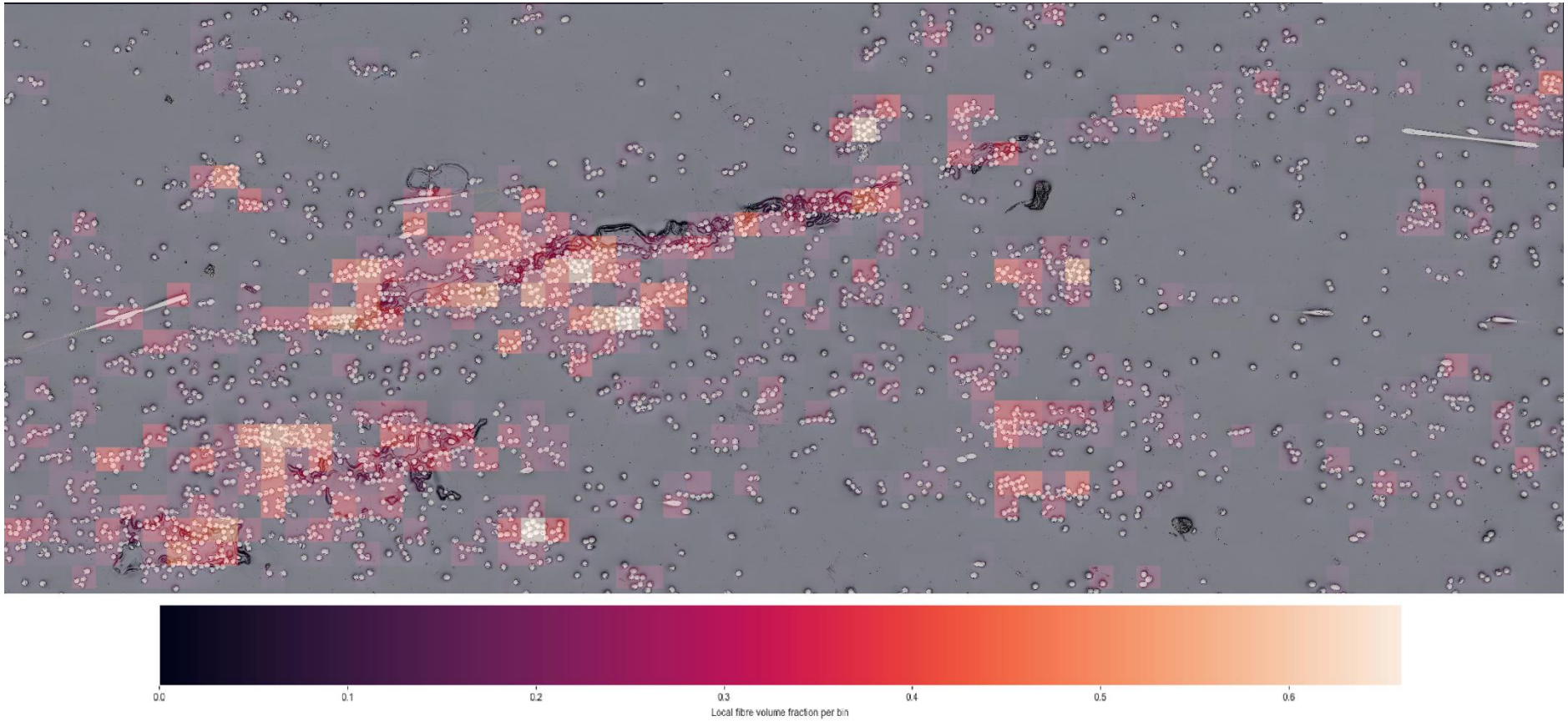

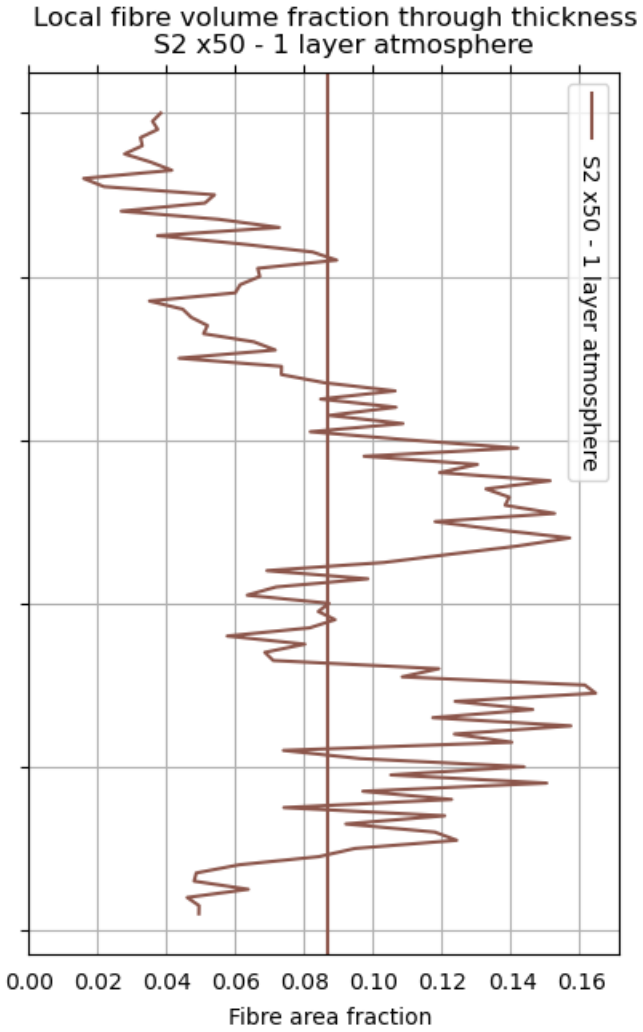
Local fibre volume fraction through thickness
S2 x50 - 1 layer atmosphere
S2 x50 - 1 layer atmosphere
0.00 0.02 0.04 0.06 0.08 0.10 0.12 0.14 0.16
Fibre area fraction

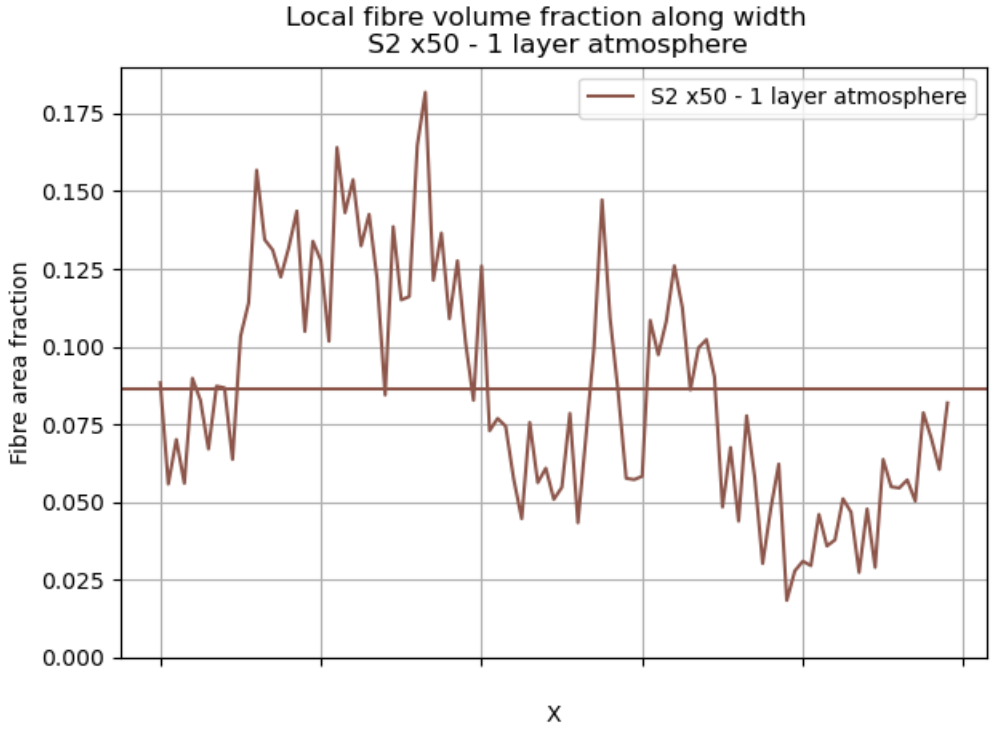
Local fibre volume fraction along width
S2 x50 - 1 layer atmosphere
S2 x50 - 1 layer atmosphere
0.175
0.150
0.125
0.100
0.075
0.050
0.025
0.000
Fibre area fraction
X

## Aerospace reference

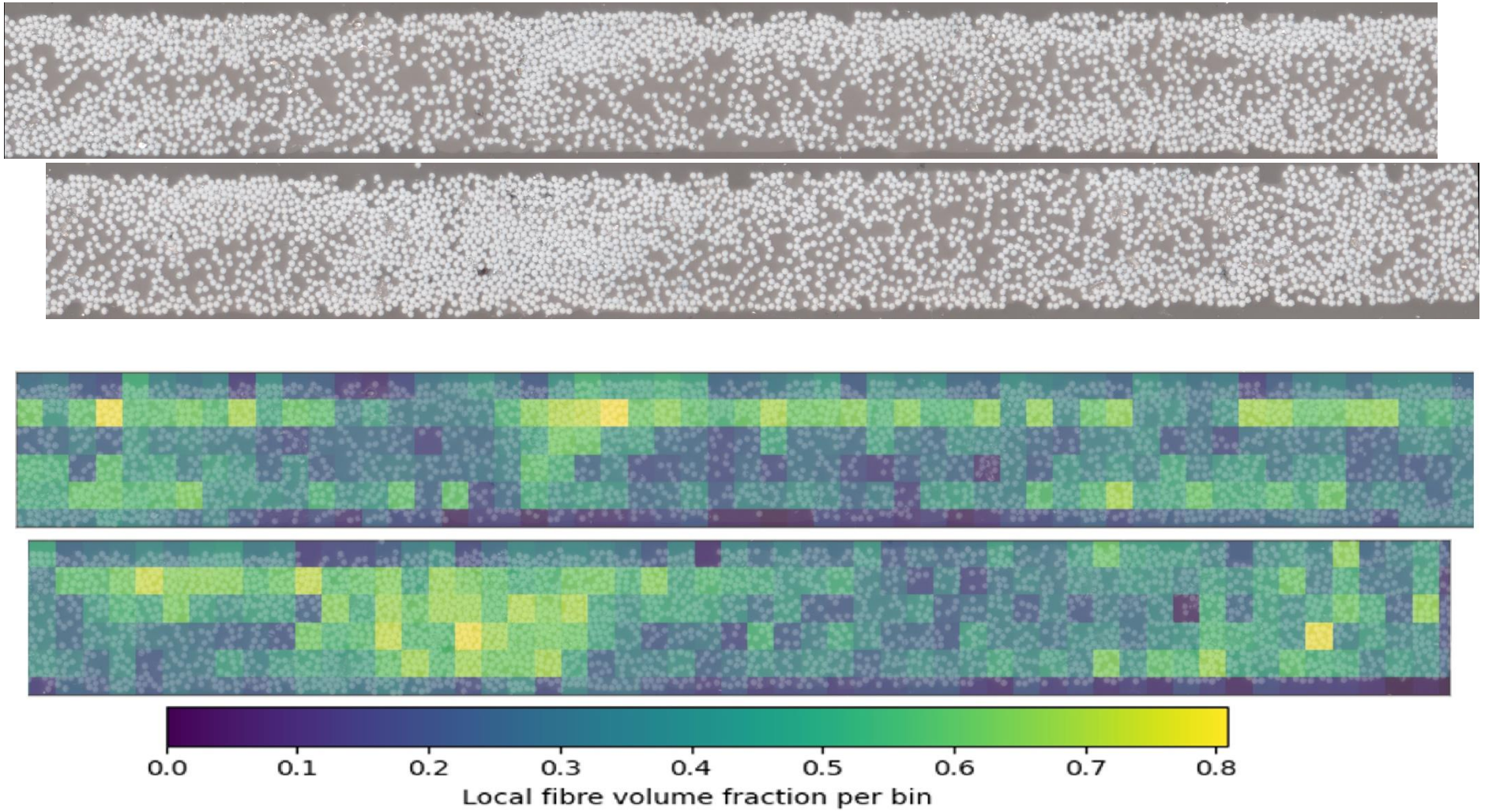

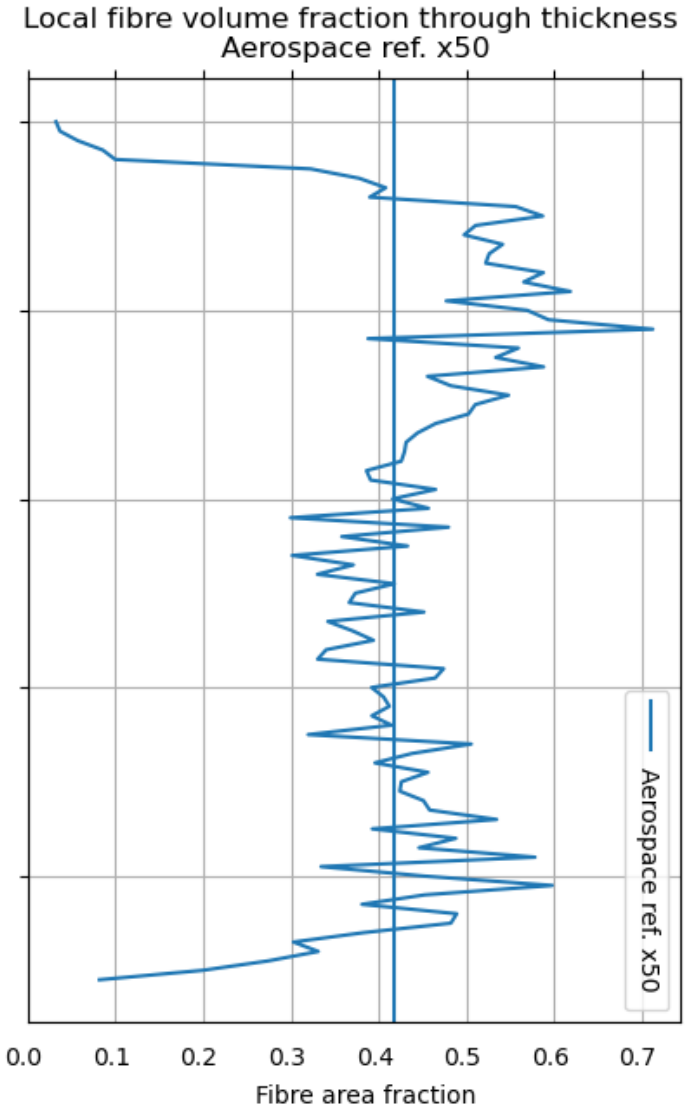
Local fibre volume fraction through thickness
Aerospace ref. x50
Aerospace ref. x50
0.0
0.1
0.2
0.3
0.4
0.5
0.6
0.7
Fibre area fraction

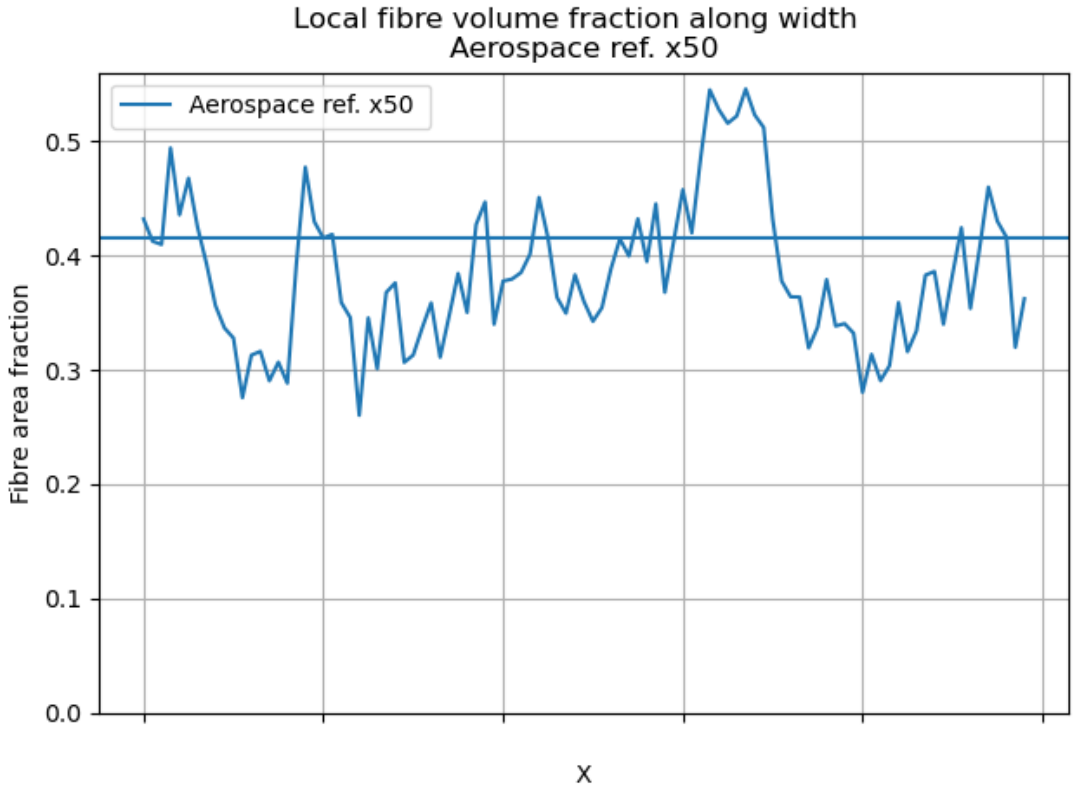
Local fibre volume fraction along width
Aerospace ref. x50
Aerospace ref. x50
0.0
0.1
0.2
0.3
0.4
0.5
Fibre area fraction
X